

Long-Term Stability Analysis of APM Conceptual Repository Design in Sedimentary and Crystalline Rock Settings

NWMO-TR-2015-27

December 2015

Zorica Radakovic-Guzina, Azadeh Riahi and Branko Damjanac

Itasca Consultant Group, Inc.

nwmo

NUCLEAR WASTE
MANAGEMENT
ORGANIZATION

SOCIÉTÉ DE GESTION
DES DÉCHETS
NUCLÉAIRES



Nuclear Waste Management Organization
22 St. Clair Avenue East, 6th Floor
Toronto, Ontario
M4T 2S3
Canada

Tel: 416-934-9814
Web: www.nwmo.ca

Long-Term Stability Analysis of APM Conceptual Repository Design in Sedimentary and Crystalline Rock Settings

NWMO-TR-2015-27

December 2015

Zorica Radakovic-Guzina, Azadeh Riahi and Branko Damjanac
Itasca Consultant Group, Inc.

This report has been prepared under contract to NWMO. The report has been reviewed by NWMO, but the views and conclusions are those of the authors and do not necessarily represent those of the NWMO.

All copyright and intellectual property rights belong to NWMO.

Document History

Title:	Long-Term Stability Analysis of APM Conceptual Repository Design in Sedimentary and Crystalline Rock Settings		
Report Number:	NWMO-TR-2015-27		
Revision:	R000	Date:	December 2015
Itasca Consulting Group, Inc.			
Authored by:	Zorica Radakovic-Guzina, Azadeh Riahi and Branko Damjanac		
Verified by:	Loren Lorig		
Approved by:	Branko Damjanac		
University of Alberta			
Reviewed by:	Derek Martin		
Nuclear Waste Management Organization			
Reviewed by:	Tom Lam		
Accepted by:	Mark Jensen		

ABSTRACT

Title: Long-Term Stability Analysis of APM Conceptual Repository Design in Sedimentary and Crystalline Rock Settings
Report No.: NWMO-TR-2015-27
Author(s): Zorica Radakovic-Guzina, Azadeh Riahi and Branko Damjanac
Company: Itasca Consultant Group, Inc.
Date: December 2015

Abstract

The long-term safety and performance of a Deep Geological Repository for used nuclear fuel will rely, in part, on the integrity of the geosphere barrier enclosing the repository. The purpose of this report is to present an illustrative case study intent on providing a bounding thermal-mechanical-hydraulic estimate of repository and geosphere response and evolution during excavation, operations and post-closure phases. The analyses consider the Mark II (48 bundle) canister design and repository configuration in crystalline and sedimentary rock settings at a nominal depth of 500 m below ground surface. On a timeframe of 1 million years (1Ma), a period relevant to the demonstration of repository safety, the influence of time dependent material properties and varied repository loading conditions are simulated. These include long-term rock mass strength degradation, thermal loading generated by canister heat flux, glacial ice-sheet advance and retreat, rare and extremely strong earthquake ground motions, internal repository gas pressure generated by canister corrosion, and transient hydraulic formation pressures. The analysis conducted is focused at the scale of the canister placement rooms and repository panels. Results provide time series estimates of overall repository stability during 1Ma that, among other factors, provide quantitative estimates of rock mass deformation and damage, evolution of the Excavation Damage Zone (EDZ), and the hydraulic and mechanical loading of a used fuel canister.

In order to conduct the analyses a number of assumptions were applied to explore and test notions of geosphere and repository stability and resilience to future loading. These included:

- 1) Hydraulic Formation Pressures: A hydrostatic formation porewater pressure of 5 MPa was assumed for the repository at 500 m depth;
- 2) Long-term Rock Mass Strength: Time dependent rock mass strength degradation was simulated with the long-term rock mass strength set to 40% of Unconfined Compressive Strength (UCS). This long-term rock mass strength is equivalent to the crack initiation stress;
- 3) Temperature Evolution: The emplacement room geometry and layout is designed to ensure the maximum used fuel canister surface temperature remains less than 100°C;
- 4) Glaciation: Transient glacial ice-sheet history and loading were explicitly considered with maximum ice-sheet thicknesses approaching 3 km;

- 5) Earthquakes: Rare and strong ground motions (i.e., 0.5g) associated with long return period (1Ma) earthquakes were simulated;
- 6) Repository Gas Pressures: Gas generation within the repository as a result of corrosion yields a maximum pressure of 8.3 MPa;
- 7) Effective Stress Formulation: Effective stress calculations were estimated without considering pore pressure relief in the low porosity rocks;
- 8) Joint Strength: Pre-existing joints within a crystalline rock mass were assumed to be cohesionless with a relatively low friction angle of 30°; and
- 9) Thermal Expansivity: Relatively high coefficients of thermal expansion were applied to yield bounding estimates of rock mass damage.

For both sedimentary and crystalline settings rock mass damage will occur as a result of: i) transient changes in in-situ stress magnitude and orientation; ii) thermally-induced stress changes; and iii) time-dependent rock mass strength degradation. It is evident from the analyses that damage is primarily driven by thermally-induced stress changes occurring within approximately 1,000 years of repository closure. Glacial ice-sheet loading and strong earthquake ground motion do not materially influence rock damage. The bounding long-term rock mass strength of 40% UCS does not yield significant damage and, in this case, it is evident that the engineered backfill provides confinement that mitigates spalling, fracture dilation, and likely contributes to slowing the rate of time-dependent strength degradation. Displacements are uniform and relatively small not exceeding 40 mm. During glaciation maximum displacements are estimated not to exceed 12 mm. The EDZ is predicted to extend not more than 1 to 3 meters into the enclosing host rock formation from excavated surfaces. For this illustrative case study, the maximum loading of used fuel canisters for the sedimentary and crystalline scenarios is predicted to be 22.7 and 29.8 MPa, respectively. A detailed explanation of the above findings and unique aspects related to sedimentary and crystalline environs is provided herein.

TABLE OF CONTENTS

	<u>Page</u>
ABSTRACT	iii
1. INTRODUCTION	1
1.1 BACKGROUND	1
1.2 OVERVIEW OF MARK II UFC DESIGNS	2
1.2.1 Repository Layout	2
1.2.2 Placement Room Backfilling	7
1.3 MODELLING APPROACH OVERVIEW	8
1.4 REPORT OUTLINE	9
2. NUMERICAL MODELLING ASSUMPTIONS AND LIMITATIONS	10
3. LONG-TERM STABILITY ANALYSIS OF A MARK II REPOSITORY IN SEDIMENTARY ROCK	11
3.1 THERMAL AND MECHANICAL MATERIAL PARAMETERS	11
3.1.1 Geological Profile	11
3.1.2 Material Models and Parameters	11
3.1.3 Voronoi Block Approximation of Mechanical Behaviour of Cobourg Limestone ..	14
3.1.4 Voronoi Model Calibration	16
3.1.5 Long-Term Strength	20
3.1.6 Backfill Materials	21
3.2 GEOLOGICAL AND REPOSITORY INDUCED PERTURBATIONS	23
3.2.1 In Situ Stresses	23
3.2.2 Thermal Loading	24
3.2.3 Long-Term Strength Degradation	25
3.2.3.1 Static-Fatigue Curves and Evolution of Damage Due to Strength Degradation ..	25
3.2.3.2 Time-dependent Strength Degradation in UDEC	28
3.2.4 Glacial Loading	30
3.2.5 Gas and Pore Pressures	32
3.2.5.1 Pore Pressures	33
3.2.5.2 Gas Pressures	33
3.2.6 Seismic Loading	35
3.2.6.1 Ground Motions	35
3.2.6.2 Material Damping	38
3.3 DESCRIPTION OF THE MODELS	39
3.3.1 Modelling and Coupling Approach	39
3.4 MODELLING MARK II DESIGN IN SEDIMENTARY ROCK	40
3.4.1 Thermal Model	40
3.4.2 Mechanical Model	42
3.4.2.1 Static Model	44
3.4.2.2 Dynamic Model	44
3.5 MODELLING RESULTS	45
3.5.1 Temperature Evolution	45
3.5.2 Time-Dependent Strength Degradation and Thermo-Mechanical Loading	49
3.5.3 Glacial Loading	51
3.5.4 Gas Pressure	51
3.5.5 Seismic Loading	52

3.5.6	Loading on the UFC	54
3.6	SUMMARY AND DISCUSSION	56
4.	LONG-TERM STABILITY ANALYSIS OF A MARK II REPOSITORY IN CRYSTALLINE ROCK	58
4.1	THERMAL AND MECHANICAL MATERIAL PARAMETERS	58
4.1.1	Geological Profile	58
4.1.2	Material Models and Parameters.....	58
4.1.3	Voronoi Block Approximation	60
4.1.4	Voronoi Model Calibration	60
4.1.5	Long-Term Strength	64
4.1.6	Discrete Fracture Network (DFN).....	64
4.1.6.1	DFN Geometrical Parameters	65
4.1.6.2	DFN Generation	66
4.1.6.3	DFN Simplification	67
4.1.6.4	DFN Mechanical Parameters	68
4.1.7	Backfill Materials	69
4.2	GEOLOGICAL AND REPOSITORY INDUCED PERTURBATIONS	69
4.2.1	In-Situ Stresses	69
4.2.2	Thermal Loading	70
4.2.3	Long-Term Strength Degradation.....	70
4.2.3.1	Static-Fatigue Curves and Evolution of Damage Due to Strength Degradation..	71
4.2.3.2	Time-dependent Strength Degradation in UDEC	71
4.2.4	Glacial Loading.....	71
4.2.5	Seismic Loading	73
4.2.5.1	Ground Motions and Damping	73
4.3	DESCRIPTION OF THE MODELS	74
4.3.1	Modelling and Coupling Approach	74
4.4	MODELLING MARK II DESIGN IN CRYSTALLINE ROCK	75
4.4.1	Thermal Model	75
4.4.2	Mechanical Model	77
4.4.3	Static Model.....	79
4.4.4	Dynamic Model.....	79
4.4.4.1	3D Model with Explicit Representation of DFN.....	79
4.5	MODELLING RESULTS	81
4.5.1	Evolution of Temperatures	81
4.5.2	Thermo-Mechanical Loading and Time-Dependent Strength Degradation	85
4.5.3	Glacial Loading.....	87
4.5.4	Seismic Loading	88
4.5.5	Loading on the UFC	90
4.5.6	Effect of DFN	92
4.6	SUMMARY AND DISCUSSION	94
5.	CONCLUSIONS	96
	REFERENCES	99
	APPENDIX A: ABBREVIATIONS, ACRONYMS AND UNITS	102

LIST OF TABLES

	<u>Page</u>
Table 1:	Geological Profile Close to Repository Horizon With Formation Thicknesses.....11
Table 2:	Intact Rock and Rock Mass Mechanical Properties13
Table 3:	Bedding Plane Strength Data of Cobourg Limestone13
Table 4:	Thermal Properties for the Units in the Sedimentary Setting.....14
Table 5:	Summary of Voronoi Stiffness and Strength Parameters from Unconfined Tests18
Table 6:	Calibrated Micro-mechanical Properties for the Voronoi Blocks and Contacts...20
Table 7:	Mechanical Properties for the Engineered Barrier Materials22
Table 8:	Thermal Properties for the Engineered Barrier Materials22
Table 9:	Waste Package Characteristics for Mark II Design24
Table 10:	Heat Release Rate at Time of Placement (post-reactor discharge time of 30 years).....25
Table 11:	Analyzed Seismic Scenarios with Corresponding PGVs and PGAs at the Repository Level (AMEC Geomatrix 2011).....36
Table 12:	Simulation Times for Ground Motions at the Repository Level.....38
Table 13:	Intact Rock and Hoek-Brown Rock Mass Properties58
Table 14:	Mechanical Model Parameters of Granite Rock Mass.....59
Table 15:	Thermal Properties of Granite Rock Mass.....60
Table 16:	Summary of Voronoi Stiffness and Strength Parameters from Unconfined Tests62
Table 17:	Calibrated Micro-mechanical Properties for the Voronoi Blocks and Contacts...64
Table 18:	Fracture Orientation Model65
Table 19:	Fracture Sizes Model at Forsmark.....66
Table 20:	In-situ Stress State (NWMO 2014)70

LIST OF FIGURES

	<u>Page</u>
Figure 1:	Conceptual Mark II layout out for 4.6 Million Bundles in Sedimentary Rock (SNC-Lavalin 2014)3
Figure 2:	Conceptual Mark II layout out for 4.6 Million Bundles in Crystalline Rock (SNC- Lavalin 2014)4
Figure 3:	Conceptual Mark II Repository (NWMO 2015)5
Figure 4:	Mark II In-room Placement (SNC-Lavalin 2014).....6
Figure 5:	Mark II Placement Room Layout Plan and Longitudinal Sections in Sedimentary and Crystalline Rocks (SNC-Lavalin 2014)7
Figure 6:	Bentonite Blocks and Bricks Room Seal Arrangement in Mark II Design.....8
Figure 7:	<i>UDEC</i> Voronoi Model and Its Micro-properties.....15
Figure 8:	Axial Response Obtained from the Numerical Tests on Calibrated Voronoi Block Model of Cobourg Limestone (Compression Positive).....17
Figure 9:	Confined Response (for 15 MPa and 30 MPa Confinement) Obtained from the Numerical Tests on Calibrated Voronoi Block Model of Cobourg Limestone (Compression Positive).....19
Figure 10:	Unconfined Strength of the Cobourg Limestone After 100 Days.....21
Figure 11:	Power Decay as a Function of Time.....25
Figure 12:	Bases and Approximation of Rock Mass Static-fatigue Curves Used in Long-term Room Stability Analyses.....27

Figure 13:	Damage Curves Used as Input to the UDEC LdB Analyses ($P_c = 0$).....	28
Figure 14:	Calculated Glacially-induced Rebound Stress (BP = before present); s11, s22, and s33 are the Normal Stress Components, s12, s13, and s23 are the Shear Stress Components	31
Figure 15:	Approximation of Glacially-induced Rebound Stress Histories Used in Repository Stability Analysis.....	32
Figure 16:	Repository Gas Pressure Profile Used in Geomechanical Stability Analyses for Mark II Repository Design	35
Figure 17:	Time History of Horizontal Velocity Component (H1) at the Repository Level for M7.4 at 200 km	36
Figure 18:	Time History of Horizontal Velocity Component (H2) at the Repository Level for M7.4 at 200 km	37
Figure 19:	Time History of Vertical Velocity Component (V) at the Repository Level for M7.4 at 200 km	37
Figure 20:	Numerical Model Simulation Chart	39
Figure 21:	Detail of Geometry of the Near-Field Thermal Model in Sedimentary Rock	41
Figure 22:	Geometry of the Far-Field Thermal Model in Sedimentary Rock.....	42
Figure 23:	Geometry of the Mechanical Model in Sedimentary Rock.....	43
Figure 24:	Details of Geometry of the Mechanical Model in Sedimentary Rock.....	43
Figure 25:	Locations of the Temperature History Points in the Near-field Thermal Model in Sedimentary Rock.....	46
Figure 26:	Temperature Histories at Characteristic Points (indicated in Figure 25) as Calculated From the Near- and Far-field Models in Sedimentary Rock.....	46
Figure 27:	A Comparison Between Modified and Unmodified Combined Temperature Histories at Characteristic Point 1 in Sedimentary Rock.....	47
Figure 28:	Evolution of Temperature Fields in the Near-field Model in Sedimentary Rock..	48
Figure 29:	Evolution of Temperature Fields in the Far-field Model in Sedimentary Rock....	49
Figure 30:	Repository Damage Evolution to 50 ka in Sedimentary Rock	50
Figure 31:	Microcracks in the Rock During Glaciation Period and Beyond, to 1Ma in Sedimentary Rock	51
Figure 32:	Effect of Gas loading on Damage in Sedimentary Rock.....	52
Figure 33:	Microcracks in the Rock at Peak Temperature Subjected to Three Different Earthquakes at 10^{-6} Probability Level in Sedimentary Rock	53
Figure 34:	Microcracks in the Rock at Peak Glacial Load Subjected to Three Different Earthquakes at 10^{-6} Probability Level in Sedimentary Rock	54
Figure 35:	Evolution of Pressure on the UFC in Sedimentary Rock	55
Figure 36:	Crystalline Rock Failure Criteria: Non-linear Hoek-Brown and Fitted Mohr- Coulomb	59
Figure 37:	Axial Response Obtained from the Numerical Tests on Calibrated Voronoi Block Model of Granite (Compression Positive)	61
Figure 38:	Confined Response (for 15 MPa and 30 MPa Confinement) Obtained from the Numerical Tests on Calibrated Voronoi Block Model of Granite (Compression Positive)	63
Figure 39:	DFN Fractures, Colored by Area (top) and Stereonet of Orientation (bottom)	67
Figure 40:	Three Different Realizations Used in 3DEC Analyses: DFNs are Simplified with a Minimum Fracture Radius of 1m.	68
Figure 41:	Calculated Glacially-induced Rebound Stress Histories (BP = before present); s11, s22, and s33 are the Normal Stress Components, s12, s13, and s23 are the Shear Stress Components.....	72

Figure 42:	Approximation of Glacially-induced Rebound Stress Histories Used in Repository Stability Analysis.....	73
Figure 43:	Simulation Chart	74
Figure 44:	Detail of Geometry of the Near-Field Thermal Model in Crystalline Rock	76
Figure 45:	Geometry of the Far-Field Thermal Model in Crystalline Rock.....	77
Figure 46:	Geometry of the Near-Field Mechanical Model in Crystalline Rock	78
Figure 47:	Detail of Geometry of the Near-Field Mechanical Model in Crystalline Rock	78
Figure 48:	DFN Region in the 3DEC Model.....	80
Figure 49:	Locations of the Temperature History Points in the Near-Field Thermal Model in Crystalline Rock	82
Figure 50:	Temperature Histories at Characteristic Points (indicated in Figure 49) as Calculated from the Near- and Far-Field Models in Crystalline Rock	82
Figure 51:	A Comparison Between Modified and Unmodified Combined Temperature Histories at Characteristic Point 1 in Crystalline Rock.....	83
Figure 52:	Evolution of Temperature Fields in the Near-field Model in Crystalline Rock.....	84
Figure 53:	Evolution of Temperature Fields in the Far-field Model in Crystalline Rock	85
Figure 54:	Evolution of Damage in Crystalline Rock.....	87
Figure 55:	Evolution of Damage during Glaciation Period and Beyond, to 1Ma in Crystalline Rock.....	88
Figure 56:	Microcracks in the Rock at Peak Temperature Subjected to Three Different Earthquakes at 10^{-6} Probability Level in Crystalline Rock	89
Figure 57:	Microcracks in the Rock at Peak Glacial Load Subjected to Three Different Earthquakes at 10^{-6} Probability Level in Crystalline Rock	90
Figure 58:	Evolution of Pressure on the UFC in Crystalline Rock	92
Figure 59:	DFN realization II: Contours of Shear Displacements (m) on Joints at Peak Rock Temperature	93
Figure 60:	DFN Realization II: Contours of Shear Displacements (m) on Joints at Peak Glacial Load.....	93

1. INTRODUCTION

1.1 BACKGROUND

The Nuclear Waste Management Organization (NWMO) is responsible for the implementation of Adaptive Phased Management (APM), the federally-approved plan for safe long-term management of Canada's used nuclear fuel. Under the APM approach, used nuclear fuel will ultimately be placed within a Deep Geological Repository (DGR) in a suitable rock formation within an informed and willing host community.

Safety is a priority for the implementation of the APM program. To support the focus on safety, a generic geomechanical stability analysis study of the repository has been carried out as part of a wide range of complementary activities to assess the performance of the multi-barrier repository concept at timeframes relevant to illustrating long-term DGR safety.

The long-term safety and performance of a used fuel repository will rely in part on the surrounding geosphere and the perturbations imposed on it. The purpose of the present illustrative study is to gain insight on the geomechanical stability of the Mark II DGR concept focusing primarily on the placement panels, which represent the most extensive development in the repository. The perturbation effects of different loading conditions, including used fuel canister thermal history, glaciation, low probability strong ground motion earthquakes and internally generated repository gas pressures from used fuel canister corrosion were analyzed. The analysis also includes the overall stability of the placement rooms, damage and deformation of the surrounding rock mass and evolution of the excavation damaged zone (EDZ). It also provides performance measures examined to assess effects on the long-term integrity of the natural geologic barriers.

The report is intended to serve as a more quantitative basis to evaluate the long-term integrity of natural barriers and far-field impacts that could influence repository engineered design consistent with the development of a strong safety case.

1.2 OVERVIEW OF MARK II UFC DESIGNS

1.2.1 Repository Layout

In Canada, the concept of deep geological repository (DGR) for the long-term management of Canada's used nuclear fuel has been studied for many years. The primary target is to locate a DGR in a low permeability crystalline or sedimentary rock setting. A recent repository design proposed by NWMO was the Mark II concept, with capacity to accommodate 4.6 million CANDU used nuclear fuel bundles. The basic concept and elements common to all DGR layouts proposed by the NWMO include:

1. Shaft only access;
2. Incorporation of an underground demonstration facility;
3. Central access tunnels connecting main and ventilation shaft stations; ; and
4. Panels comprised of UFC placement rooms at selected spacing intervals,

The conceptual Mark II repository occupies a footprint of about 1.9 km by 2.0 km in a sedimentary rock setting (Figure 1) and 1.7 km by 1.4 km in crystalline one (Figure 2). Figure 3 shows conceptual layouts of the repository facilities. Details of the Mark II concept design are described in NWMO (2015). The Mark II UFC is a mid-sized capacity copper/steel composite vessel containing 48 CANDU used fuel bundles. Prior to emplacement, each UFC is encapsulated in a rectangular buffer box consisting of an outer shell comprised of highly compacted bentonite (HBC). The dimensions of the buffer box are approximately 1.0 m x 1.0 m x 2.8 m (Figure 4). The placement rooms have cross-sectional dimensions of 2.2 m (high) and 3.2 m (wide), and a nominal length of 300m.

In this study, it was assumed that excavation of the placement rooms will be carried out with extreme care to minimize damage in the room walls. Based on the condition of the host rock and room layout, rock ground support is not anticipated. Within the placement rooms, the buffer boxes would be stacked in 2 levels separated by dense backfill blocks as shown in Figure 4. A total of 341 buffer boxes can be placed in each placement room. Upon completion of buffer box placement, a seal comprised of highly compacted bentonite (HCB) behind a concrete bulkhead will be constructed at the entrance of each placement room (Figure 5). In sedimentary rock, a 25 m room-to-room spacing has been adopted whereas, a 20 m room-to-room spacing is needed for crystalline rock. This spacing promotes heat dissipation and will ensure the maximum temperature of the UFC surface is less than 100°C. The panels are connected by panel access tunnels that are connected to two parallel central tunnels running from the main shaft complex to the ventilation shaft.

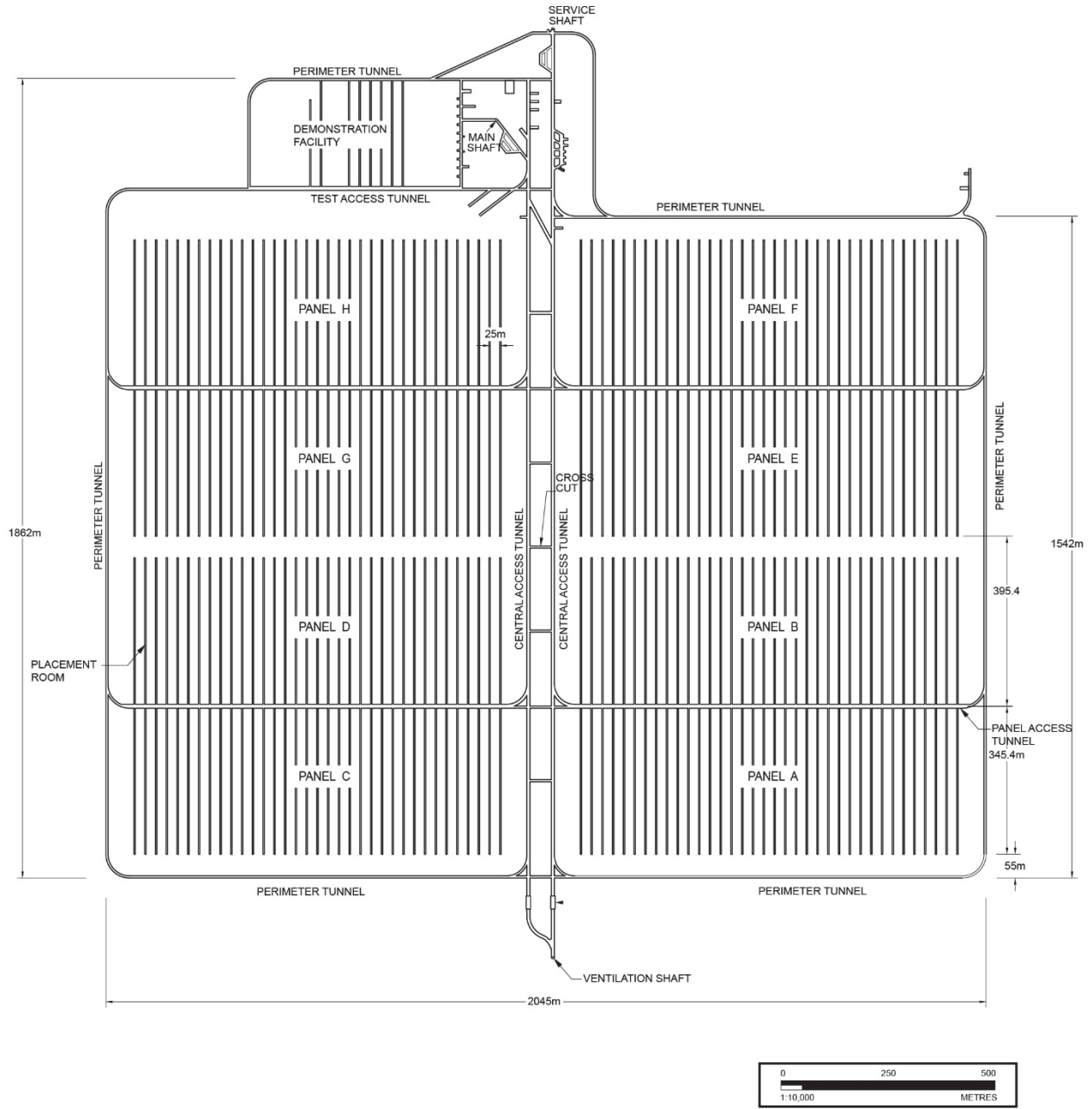


Figure 1: Conceptual Mark II layout out for 4.6 Million Bundles in Sedimentary Rock (SNC-Lavalin 2014)

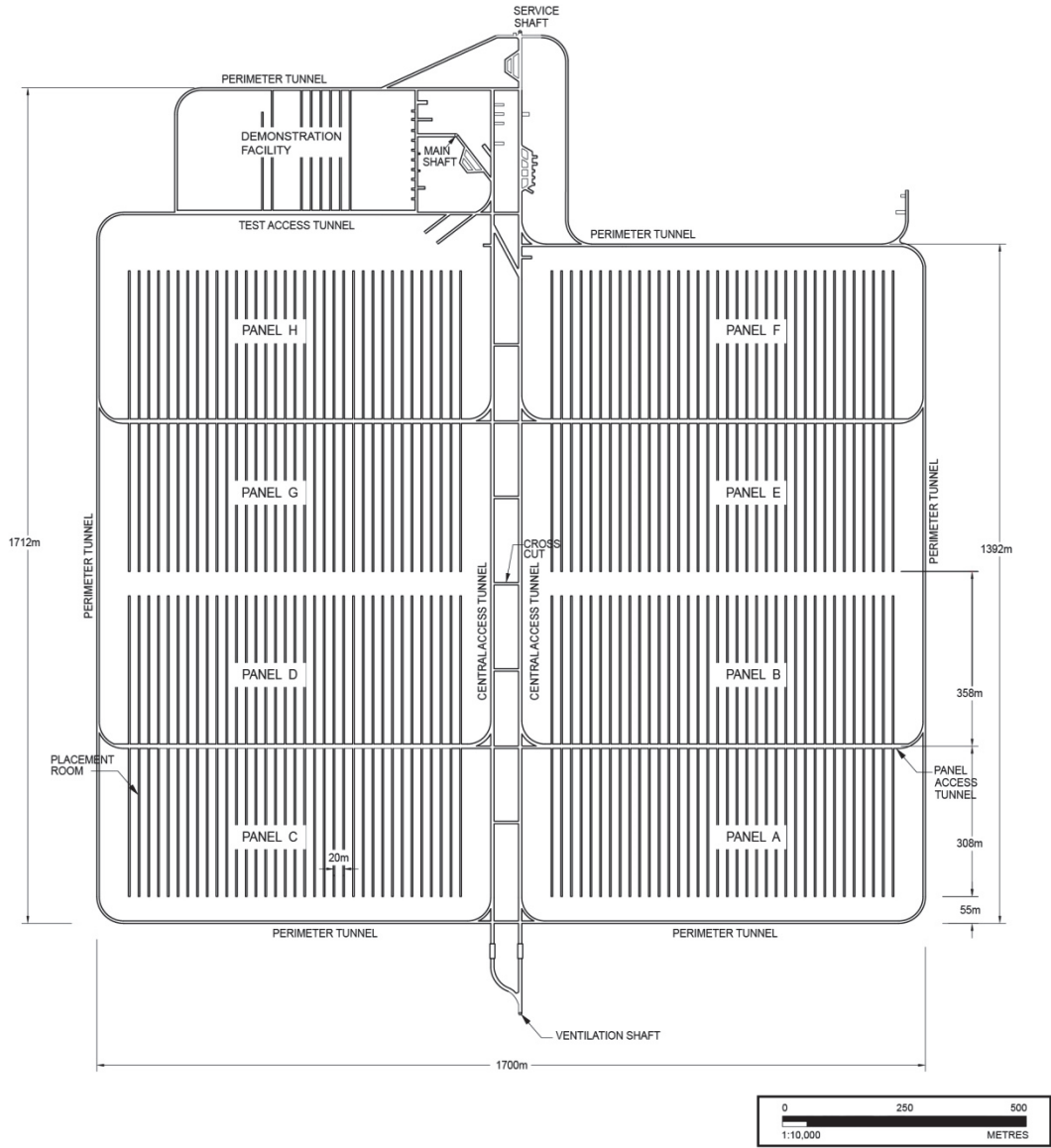


Figure 2: Conceptual Mark II layout out for 4.6 Million Bundles in Crystalline Rock (SNC-Lavalin 2014)

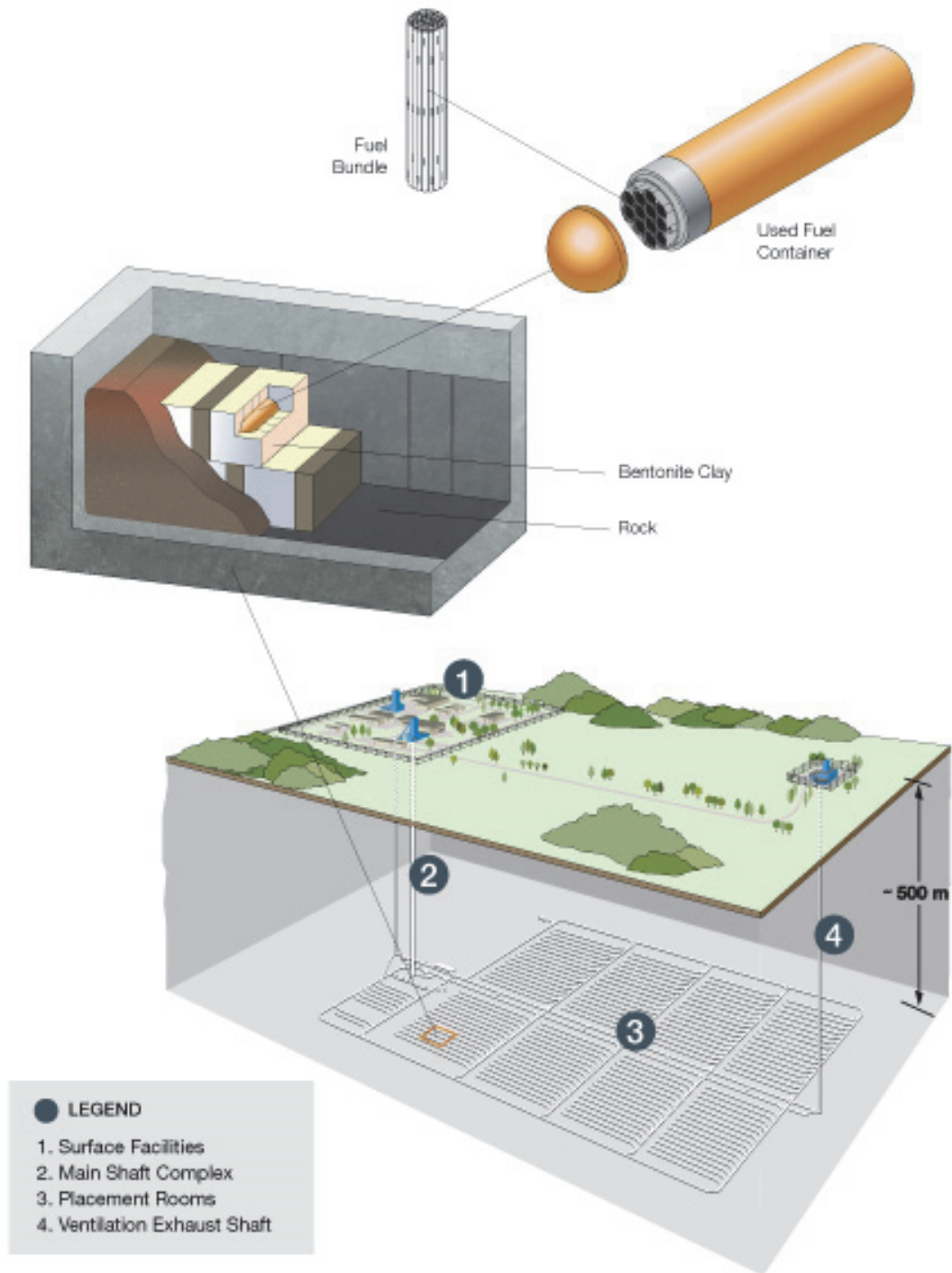


Figure 3: Conceptual Mark II Repository (NWMO 2015)

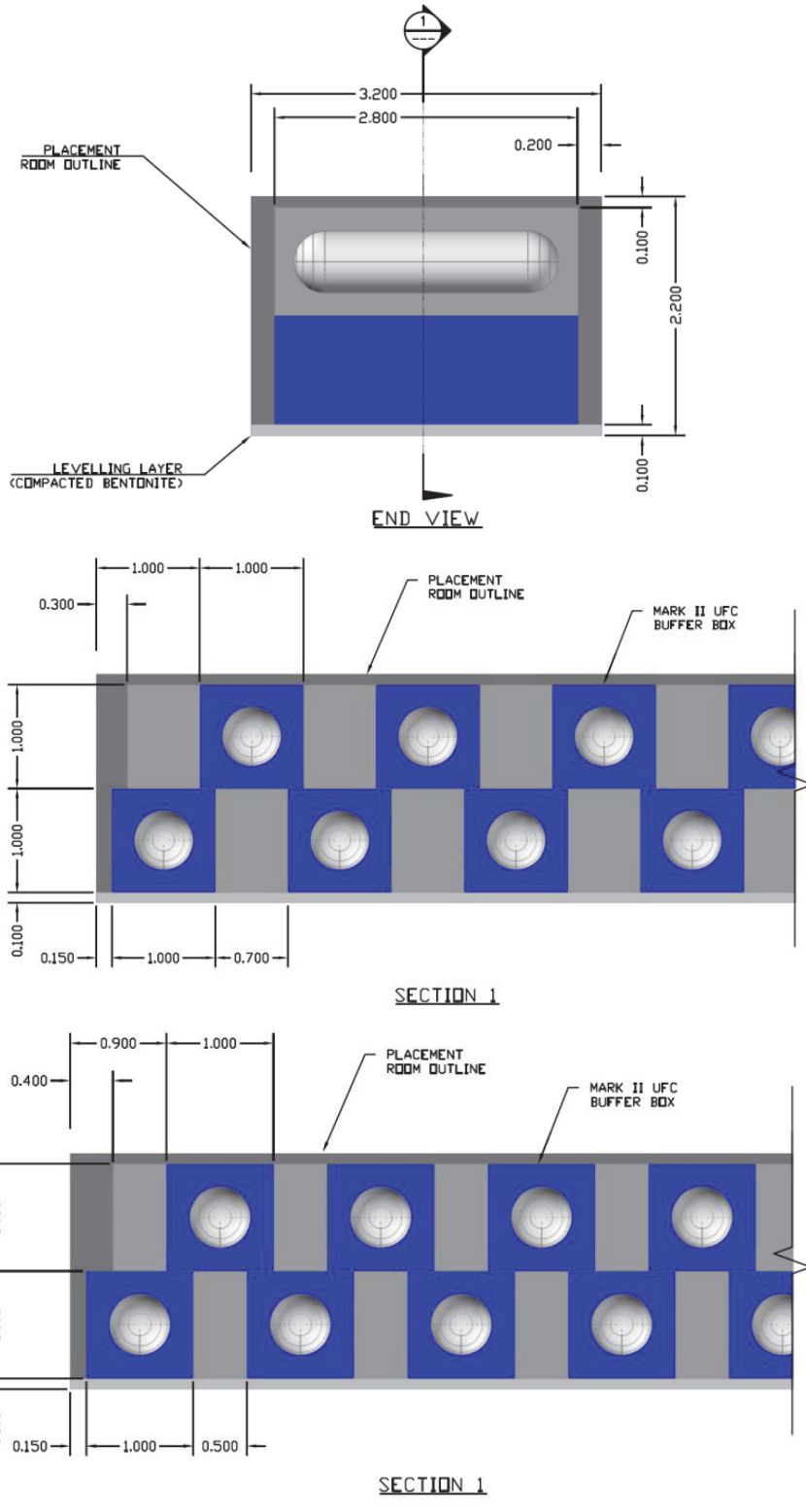
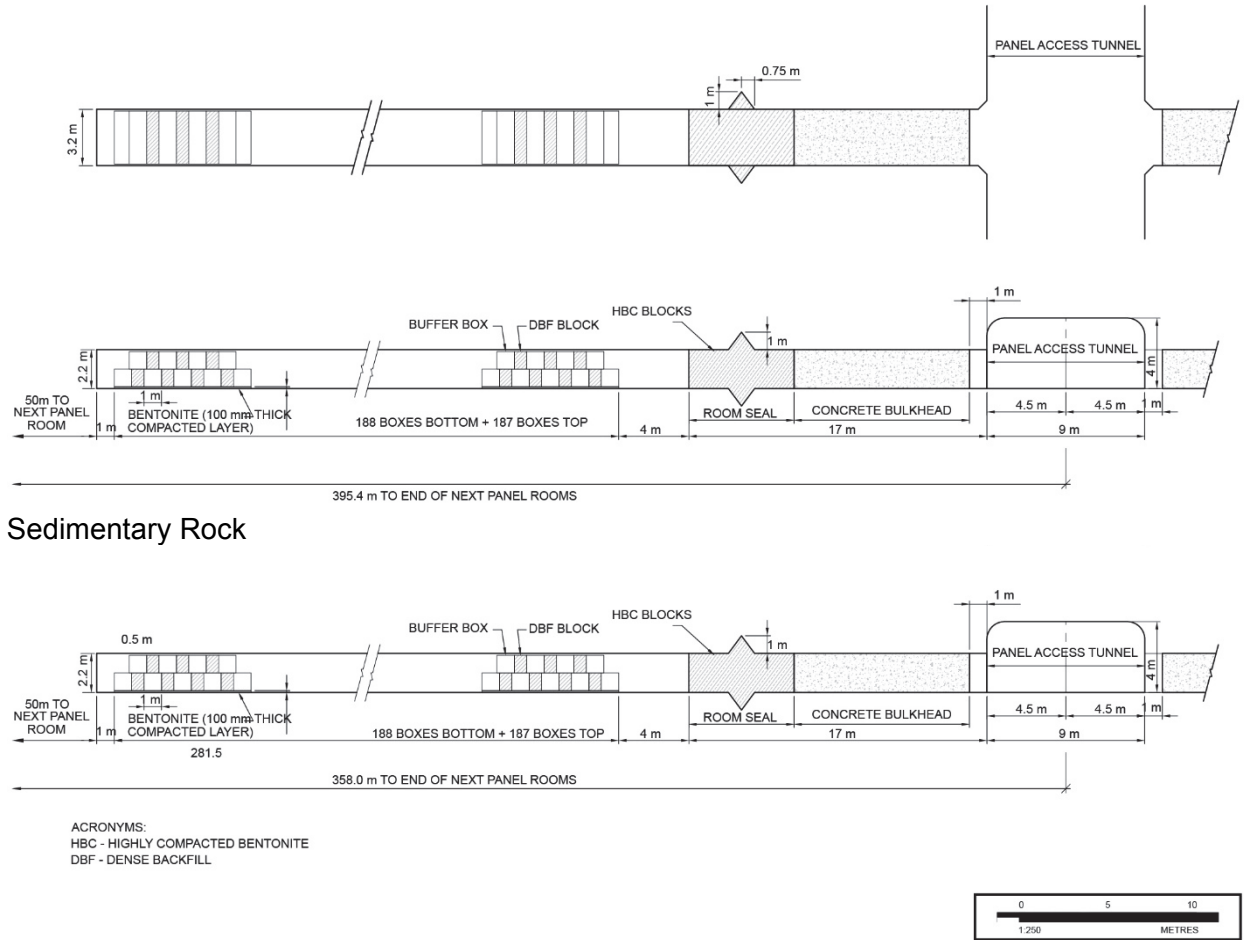


Figure 4: Mark II In-room Placement (SNC-Lavalin 2014)



Sedimentary Rock

Crystalline Rock

Figure 5: Mark II Placement Room Layout Plan and Longitudinal Sections in Sedimentary and Crystalline Rocks (SNC-Lavalin 2014)

1.2.2 Placement Room Backfilling

During the placement of the buffer and spacer boxes, backfilling of the space between the UFC packages and placement room walls using 100% bentonite pellets will be carried out as the placement operation proceeds toward the room entrance. Once the room has been filled with waste packages and bentonite backfill, dense backfill (DBF) blocks similar to spacer blocks will be positioned after the last buffer block for the next 4 m long section. Based on the conceptual design, an EDZ cut-off section will be constructed around the placement room intersecting the highly damage zone of the host rock. Once the excavation is complete, a room seal will be assembled using dense backfill (DBF) and bentonite bricks arranged as shown in the isometric view of the room seal arrangement (Figure 6). The sealing of the placement room will be complete after the space around the sealing bricks is filled with loosely placed bentonite pellets, in a similar process to that used during buffer box placement (SNC-Lavalin 2014).

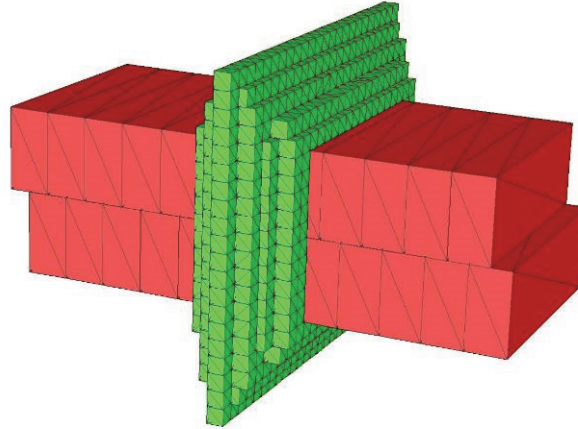


Figure 6: Bentonite Blocks and Bricks Room Seal Arrangement in Mark II Design

1.3 MODELLING APPROACH OVERVIEW

The long-term stability analyses documented herein were focused on the placement rooms. The effects of different loading conditions expected during a timeframe of 1 Ma on repository performance were analyzed, including the overall stability of the rooms, damage and deformation of the surrounding rock mass and evolution of EDZ. The following is the list of the loads and conditions relevant for stability and performance of the repository, which were considered as an individual event or in combination with other scenarios in the analysis.

- In situ stresses: The rock mass is in a relatively high in situ stress state with horizontal stresses exceeding vertical at the nominal 500 m depth. Excavation of the repository will cause perturbation of the in situ stress state and stress concentrations around the excavations will cause deformation and, potentially, damage and failure of the rock mass.
- Thermal loading: The used nuclear fuel is assumed to be placed in the DGR 30-years post-reactor age. As such, it will continue releasing heat that will increase temperatures within the near- and far field. Increase in the temperature of the enclosing rock mass could create thermally-induced stresses, deformation and potential damage of the rock mass.
- Time-dependent strength degradation of the stressed rock mass: There is evidence that the strength of the rocks subjected to certain stress levels and exposed to atmosphere gradually degrades with time. Time-dependent strength degradation of the rock mass can lead to damage and failure of the rock mass.
- Repository porewater and gas pressures: The rock mass at the DGR horizon is considered saturated with a hydraulic formation pressure equivalent to a fresh water head with a water table at ground surface. In low permeability sedimentary rock, gases generated inside the placement rooms as a result of waste degradation will impose a pressure on the excavated room walls, and if sufficiently large, may result in fracturing of the rock.

The impacts of potential gas generation is insignificant in the case of a repository in crystalline rock setting. Gas escape through the fractured host rock is sufficient to release pressure in the repository (NWMO 2012).

- Glacial ice sheet advance and retreat: It is expected that the repository will be subjected to multiple glacial events during 1 Ma. The ice sheet that can be up to 3 km thick will impose additional loading on the repository, and will cause additional deformation, damage and potential failure of repository pillars and/or excavated rooms.
- Seismic shaking. Over the period of 1 Ma the repository will be subject to multiple seismic events, some with a very small probability of recurrence and relatively strong intensity.

1.4 REPORT OUTLINE

The following is the outline of this report.

- Chapter 2 listed software used in the analyses and discusses assumptions and limitations of the numerical modelling.
- Chapter 3 describes the long-term stability analysis in a sedimentary rock setting with the following subsections:
 - A summary of the geomechanical characteristics and model parameters used in this study;
 - A discussion of different loading scenarios and conditions that can affect long-term performance of a repository and their representation in the analyses;
 - The thermal and mechanical models used for the long-term room stability analysis considering various loading scenarios and sequences;
 - The results of the long-term room stability analysis considering different loading scenarios and evolution of the EDZ surrounding a placement room; and
 - A discussion of the stability analysis results and overall conclusions of the long-term stability analyses.
- Chapter 4 describes the long-term stability analysis in a crystalline rock setting with similar subsections as in Chapter 3.
- Chapter 5 provides a summary of the long-term stability for both the sedimentary and crystalline settings.

2. NUMERICAL MODELLING ASSUMPTIONS AND LIMITATIONS

There were three numerical modelling codes used for the analyses and simulations documented in this report:

1. *UDEC* Version 6.00.297 (Itasca 2014);
2. *FLAC3D* Version 5.01.100 (Itasca 2012); and
3. *3DEC* Version 5.20.181 (Itasca 2013).

Although these modelling techniques are well established in engineering research and practice and capable of providing valuable insight into geomechanics problems, it is acknowledged that they entail a number of simplifying assumptions with the prime objective of capturing the dominant mode of behaviour, with respect to the long-term development of a zone of damage/yielding around the placement rooms. The critical assumptions with respect to the models are described where appropriate throughout this report.

Simulation of the long-term stability of the placement rooms under the in situ conditions can be carried out only in an approximate manner. However, because the models reflect the mechanical responses (based on established mathematical and physical theories) for reasonable input parameters, they can be used in the process of performance assessment in a general sense (i.e., suggesting the extent of damaged zone around the rooms). It is in this context that the current model analyses were conducted and should be evaluated. Considering that the objective of the analyses is to predict the repository performance for 1 Ma, which includes considerable uncertainty, the input parameters were selected in order to provide conservative bounds to expected responses. Whenever possible, the model outputs are judged by comparison with observations and experience regarding behaviour of similar excavations in comparable conditions. Although sensitivity studies provide perspective and can be a useful tool in modelling geotechnical conditions, the need for such perspective must be balanced with the modelling objective, site-condition uncertainty and the amount of conservatism included in the model in general. For this study, conservative assumptions regarding geotechnical conditions were made, and sensitivity studies focused on the long-term loading conditions (e.g., seismic loading, pore pressure).

3. LONG-TERM STABILITY ANALYSIS OF A MARK II REPOSITORY IN SEDIMENTARY ROCK

3.1 THERMAL AND MECHANICAL MATERIAL PARAMETERS

3.1.1 Geological Profile

The geology of the hypothetical repository site in the sedimentary setting, with stratigraphy at the repository depth listed in Table 1, consists predominantly of a near horizontally layered sequence of dolostone, shale and limestone. Table 1 includes units from Upper and Middle Ordovician. The repository is proposed to be located at a nominal depth of 500 mBGS, in the competent, low porosity limestone of the Cobourg Formation. The stratigraphy of the hypothetical site was created based on DGR site characterization boreholes (DGR-1 to DGR-8) (Intera 2011) conducted at Bruce nuclear site. The mechanical properties used for long-term stability analyses were also based mainly on laboratory testing of rock samples taken from the investigation boreholes (Gorski et al. 2009a, 2009b, 2010a, 2010b and Golder 2013).

The laboratory testing has been carried out on a number of samples from the representative bedrock formations. However, the largest number of tests were carried out on the samples from the Cobourg Formation, in which the hypothetical repository is situated. The tests include: 1) P- and S-wave velocity measurements, 2) unconfined compressive strength (UCS) and triaxial compressive strength testing, 3) acoustic emission monitoring during the UCS test, which was used to determine crack initiation, CI, and crack damage, CD, thresholds, 4) Brazilian tensile strength test, 5) bedding plane direct shear strength tests, and 6) long-term strength degradation testing.

Table 1: Geological Profile Close to Repository Horizon With Formation Thicknesses

Geological Unit	Top of Rock Unit (mBGS)	Thickness (m)
Georgian Bay ¹	325.3	96.2
Blue Mountain ¹	421.5	49.5
Collingwood ¹	471	8.6
Cobourg ²	479.6	38.4
Cobourg – Lower ²	518	8
Sherman Fall	526	47.3

Note: 1 - a part of Georgian Bay and Blue Mountain Formation (Table 4)

2 – a part of Cobourg Formation (Table 4)

3.1.2 Material Models and Parameters

Six different geological units listed in the sequence from the bottom to the top, are included in the numerical model of the pillar-scale room stability model, including: 1) Sherman Fall limestone, 2) lower Cobourg limestone, 3) Cobourg limestone, 4) Collingwood shale; 5) Blue Mountain shale and 6) Georgian Bay shale. The mechanical properties of these rock units are

listed in Table 2. The table includes mechanical properties of the intact rock (unconfined compressive strength, UCS, and Young's modulus, E_i), geological strength index, GSI, parameters of the Hoek-Brown failure envelope (m_i , m_b , s , and a), confining stress used for estimation of Mohr-Coulomb failure parameters fitted to the Hoek-Brown failure curve, σ_3 , calculated rock mass mechanical properties (Young's modulus, E_{rm} , and strength, σ_{rm}), fitted Mohr-Coulomb strength parameters (cohesion, cc , and friction angle, ϕ), and in the units where explicitly represented, the bedding plane stiffness. The bedding plane stiffness, k_n , is calculated to be consistent with bedding plane spacing, d , and stiffnesses of the intact rock and rock mass, using the following relation:

$$\frac{1}{E_{rm}} = \frac{1}{E} + \frac{1}{k_n d} \quad (1)$$

Barton (2007, Section 16.4 therein) states that the ratio of static joint normal-to-shear stiffness for most of the tested cases is in the range between 11 and 15. For the room stability analysis, the joint shear stiffness, k_s , is assumed to be 1/15 of the joint normal stiffness. The bedding planes strength parameters used in the analysis are listed in Table 3 (Itasca 2011). The bedding planes are assumed to be non-dilatant, which is conservative because it results in underestimation of the bedding plane shear strength. The strength parameters were determined based on laboratory testing on the cores from the exploratory boreholes (DGR-1 through DGR- 8) drilled during the site characterization investigation at Bruce nuclear site.

The mechanical behaviour of the geological units away from the placement rooms is approximated in the numerical models as continuum Mohr-Coulomb materials with equivalent intact or rock-mass material properties (depending on explicit representation of the bedding planes). Continuum approximation for these units away from the rooms is certainly considered adequate, because they are relatively far from the placement rooms and are expected to behave elastically over 1 Ma.

For the Cobourg limestone around the placement rooms, the Voronoi block approach (Section 3.1.3 and Damjanac et al. 2007) was used. Despite the lack of bedding partings observed on cores retrieved from the Cobourg limestone during OPG low- and intermediate-level waster (L&ILW) DGR site characterization (Intera 2011), bedding planes were conservatively assumed in the Cobourg limestone. These bedding planes are represented explicitly at 0.75 m spacing with the Voronoi block assembly represents the intact rock between them. It is reasonable to assume that these bedding planes are not continuous and there are 50% of the rock bridges within the bedding planes with the strength equal to that of the intact rock.

Table 2: Intact Rock and Rock Mass Mechanical Properties

Unit	Intact Lab		Hoek Brown parameters					Rock mass			Mohr Coulomb		Bedding kn GPa/m
	UCS MPa	Ei GPa	GSI	mi	mb	S	a	Erm GPa	σ_{cm} MPa	σ_3^3 MPa	C MPa	ϕ deg	
Georgian Bay ¹	34	9.04	76	10.1	4.3	0.069	0.501	7.51	11.4	10.1	3.04	37	
Blue Mountain ¹	34	9.64	77	6.0	2.6	0.078	0.501	8.14	10.1	12.1	3.16	31	
Collingwood ¹	117	36.9	76	10.0	4.2	0.070	0.501	30.7	39.2	12.8	6.66	44	1157
Cobourg ²	121	43.5	89	11.4	7.7	0.295	0.5	41.4	67.3	9.4	11.1	49	1157
Cobourg – Lower ²	101	39.1	89	7.2	4.8	0.295	0.5	37.2	52.4	14.1	11.4	42	1157
Sherman Fall	76	38.8	87	11.0	6.9	0.236	0.5	36.5	38.7	14.8	7.76	44	

Note: 1 – a part of Georgian Bay and Blue Mountain formations (Table 4)

2 – a part of Cobourg Formation (Table 4)

3 – overburden weight

Table 3: Bedding Plane Strength Data of Cobourg Limestone

Peak Cohesion MPa	Peak Friction Angle Deg.	Residual Cohesion MPa	Residual Friction Angle Deg.	Tensile Strength MPa
3.31	38.3	0	38.3	0.66

The thermal properties for the geological units in the sedimentary setting are listed in Table 4 (Golder 2013). The average values in the table are calculated based on the available testing results. In the thermal models, some of the units with relatively small thickness or unavailable thermal properties were lumped together. Also, the units of same rock types (e.g., carbonates, sandstone or shales) were lumped together where possible. The linear coefficients of thermal expansion of $2.0 \times 10^{-6} \text{ } 1/^{\circ}\text{C}$ and $6.7 \times 10^{-6} \text{ } 1/^{\circ}\text{C}$ were used in the analysis for shales and carbonates, respectively (Baumgartner 2005). The data on carbonate is consistent with the testing results on Cobourg Limestone at Darlington, Ontario, reported by Lo and Wai (1982).

Table 4: Thermal Properties for the Units in the Sedimentary Setting

Geological unit	Unit Top Depth m	Thickness m	Thermal Conductivity W/m°C		Specific Heat MJ/m ³ °C	
			Averages	Model Values	Averages	Model Values
Drift	0	29.4				
Hamilton Group						
Dundee						
Detroit River Group						
Bois Blac			3.31	4.47	2.82	3.36
Bass Island			4.56		2.97	
Unit G						
Unit F			5.55		4.28	
Unit F Salt						
Unit E						
Unit D						
Unit B and C	29.4	52.3	2.22	2.42	2.50	2.50
Unit B Anhydrate						
Unit A-2 Carbonate	81.7	27.0	2.58		2.36	
Unit A-1 Upper Carbonate	108.7	3.0				
Unit A-1 Carbonate	111.7	22.1				
Unit A-1 Evaporate	133.8	2.0	5.31		4.11	
Unit A0	135.8	2.3				
Guelph	138.1	71.4		2.55		1.83
Goat Island			2.55		1.83	
Gasport						
Lions Head						
Reynales/Fossil Hill	209.5	6.8				
Cabot Head	216.3	15.8		1.89		1.79
Manitoulin	232.1	15.6		1.89		1.79
Queenstone	247.7	77.6	1.89	1.89	1.79	1.79
Georgian Bay/Blue Mountain*	325.3	154.3	1.89	1.89	1.27	1.27
Cobourg*	479.6	46.4	2.27	2.27	1.63	1.69
Sherman Fall	526	47.3	1.90	1.90	1.61	1.61
Kirkfield	573.3	39.5	2.28	2.28	2.07	2.07
Coboconk	612.8	8.0	3.11	2.78	1.99	1.99
Gull River	620.8	53.4	2.73		2.17	
Shadow Lake	674.2	7.6		3.00		2.28
Cambriam						
Upper Precambrian	681.8	20.0		3.00		2.28
Precambrian	701.8					

Notes: see Tables 1 and 2 for subdivision of Cobourg Formation

3.1.3 Voronoi Block Approximation of Mechanical Behaviour of Cobourg Limestone

All rocks have a microstructure. The Voronoi tessellation scheme (example shown in Figure 7) is a numerical methodology used to represent microstructure and consists of an assembly of

small polygonal blocks. The blocks can be rigid or deformable, and, if deformable, either elastic or elastic-plastic. The blocks interact with each other through their contacts, which initially are elastic when the stresses are relatively small. As the load in the contacts increases, they can fail, either in tension or shear. Contact failure in tension is controlled by the contact tensile strength. The Coulomb slip criterion governs the onset of inelastic shear deformation, or slip of the block contact. Contacts between Voronoi blocks do not represent the actual internal structure of rocks. Instead, they are oriented randomly at relatively short spacing, acting as possible locations and orientations of discrete flaws within the rock. Failure of a contact in shear or tension represents fracturing of the rock mass. Fracturing initiates and evolves as a function of rock mass strength, and as dictated by stresses and forces in the rock mass. An example of the use of the Voronoi block approach for stability analysis of underground excavations at the Yucca Mountain Project, the U.S. program for high-level nuclear waste disposal, is described by Damjanac et al. (2007). The advantage of the Voronoi block approach is that it can simulate fracturing of a brittle rock mass, the formation of loose and unstable ground, and its rockfall. Continuum-based numerical models can be used to predict the redistribution of stresses, displacements and regions of inelastic deformation and damage, but they cannot predict rockfall. One disadvantage of the Voronoi block approach is that micro mechanical properties (of contacts and blocks) are not measured directly in laboratories. Instead, they have to be determined indirectly through the calibration process, in which micro mechanical properties are adjusted until the macro-mechanical behaviour measured in laboratories is matched by the response of the Voronoi block model in the numerical simulation of that laboratory experiment.

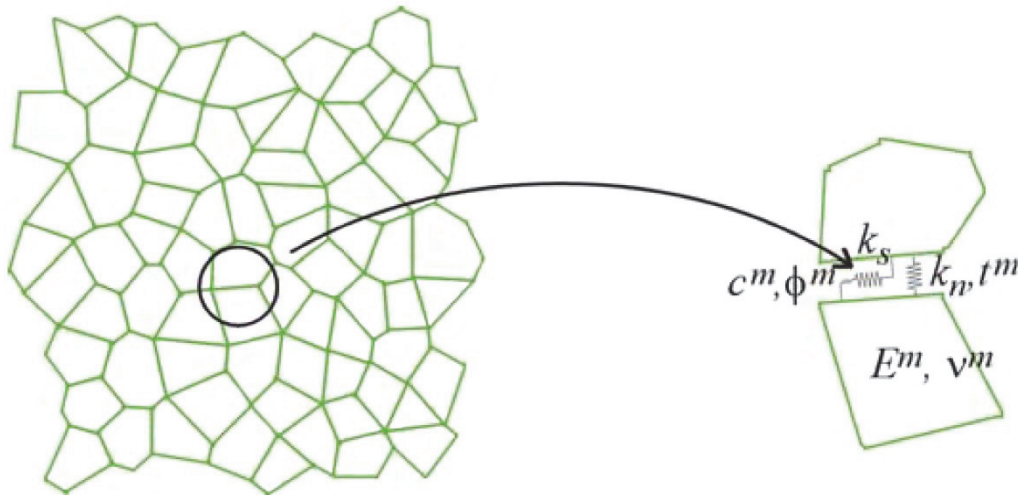


Figure 7: UDEC Voronoi Model and Its Micro-properties

The Voronoi block approach was selected for the analysis. The model is discretized into Voronoi blocks in the region around the room where stress concentrations from the in situ stresses and external loading occur. The average Voronoi block size (width) is selected to be 0.1 m. The ratio of the block size to the minimum room dimension (height), which is $0.1/2.2 = 0.045 \ll 1$, is sufficiently small so that the block size does not affect the model results.

3.1.4 Voronoi Model Calibration

The Voronoi block model is calibrated to the laboratory mechanical properties of the Cobourg limestone. The calibration is conducted by simulating the laboratory experiments used to determine the laboratory properties of the rocks. The most important mechanical parameters that control stability of the underground excavation are UCS and Young's modulus (stiffness). The micro-mechanical parameters of the Voronoi block model are adjusted in order to match the stiffness and strength of the intact Cobourg limestone (Table 2).

The following are the micro-mechanical parameters that need to be determined in the calibration process:

contact normal stiffness.....	k_n
contact shear stiffness.....	k_s
block Young's modulus.....	E
block Poisson's ratio.....	ν
contact peak cohesion.....	c_p
contact peak friction	ϕ_p
contact peak tensile strength.....	T_p
contact residual friction.....	ϕ_r

The model parameters also include residual cohesion and tensile strength of the contacts. In all of the analyses discussed here, both of those parameters were considered to be zero in order to simulate the Cobourg limestone as a brittle material.

Matching of Young's modulus and Poisson's ratio and the macro-failure strength envelope defined by cohesion, friction angle and tensile strength, is an under-determined problem, because there are more micro-mechanical constants than constraints. The problem is resolved by assuming that the stiffness of the Voronoi blocks is much greater (approximate 10 times) than the stiffness of the contacts, meaning that the contacts are the main contributors to the compliance of the model. The other extreme also is analyzed, when the contacts are much stiffer than the blocks. The results of the two approximations are found to be quite similar (BSC 2004). In the case of the calibration of micro-mechanical strength parameters, additional constraints used to bound the solution were mode of failure and its evolution as a function of confinement, and post-peak behaviour (e.g., post-peak softening strain and residual strength). It was observed in unconfined laboratory tests that the Cobourg limestone fails predominantly by axial splitting. The post-peak behaviour recorded during experiments illustrates quite a brittle response of the Cobourg limestone after failure. Therefore, the micro-mechanical strength parameters used in the Voronoi block model were adjusted to result in a brittle sample failure.

The calibration was carried out on 5 Voronoi block samples generated using different realizations of random block geometry. The results of the numerical simulation of unconfined compression and direct tension are shown in Figure 8. The tests were carried out on 2.5 m edge square samples. It was not necessary to have a 2:1 height-to-width ratio for the tested samples, because perfectly frictionless boundary conditions were applied in the numerical tests on the loaded ends of the sample. (The height-to-width ratio of 2:1 is necessary in the laboratory

tests in which the platen friction cannot be made zero, to ensure unconfined stress state in the middle of the sample. In the numerical tests, the platen friction is exactly zero). The samples fail by axial splitting in the unconfined compression test. The Voronoi block model was calibrated to match the intact the Cobourg limestone properties determined on the laboratory scale samples. No strength reduction due to the scale effect was considered because the Cobourg limestone is homogeneous and massive rock. In addition, the bedding planes are explicitly represented in the numerical model.

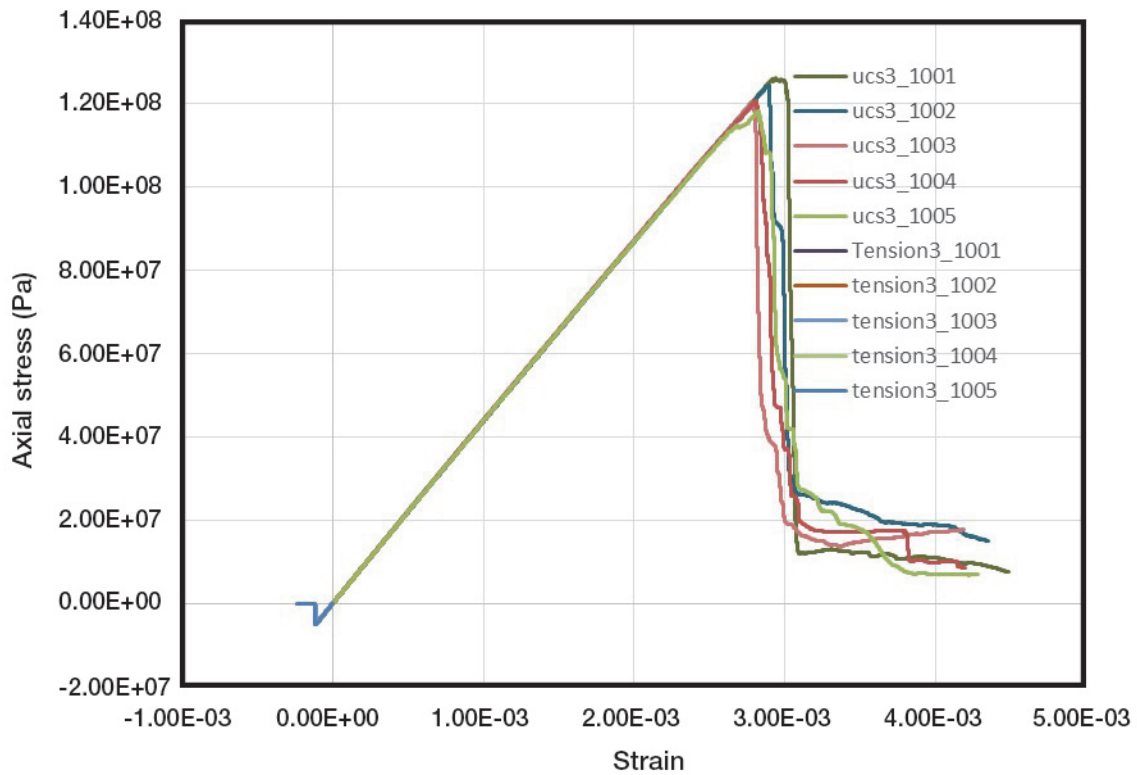


Figure 8: Axial Response Obtained from the Numerical Tests on Calibrated Voronoi Block Model of Cobourg Limestone (Compression Positive)

The stiffness and strength parameters that represent the properties of the Voronoi block samples under unconfined conditions are summarized in Table 5. The Young's modulus of 43.1 GPa, the UCS of 122 MPa, and tensile strength of 4.9 MPa, which are averages calculated from the results for five Voronoi block samples, are in good agreement with the target values of 43.5 GPa, 121 MPa, and 4.7 MPa respectively, for the intact Cobourg limestone listed in Table 2.

Table 5: Summary of Voronoi Stiffness and Strength Parameters from Unconfined Tests

Voronoi Block Random Number Generation Seed	UCS MPa	Tensile strength MPa	E GPa
1001	126	5.10	43.0
1002	124	4.70	43.0
1003	120	4.70	43.3
1004	120	5.10	43.0
1005	118	5.00	43.0
UDEC average	122	4.92	43.1
DATA	121	4.70	43.5
error	0.3%	4.5%	-1.0%

The Voronoi samples were tested also for compressive strength for two different values of confining stress (15 MPa and 30 MPa). Increase in confinement results in strength increase. The post-peak behaviour observed in the numerical tests for three compression tests is also quite different. Unconfined response is brittle (Figure 8). At 15 MPa and 30 MPa confinements, the response of synthetic material is softening (see Figure 9). However, the material becomes less brittle (compared to unconfined conditions) as manifested in increased residual strength and critical softening strain (i.e., the plastic strain required for material to be degraded to the residual strength). The brittleness decreases with increase in confining stress. The obtained peak strengths of 190 MPa and 240 MPa at confinements of 15 MPa and 30 MPa, respectively, are in good agreement with the test results on confined samples of the Cobourg limestone (reported in Figure 3.8 by Itasca, 2011).

To ensure that the numerical model does not overestimate the strength of the rock and does not yield unconservative predictions of failure of excavations, it is necessary that the model has: 1) equal or lower yield strength, 2) equal or more brittle post-peak response and 3) equal or lower residual strength, compared to the mechanical behaviour of the analyzed rock mass. The post-peak response of the Cobourg limestone from numerical simulations during calibration for 5 realizations of Voronoi block geometry is almost perfectly brittle, with the residual strength less than or equal to 15% of the peak strength. Thus, the post-peak behaviour of synthetic Voronoi block model is a reasonably conservative approximation of the mechanical behaviour of the Cobourg limestone.

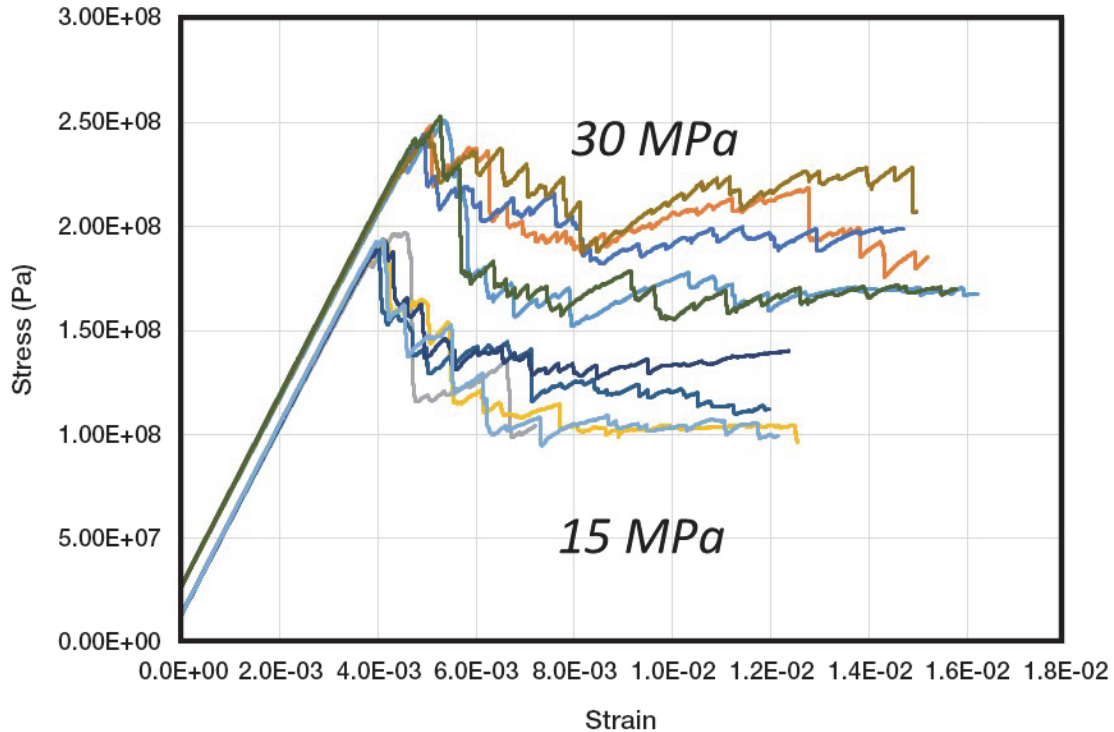


Figure 9: Confined Response (for 15 MPa and 30 MPa Confinement) Obtained from the Numerical Tests on Calibrated Voronoi Block Model of Cobourg Limestone (Compression Positive)

The model response (including the calibration tests) will not be identical between different realizations of the block geometry (as illustrated in Figure 8 and Table 5), because the geometry of the Voronoi blocks is random. Although there is variability between different block geometry realizations in the model response, it is important that variability is relatively small, within 10% of the mean. The variability for 5 samples used in the calibration is less than 5%, which is much less than the variability of the typical laboratory test results.

The calibrated micro-mechanical properties for Cobourg limestone are listed in Table 6. Those properties were assumed to be uniform throughout the model (or the sample). The effect of spatially variable properties (i.e., normally distributed joint peak cohesion and tension with a standard deviation between 10% and 30% of the mean) on the mechanical behaviour of the Voronoi block model, which also was investigated, was not significant, therefore it was not considered justifiable to introduce that as an additional complexity into the model.

Table 6: Calibrated Micro-mechanical Properties for the Voronoi Blocks and Contacts

Unit	Cobourg
Contact Normal Stiffness k_n (GPa/m)	740
Contact Shear Stiffness k_s (GPa/m)	370
Block Bulk Modulus K (GPa)	110
Block Shear Modulus G (GPa)	83
Block Young's Modulus E (GPa)	199
Block Poisson's Ratio ν	0.2
Contact Peak Cohesion c (MPa)	60
Contact Peak Friction ϕ_p ($^\circ$)	35
Contact Peak Tensile Strength T (MPa)	8.5
Contact Residual Friction ϕ_r ($^\circ$)	15

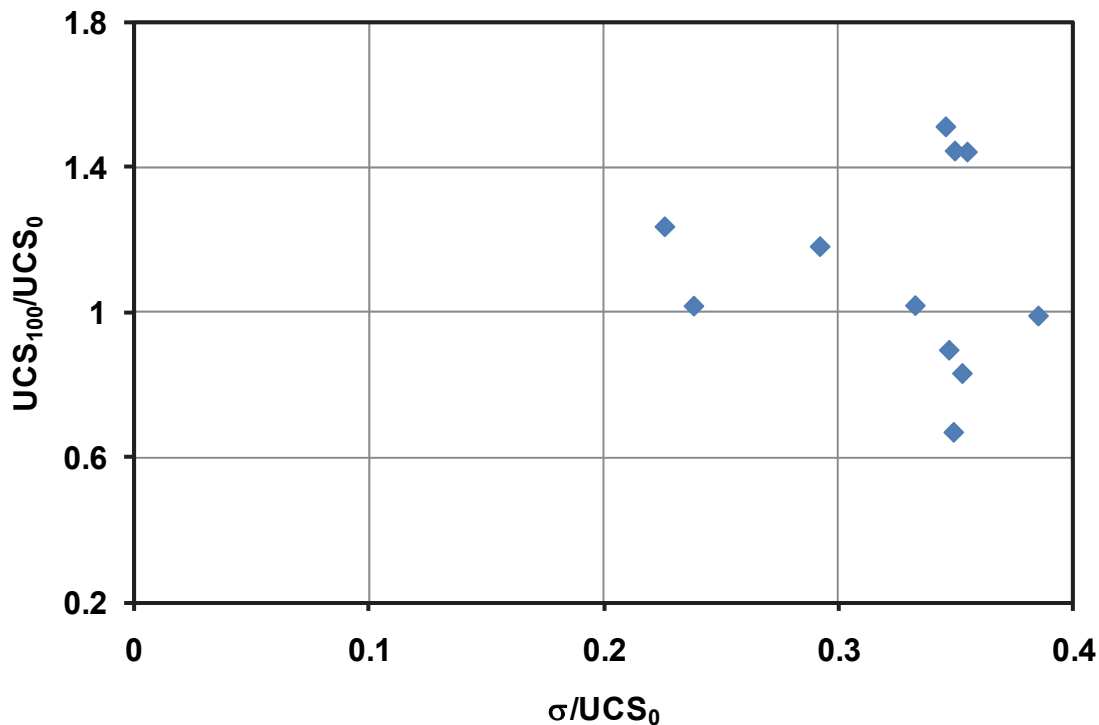
Notes: Residual micro-tension and cohesion are assumed to be zero.

3.1.5 Long-Term Strength

In the analysis of the long-term performance of the placement rooms, an important factor could be time-dependent strength degradation. It was observed that rocks loaded at certain stress, smaller than the short-term strength (typically measured in laboratories), but greater than the long-term or true strength, can fail if that stress is maintained for a sufficiently long time period. If the stress is equal to or less than the long-term strength (a fraction of the short-term strength), the rock will not fail, irrespective of the stress (load) duration. In the static-fatigue tests, the samples are loaded by the load smaller than their short-term strength. That load is maintained constant until the sample fails, which is recorded as the time-to-failure.

The objective of the long-term tests carried out on the samples taken at the Bruce nuclear site was to determine the long term strength of the rock (i.e., the stress at which their strength does not degrade with time), not the complete static-fatigue (or time to failure) curves. The long-term strength testing of the Cobourg limestone was carried out on the samples taken from DGR-2 (Gorski et al. 2009b), DGR-3 and DGR-4 (Gorski et al. 2010b). There were five tests on samples from DGR-2 and six tests from both DGR-3 and DGR-4. For each long-term test, a long specimen was cut into two pieces. One piece was tested instantaneously to obtain short term strength (UCS). The other piece was loaded at stress in the range between 0.2 and 0.4 of UCS. That load was maintained for 100 days, when the sample was loaded to failure. Thus, the test measures the change (decrease) in the rock strength (or damage accumulation) after 100 days of load at certain stress level. The results of long-term strength testing on all samples are presented in Figure 12. There is no obvious trend in data. Three measurements at approximately 0.35 UCS show some decrease in strength. However, other measurements at the same or greater load show increase in strength. The average of UCS100/UCS0 of all measurement is 1.11. That implies the effect of damage accumulation at the tested load levels

for 100 days is practically zero, or of the second order compared to natural variability of strength between relatively close samples. Based on existing test results, it can be concluded that there is no strength degradation for the loads less than or equal to 0.35 (of the mean) UCS or 42 MPa. Such a result is in agreement with unconfined test data (Itasca 2011), which show that the mean crack initiation stress, CI, is 41% of UCS. Many experts in the field believe that the lower bound value of the long-term strength of the rock is equal to or greater than crack initiation in unconfined compressive tests (Damjanac and Fairhurst 2010). Nickiar and Martin (2013) examined 376 laboratory tests. The average ratio of crack initiation to peak stress in igneous, sedimentary and metamorphic rocks, regardless of the mineralogy and grain size, was found to range from 0.42 to 0.47 in unconfined compression. In triaxial compression, the crack initiation stress ratio ranges from 0.50 to 0.54. Hence assuming a CI equivalent to long-term strength of sedimentary rock represents a lower bound value. In the present analysis, the long-term strength of Cobourg limestone is assumed to be equal to the mean CI of about 40% of UCS, 45 MPa.



Note: UCS_{100} normalized to the initial unconfined compressive strength (UCS_0) as a function of the long-term load (σ) normalized to the initial unconfined compressive strength (UCS_0).

Figure 10: Unconfined Strength of the Cobourg Limestone After 100 Days

3.1.6 Backfill Materials

The mechanical and thermal properties of the backfill materials, components of the engineered barrier system, are listed in Tables 7 and 8, respectively. In all analyses, the backfill materials are considered to be linearly elastic.

Table 7: Mechanical Properties for the Engineered Barrier Materials

Material	Composition	Bulk Density (kg/m³)	Dry Density (kg/m³)	Young's Modulus (GPa)	Poisson's Ratio
Buffer – HCB	100% bentonite	1880	1610	0.1	0.1
Buffer pellets – GF	100% bentonite	1439	1410	0.1	0.1
Dense Backfill – DBS	70:25:5 Aggregate:clay:bentonite	2276	2120	0.2	0.1

Table 8: Thermal Properties for the Engineered Barrier Materials

Material	Composition	Thermal Conductivity (W/m°C)	Specific Heat (J/kg°C)	Linear Coefficient of Thermal Expansion (1/°C)
Buffer – HCB	100% bentonite	0.5	1440	2×10^{-4}
Buffer pellets – GF	100% bentonite	0.4	910	2×10^{-4}
Dense Backfill – DBS	70:25:5 Aggregate:clay:bentonite	0.8	1110	2×10^{-4}

3.2 GEOLOGICAL AND REPOSITORY INDUCED PERTURBATIONS

The long-term stability of the placement rooms is analyzed considering different processes and loads that can affect their stability over a period of 1 Ma, including in situ stresses, time-dependent strength degradation, pore pressures (inside the rock mass), gas pressures (inside the placement rooms) and multiple glacial and seismic events. The analysis has been carried out for in-situ stresses, thermal loading, time-dependent strength degradation, pore pressures in rock mass and multiple glacial ice sheet advances and retreats occurring concurrently as the base case.

The different loading conditions considered and their representation in the models are discussed in this chapter.

3.2.1 In Situ Stresses

Extensive stress measurements have been carried out at shallow depths in the Southern Ontario for geological conditions representative of the sedimentary geological setting. The stress tensor at the repository depth has been constrained by these local stress measurements, stress measurements at the Norton Mine (at depth of approximately 670 mBGS), repeated borehole televiwer surveys at the Bruce site and extensive bounding analyses (Itasca 2011). As one of the initial steps in the numerical modelling, an attempt to gain further insight into the range of in situ stress conditions was made. A simple three-dimensional model of the stratigraphy at the proposed DGR site was used to evaluate the effect of tectonic strains on the distribution of stresses in the different stratigraphic units (Cartwright 1997). The stresses developed in the model then were verified by comparison with limiting stress conditions, estimated from borehole breakout observations and other data from the literature.

The in situ stress estimates from several sources were available. Adams and Bell (1991) provided a summary of in situ stresses for the St. Laurence Platform, with a proposed stress distribution. In situ stress gradients pertinent to the DGR site were provided by a survey of the Canadian In-Situ Stress Database compiled by Arjang (2001) and reviewed specifically for the DGR site by Kaiser and Maloney (2005). Bauer et al. (2005) describe the in situ stresses measured using the USBM overcore method at the Norton Mine, near Akron, Ohio. The room-and-pillar limestone mine is located within the 15 m thick Columbus limestone formation ($E = 49 \text{ GPa}$ and $\nu = 0.25$) at a depth of 670 mBGS. The measurements indicated the following in situ stress field:

$$\sigma_H = 36.7 \text{ MPa (in N75}^\circ\text{W direction)}$$

$$\sigma_h = 28.3 \text{ MPa (~1.26 times overburden)}$$

$$\sigma_v = 22.5 \text{ MPa}$$

Valley and Maloney (2010) used a comparison of the strength of the various rock units with the extent of borehole breakouts from televiwer observations to bound the in situ stress profile at the Bruce nuclear site, the proposed Low and Intermediate Level Waste Repository for OPG.

The in situ stresses at the Bruce nuclear site were evaluated using a simple model of the DGR stratigraphy. The model was set up to be orientated in the direction of the in situ principal stresses (maximum stress oriented approximately NE-SW). It was then strained horizontally with constant velocity in both horizontal directions to simulate the tectonic forces. A total strain

of 5.16×10^{-4} in the maximum horizontal stress direction and 2.84×10^{-4} in the minimum horizontal stress direction produced a good match to the in situ stress data.

The same tectonic strains calibrated at the DGR site are used for estimation of the in situ stresses at the repository in the sedimentary geological setting. The horizontal stresses are calculated for each layer as a function of depth using the elastic relations between stresses and strain:

$$\begin{aligned}\sigma_{xx} &= \frac{E}{1-\nu^2} (\varepsilon_{xx} + \nu\varepsilon_{yy}) + \frac{\nu}{1-\nu} \sigma_{zz} \sigma_{xx} = \frac{E}{1-\nu^2} (\varepsilon_{xx} + \nu\varepsilon_{yy}) + \frac{\nu}{1-\nu} \sigma_{zz} \\ \sigma_{yy} &= \frac{E}{1-\nu^2} (\nu\varepsilon_{xx} + \varepsilon_{yy}) + \frac{\nu}{1-\nu} \sigma_{zz} \sigma_{yy} = \frac{E}{1-\nu^2} (\nu\varepsilon_{xx} + \varepsilon_{yy}) + \frac{\nu}{1-\nu} \sigma_{zz}\end{aligned}\quad (2)$$

where E and ν are Young's modulus and Poisson's ratio of the particular layer of the sedimentary profile, $\varepsilon_{xx} = 2.84 \times 10^{-4}$ is the tectonic horizontal strain perpendicular to the placement room axis and $\varepsilon_{yy} = 5.16 \times 10^{-4}$ is the tectonic horizontal strain along to the placement room axis. The vertical stress, σ_{zz} , is gravitational and statically determined. Thus, it was possible to initialize the vertical stress for each zone in the model based on the weight of the overburden. The stress changes caused by the glaciation, discussed in Section 3.2.4, act as additional stresses relative to the in situ gravitational and tectonic stress discussed in this section.

3.2.2 Thermal Loading

The characteristics of the UFC for Mark II are listed in Table 9. The heat release rates per UFC and per unit volume of the UFC for a post-reactor discharge time of 30 years (i.e., the waste placement time) are listed in Table 10. The heat release rates listed in the table were considered as the initial heat release rates in the analysis. In the near-field models, which is 3D and explicitly represents the UFC, the thermal heat source is represented as the heat release rate per unit volume assigned to the model zones within the UFC. In the far-field model, the heat source is distributed over the layer of the zones that covers the panel layout in the plan view. The height is equal to the difference between the top coordinate of the upper layer of the UFC and the bottom coordinate of the lower layer of the UFC. The volumetric heat source for the far-field models is calculated by averaging the power of the single UFC over the tributary area in the plan view (i.e., center-to-center spacing between the adjacent UFC times the center-to-center spacing of the placements rooms).

Table 9: Waste Package Characteristics for Mark II Design

Bundles / Container	48
Total Shell Length	2.515 m
Diameter	0.565 m
Cylinder Surface Area	3.459 m ²
Lids Surface Area	1.002 m ²
TOTAL SURFACE AREA	4.462 m ²
TOTAL VOLUME	0.583 m ³

Table 10: Heat Release Rate at Time of Placement (post-reactor discharge time of 30 years)

	Single container W	Per unit volume of container W/m ³	Per unit volume of zone in far-field model W/m ³
Mark II	169	301	7.05

The heat release rate (or power) decays with time as a result of radioactive decay of the waste. The decrease of the power, relative to the power at time of placement, is illustrated in Figure 11. The multiplier given by this chart is used to scale the heat release rates as a function of time in all of the thermal models.

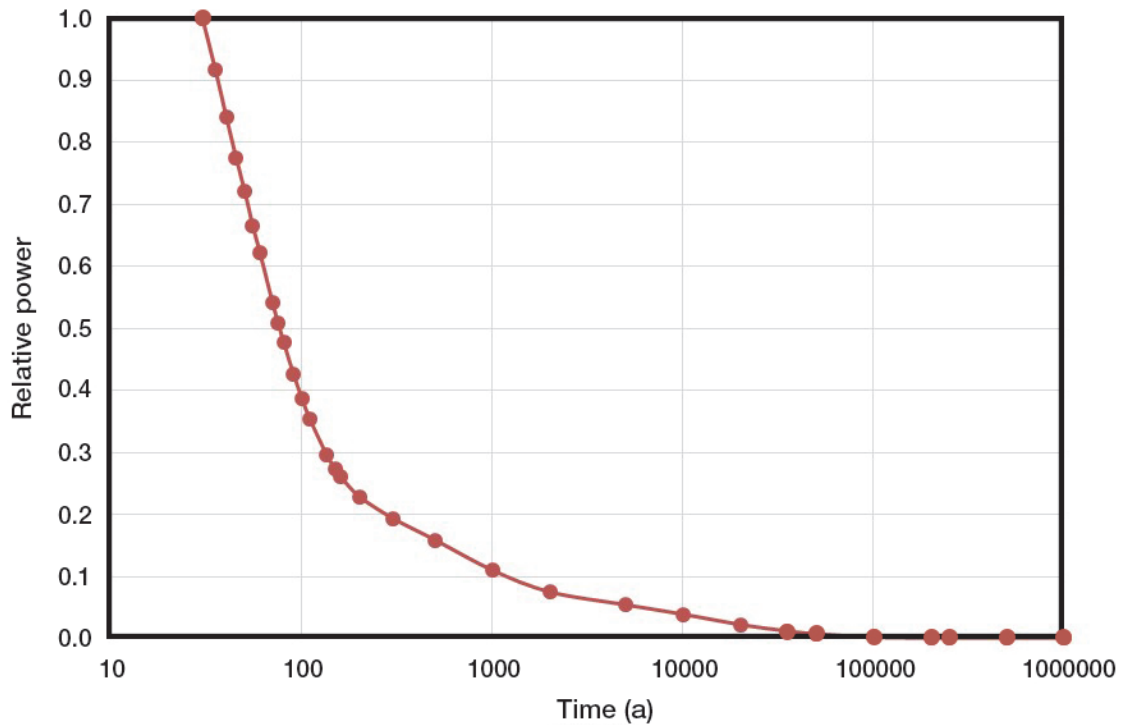


Figure 11: Power Decay as a Function of Time

3.2.3 Long-Term Strength Degradation

One objective of the analysis presented here is to predict degradation of and development of the EDZ around the placement rooms due to long-term (1 Ma) rock-strength degradation of the host rock units around the repository excavations subjected to in situ and glacially-induced stresses.

3.2.3.1 Static-Fatigue Curves and Evolution of Damage Due to Strength Degradation

The static-fatigue (long-term) behaviour of a rock forms the basis of the model for simulating time-dependent processes. The static-fatigue curves, which are obtained from laboratory tests

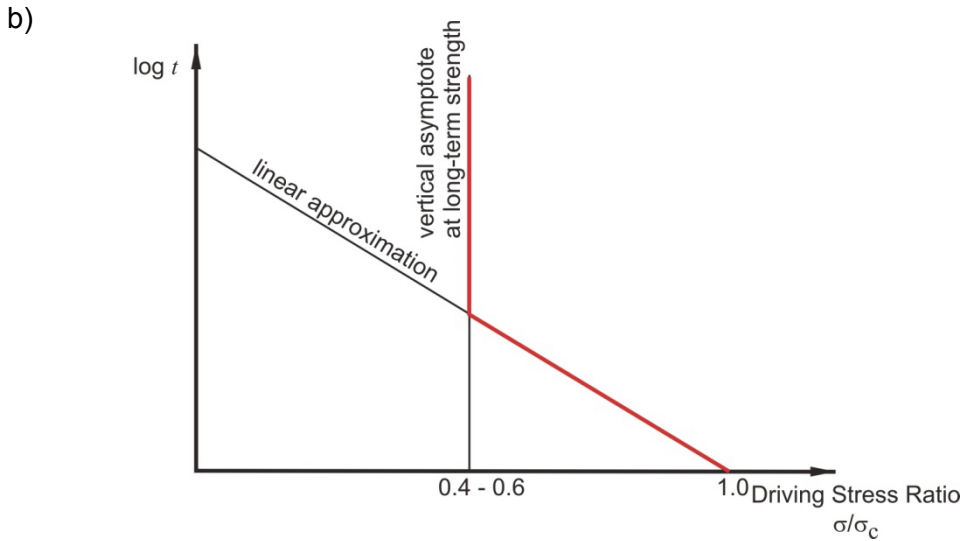
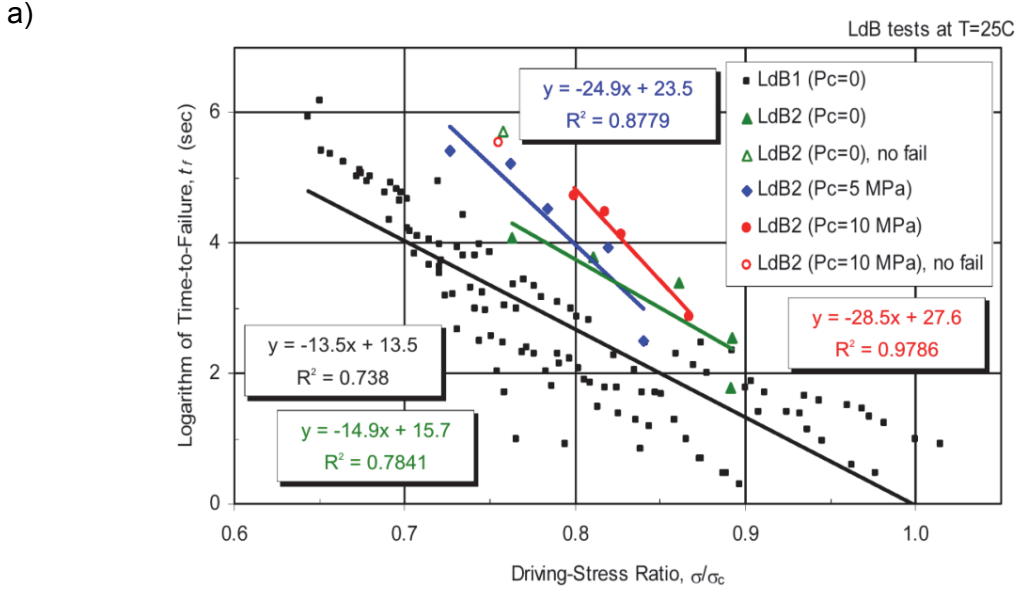
on small samples, provide the time-to-failure (t_f) of the material at a particular driving-stress ratio (σ / σ_c)¹.

There are few static-fatigue datasets to evaluate if rock type has any influence on the slope of the static-fatigue curve. Schmidtke and Lajtai (1985) established the static-fatigue relation for unconfined Lac du Bonnet granite (LdB) and Lau et al. (2000) evaluated the static-fatigue relation for confined (5 MPa and 10 MPa) samples (Figure 12a). Data sets for each confinement were fit with a straight line, and the line was extrapolated to encompass driving-stress ratios measured. The approximation of static-fatigue line as used in the long-term stability analyses is shown in Figure 12b.

Limited time-dependent testing was carried out for the Cobourg limestone. The primary purpose of this testing was to assess the long-term strength threshold approximated by the crack initiation stress proposed by Damjanac and Fairhurst (2010). Consequently, all testing had driving-stress ratios that were between 0.2 and 0.4 of the UCS, or equal to or less than the crack initiation stress. No samples failed or showed strength reduction during 100 days of testing. Consequently, the long-term stability analyses were carried out assuming that the long-term strength is 45 MPa for the Cobourg limestone (see Section 3.1.5).

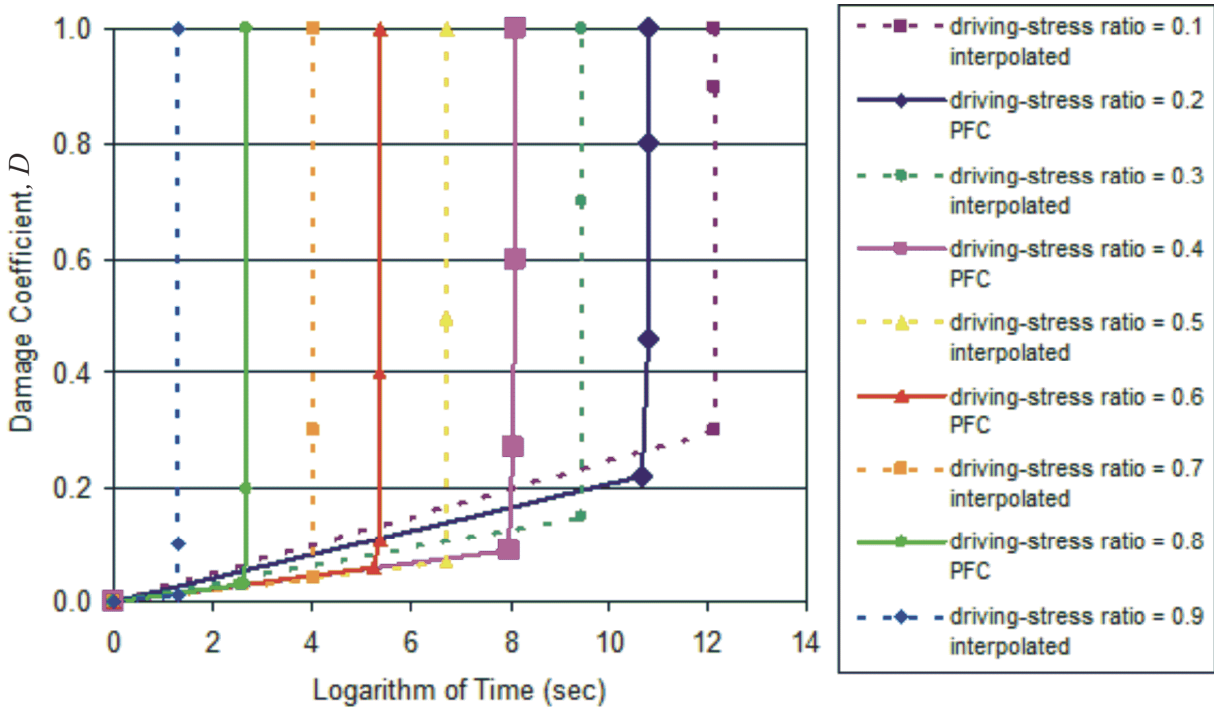
Once the lower-bound long-term strength was established, the next step was to develop a numerical process that degrades the short-term strength to the long-term strength. The evolution of damage, expressed in terms of the damage coefficient, D , which is the ratio of the degraded to the initial strength, for the Lac du Bonnet granite was developed using the discrete element software PFC (Itasca 1999, BSC 2004) and is shown in Figure 13.

¹ The following notation is employed to describe the results of static-fatigue tests. The applied load in the axial direction and the confining pressure are denoted by σ_1 and P_c , respectively. The axial load at failure during a short-term test is denoted by σ_f . The stress difference maintained during a static-fatigue test conducted at a confining pressure of P_c is $\sigma = \sigma_1 - P_c$. The stress difference at failure during a short-term test is $\sigma_c = \sigma_f - P_c$. To facilitate comparison between different data sets, we generate a static-fatigue curve by plotting the logarithm of time-to-failure, t_f , versus the driving-stress ratio given by $\sigma / \sigma_c = (\sigma_1 - P_c) / (\sigma_f - P_c)$.



Notes: a) Laboratory static-fatigue data for Lac du Bonnet granite established by Schmidtke and Lajtai (1985) for unconfined conditions (LdB1) and Lau et al. (2000) for unconfined and confined conditions (LdB2). b) The static-fatigue curves (red line) for a rock mass based on the approach by Damjanac and Fairhurst (2010).

Figure 12: Bases and Approximation of Rock Mass Static-fatigue Curves Used in Long-term Room Stability Analyses



Notes: Each curve has a vertical asymptote at a time-to-failure for a given driving-stress ratio, which is provided by the LdB ($P_c = 0$) curve from Figure 4.2a. The evolution of damage up to the vertical asymptote (i.e., the failure time) is provided by the PFC time-dependent model.

Figure 13: Damage Curves Used as Input to the UDEC LdB Analyses ($P_c = 0$)

Two parameters control the predictions of time-dependent strength degradation and, eventually, the predictions of rockfall: 1) time-to-failure, and 2) damage evolution (rate) before time-to-failure. Time-to-failure as a function of the stress state (i.e., the driving stress) is determined from the static-fatigue lines constructed by interpolation and extrapolation of the only available comprehensive testing results (obtained on Lac du Bonnet granite) and from the test data on the long-term strength obtained on the Cobourg limestone. Damage rates at different stress levels are generated using the PFC stress corrosion model. There is concern about the level of uncertainty in PFC predictions and how the damage rates affect the final result of the model (i.e., the rockfall induced by time-dependent strength degradation). In order to investigate the sensitivity of the model predictions to the damage rate, new damage curves are generated where the damage rates for all driving stress levels are assumed to be the same, equal to the maximum rate predicted by PFC. The rockfall predictions due to time-dependent strength reduction, using different damage curves, are compared (BSC 2004). It was confirmed that the considered variation of damage rates has no practical effect on predicted rockfall. Time-to-failure is the main factor controlling evolution of the rockfall due to time-dependent strength reduction. Consequently, predictions are not very sensitive to the input from the PFC stress corrosion model.

3.2.3.2 Time-dependent Strength Degradation in UDEC

Implementation of the time-dependent strength degradation scheme in the room stability model, which uses UDEC Voronoi block model (Section 3.1.3), is discussed in detail in this section. The implementation of the approach used in FLAC3D (the continuum code) for Mark I design

analysis is practically identical. The only difference is that in the continuum model the cohesion and tensile strength of strain-softening Mohr-Coulomb constitutive model are reduced to account for time-dependent strength degradation.

The long-term strength degradation of the Cobourg limestone units was implemented in the UDEC model by incrementally referencing a series of tables defining evolution of damage due to strength degradation as obtained from the PFC time-dependent model (Figure 13). Based upon the local driving-stress ratio at the Voronoi block contacts within the UDEC model, the strength of the contact in the model is degraded as a function of time. The times considered were 1, 2, 5, 10, 20, 50, 100, 200, 500, 1,000, 200, 5,000, 10,000, 20,000, 50,000, 100,000, 200,000, 500,000 and 1 Ma.

Time-dependent strength degradation in the UDEC model is generalized by a damage coefficient, D , which is in the range between zero and one. The cohesion and tensile strength of the material are assumed to be functions of time:

$$\begin{aligned} c(t) &= c_0 D(t) \\ T(t) &= T_0 D(t) \end{aligned} \quad (3)$$

where: c_0 and T_0 are the initial, short-term cohesion and tensile strength of contacts in the UDEC model, respectively. The large-scale short-term strength of the UDEC synthetic model of the rock mass is proportional to the cohesion and tensile strength of the contacts, c_0 and T_0 , respectively. Consequently, the time-dependent strength of the UDEC synthetic model of rock mass will decay proportionally to $D(t)$.

It is assumed that, in the general case:

$$\frac{dD}{dt} = f(F, D) \quad (4)$$

where: F , a function of stress state and material strength, defines the driving stress. For unconfined stress conditions (i.e., $P_c = 0$), function F must be identical to the ratio of the axial load and the unconfined short-term strength: $F(P_c = 0) \equiv \sigma_1 / \sigma_f$. The load at failure during a short-term test is calculated as follows (Jaeger and Cook 1979, pp. 95 – 97):

$$\begin{aligned} \sigma_f &= P_c N_\phi + 2c\sqrt{N_\phi} \\ N_\phi &= \frac{1 + \sin \phi}{1 - \sin \phi} \end{aligned} \quad (5)$$

where: c and ϕ are the rock mass cohesion and friction angle, respectively. It is assumed that if time-to-failure for two different stress states were the same, then evolution of damage due to strength degradation for both states as a function of time would be the same, irrespective of the confinement. As discussed in this section, given the time-to-failure, the model predictions are not very sensitive to the assumption pertaining to the functional form of damage evolution. Based on the laboratory data of Lau et al. (2000) and Schmidtke and Lajtai (1985), the slope of

the static-fatigue line, $k(P_c) = \Delta(\sigma / \sigma_c) / \Delta \log(t_f)$ is sensitive to the confining pressure. For example, the slope k of the static-fatigue lines for LdB granite (see Figure 12) is 0.051/log(s) for unconfined and 0.031/log(s) for 5 MPa confined conditions.

Given the conservative nature of the static-fatigue approach, it was assumed that linearizing the dependence of the slope k on confinement P_c was a reasonable simplification due to the observation that failure and damage usually take place at low confinements. The form of function F used in the UDEC model to capture the static-fatigue time-dependent induced damage is:

$$F = 1 - \frac{k(0)}{k(P_c)} \left(1 - \frac{\sigma}{\sigma_c} \right) \quad (6)$$

The damage evolution $D(F;t)$ was generated using PFC for values of function F in the range between zero and one, and used as the UDEC input data in a tabular form (see Figure 13). Interpolation was carried out for stress states in the model during the simulation, for which function F did not coincide with values for which the tables were provided. This is reasonable given the data in Figure 13 are generated for a small driving-stress increment of 0.1.

It is convenient for numerical implementation in UDEC that the damage increment in Equation 6 depends on accumulated damage, which is a function of the stress history. Although the stress state (at a given point) can have a complex history as a function of time (due to stress redistribution), it is sufficient to only keep track of accumulated damage in the simulation. The calculation of the damage increment in the UDEC simulation was carried out in the following manner: (1) for the time increment Δt , it is assumed that the stress state and the stress function, F , at a given point in the model are constant, $F = F_i$ (2) the table of damage evolution $D(F;t)$ is selected or interpolated based on tables provided (3) a point on the damage evolution curve corresponding to accumulated damage D_i is determined $D_j = D(F_i; t_j)$ and (4) the damage increment is calculated as:

$$\Delta D = D(F_i; t_j + \Delta t) - D(F_i; t_j) \quad (7)$$

Time increment(s) for the simulation must be selected. The only criteria for selection are the accuracy of the simulation and calculation time. The stress state is assumed to be constant during the time increment. Preliminary investigations showed that selected time increments did not affect model results significantly.

Damage is calculated and accumulated for the Voronoi contacts to simulate the rock mass strength degradation with time. The stress state used for calculation of the damage is determined by averaging stresses in the blocks separated by a contact.

3.2.4 Glacial Loading

Canada has been subjected to glacial events over the past million years. These events, which occur periodically, are associated with the development of the ice sheet covering certain portions of the Earth's surface. The University of Toronto Glacial Systems Model (UofT GSM), which is a model of continental-scale glaciation events, was used by Peltier (2011) to develop a description of glaciation of the Canadian Shield as a means of assessing the impact that such

an event would have on performance of a nuclear waste repository. Different possible realizations of glaciation and deglaciation during the last 120,000 years were developed, and provide acceptable fits to the observed constraints. Based on these realizations, the maximum ice thickness over southern Ontario, where the potential repositories are planned, could have exceeded 2.5 km during the most southerly ice sheet advance (Peltier 2011).

These glacial models were used to assess how the formation of the ice sheet will affect the room and repository stability. The weight of the ice sheet will increase both vertical and horizontal normal stresses. Furthermore, as the ice sheet moves sliding at a relatively slow rate, it will impose additional shear stresses on the ground surface. The case that resulted in the greatest vertical stress (histories of all independent stress components shown in Figure 14) was used in the long-term stability analysis of the repository and the placement rooms. The time histories of the glacial loads are results of a glaciation and earth crust deformation models by Peltier (2011) and Wu (2013) for the location of the hypothetical repository site in sedimentary rock. The stresses are calculated for 850 m depth but assumed to be valid for the repository depth of 500 m.

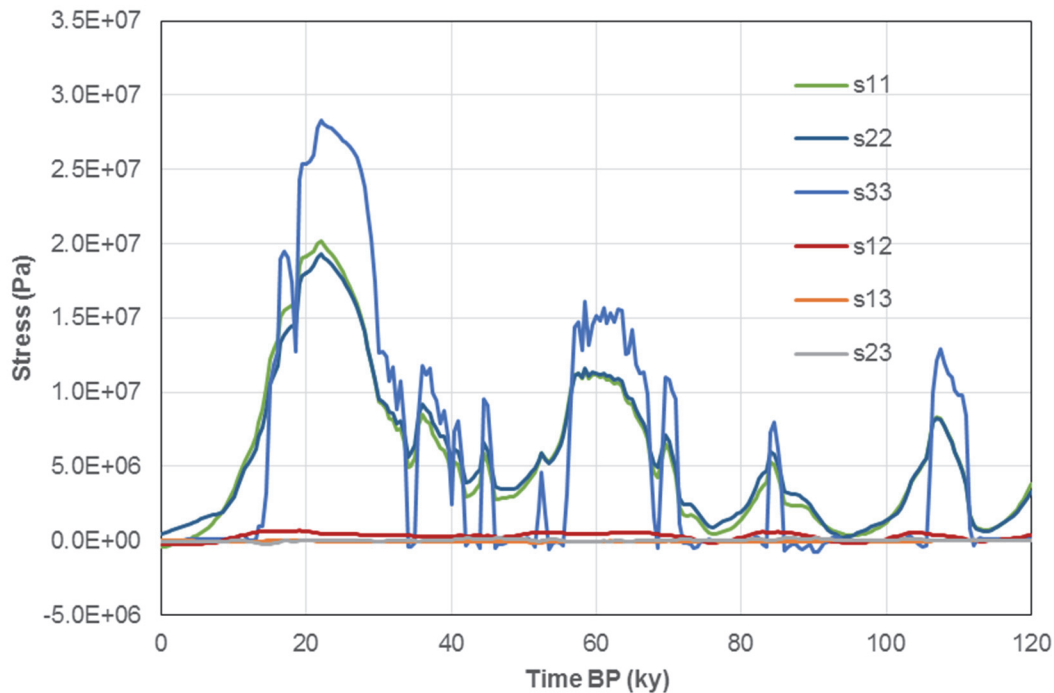


Figure 14: Calculated Glacially-induced Rebound Stress (BP = before present); s11, s22, and s33 are the Normal Stress Components, s12, s13, and s23 are the Shear Stress Components

The conditions for the next advance of continental scale glaciation will not be favourable for approximately another 60,000 years (Peltier 2011). However, predictions of possible variations of the ice thickness during future glaciations are not available. The analysis is conducted assuming that the sequence of the glacial events and corresponding histories of the rebound stresses predicted for the L9921-Lith075-UM6E20LM3E21 (Wu 2013) case will occur in future starting at 60,000 years after the present. The rebound shear stresses (s12, s13 and s23 in Figure 14) are much smaller than the normal stresses (s11, s22 and s33). Consequently, they

were neglected in the analysis. The rebound stress histories, as considered in the analysis, are shown in Figure 15. The x-axis shows the time relative to the onset of the glaciation, 60,000 years after the present. Each glacial rebound stress increment (including all three normal stress components) was read into the mechanical models to increment stress state throughout the domain that represents the rock mass. Subsequently, the model was run to equilibrium. The stress increments due to the rebound stresses were initialized (i.e., not applied as the boundary conditions). Consequently, the model does not predict the elastic rock mass deformation of the entire geological setting caused by the change in the glacial loading. Instead predicted are only elastic rock mass deformation at placement room horizon and inelastic deformation due to yielding and damage of the rock mass.

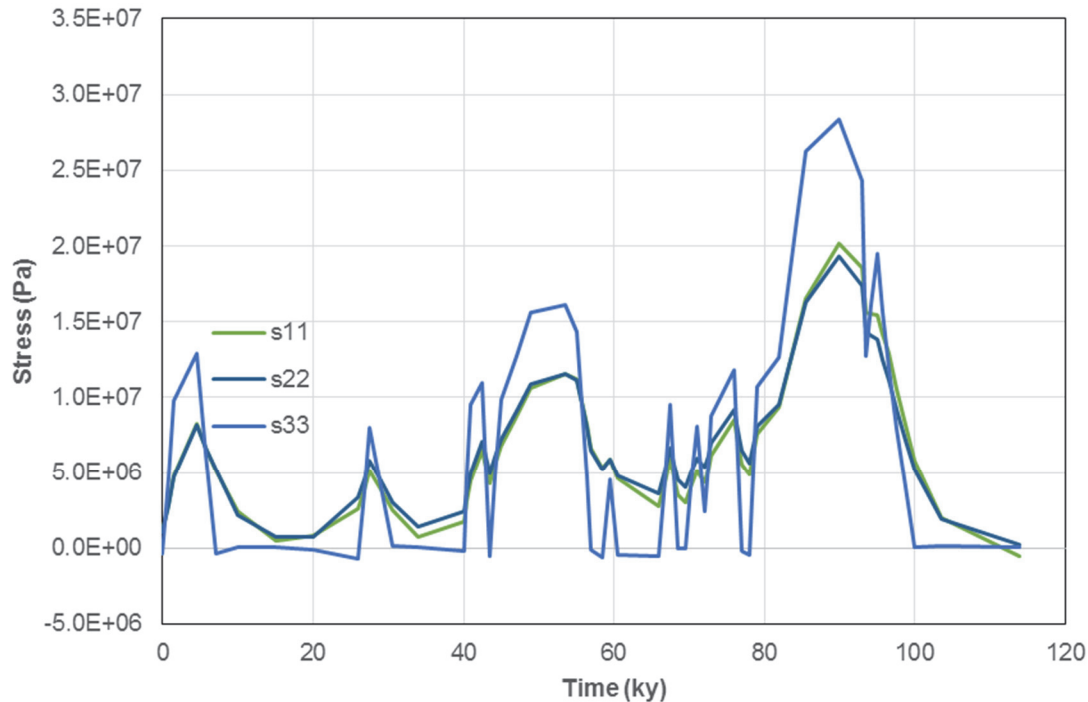


Figure 15: Approximation of Glacially-induced Rebound Stress Histories Used in Repository Stability Analysis

3.2.5 Gas and Pore Pressures

The initial pore pressure field was assumed to be hydrostatic, corresponding to the water table at the ground surface level. Excavation and operation of the repository will induce instantaneous and transient changes in the pore pressure in the rock mass and the gas pressure within the repository. For example, excavation of the placement room will cause instantaneous pressure changes in the pore pressure around the rooms due to undrained deformation of the rock. While the rooms are open, the fluid pressures around the rooms will gradually start to dissipate due to drainage into the rooms. Considering relatively small permeability of the Cobourg limestone, this drainage and pore pressure dissipation will be relatively slow. After placement of the waste packages, backfilling of the placement rooms, and closure of the repository, the ground water will gradually re-saturate the rooms and return to the hydrostatic state. Changes in temperature around the repository will also cause changes in the fluid pore pressures. However, those

pressure changes will occur gradually over time in parallel with pore fluid pressure dissipation processes. After approximately 10,000 years, the gas generation inside the rooms will result in increase in the gas pressure. Over certain period of time the gas pressure will exceed the hydrostatic water pressure, replacing the water from the placement rooms and percolating in the surrounding rock.

All of these processes and evolution of the gas and pore water pressures, coupled with mechanical deformation and temperature changes, can be analyzed using fully coupled thermo-hydro-mechanical models considering two-phase flow and the gas generation models. In this study, a simpler bounding approach is used described in the following sections.

3.2.5.1 Pore Pressures

The water pore pressure is assumed to be hydrostatic throughout the model, irrespective of the mechanical deformation, water seepage into the open rooms or temperature changes. This approximation is a conservative and reasonable approximation of relatively complex pore pressure evolution. When the room is excavated, the pressure inside the room is considered to be zero. As soon as the waste packages and the bentonite backfill are placed into the room, the pressure inside the room is re-initialized to hydrostatic as the ground water pressure inside the placement rooms gradually increases over time.

The pore pressure changes due to difference in coefficients in thermal expansion between the sedimentary rock and water were neglected in this analysis based on two arguments. Both heat conduction and pore pressure dissipation are transient processes occurring, in this case, over time scale of thousands of years and longer. It is reasonable to assume that significant portion of the pore pressure increase will dissipate (from the regions where pore pressures have increased due to temperature increase) as a result of fluid flow and partially equilibrate pore pressure fields around the placement rooms with hydrostatic pressure. In addition, any yielding (even micro cracking at crack initiation stress) in low-porosity rock like Cobourg limestone will result in instantaneous pore pressure drop, most likely to zero.

During the glacial cycles and increase in the vertical and horizontal stresses due to ice load and crustal deformation, the pore pressures are also assumed to increase uniformly throughout the model according to the following relation:

$$\Delta p = B \Delta \sigma \quad (8)$$

where B is the Skempton coefficient and $\Delta \sigma$ is the change in the mean stress. Detournay and Cheng (1993) suggested that $B = 0.7$ results in conservative estimate of the pore pressure change in low porosity rocks using Equation (8). The justification for this value based on poroelasticity and laboratory measurements is provided by Detournay and Cheng (1993).

3.2.5.2 Gas Pressures

Corrosion and microbial degradation of the wastes and packages inside the rooms will result in the generation of gases. Because of the low permeability of the host rock, a significant amount of gas will remain inside the repository, which could result in a gradual build-up of gas pressure. To estimate this gas pressure, custom gas-generation modelling (T2GGM v3.1) was used (Suckling et al. 2012).

T2GGM has been developed to simulate various microbial and corrosion processes, the gas evolution of the repository, and its interaction with the geosphere. The code calculates the

production and consumption of the key chemical species (e.g., metals, organic wastes, gases, water), as well as the fluxes of the water and gases into and out of the repository. T2GGM includes four key mechanisms for the generation of gas and consumption of water:

- 1) Microbial degradation of organic wastes;
- 2) Hydrogen reactions including methanogenesis;
- 3) Aerobic corrosion of metallic wastes; and
- 4) Anaerobic corrosion of metallic wastes.

These processes may occur when the repository is fully saturated or partially saturated with groundwater. The gas pressure was calculated conservatively by assuming that gas transport was limited to two phase flow through all repository materials, and that all used fuel containers suddenly lost their corrosion barrier of copper after 10,000 years. The gas pressure within the repository was estimated from completed for the fifth Case Study (NWMO 2013) for the Mark II designs. Pressures were calculated based on the equation of state of the generated gas and the available volume (also a function of material porosity) inside repository.

The principal results of the modelling as they relate to gas generation and water processes within the repository are summarized below.

- 1) Oxygen within the repository is consumed and conditions become anaerobic shortly after repository closure.
- 2) Moisture initially present in the wastes, plus water that seeps into the repository from the surrounding rock and the shaft, support corrosion of the steel in the Mark II containers resulting in generation of hydrogen gas.
- 3) The very low permeability of the rock slows groundwater entering the repository.
- 4) The peak repository gas pressure for the Mark II repository design is found to be 8.3 MPa. The peak gas pressure occurs at approximately 29,000 years, postclosure. The pressure decreases to lower than the steady state environmental head at the repository horizon of around 2.7 MPa for Mark II layout.

The gas pressure profile as considered in the models is illustrated in Figure 16.

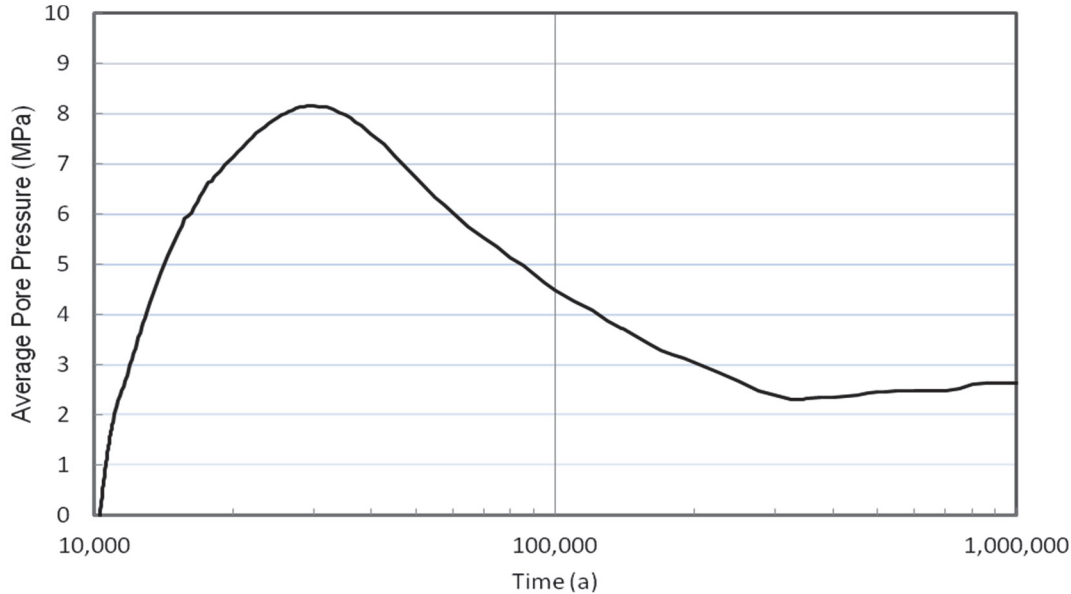


Figure 16: Repository Gas Pressure Profile Used in Geomechanical Stability Analyses for Mark II Repository Design

3.2.6 Seismic Loading

3.2.6.1 Ground Motions

Stability of the placement rooms was analyzed for seismic ground motions, which could be generated by earthquakes with an annual probability of exceedance of 10^{-5} p.a. (per annum) for the reference case and 10^{-6} p.a. for the extreme case. The ground motion time histories were developed for the ground surface, but also at depths of interest to be used as inputs as the ground motions at the base of the models for stability analysis. The ground motions used as the inputs to the analyses include the surface reflections, because the numerical models do not extend to the ground surface (i.e., they are truncated at some height above the structure of interest) and use the non-reflecting boundaries at the model top.

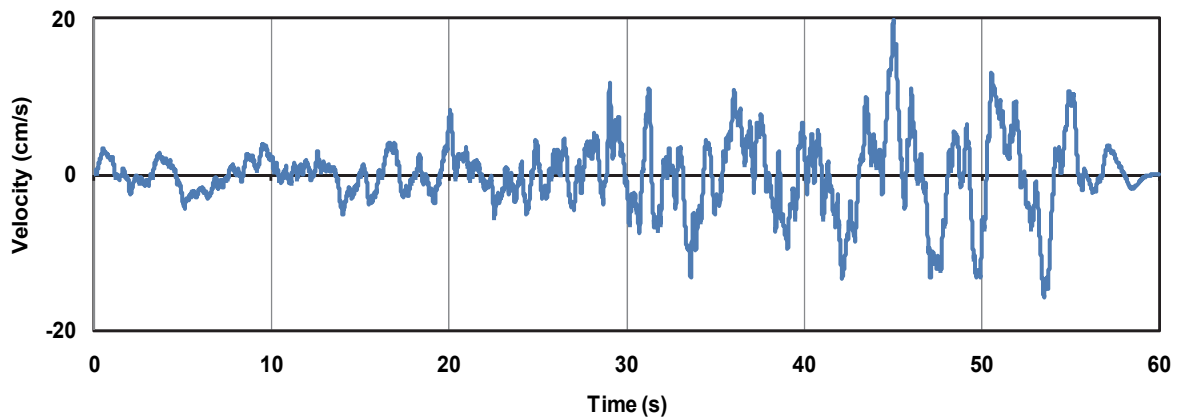
Conservative three dimensional ground motions generated for the DGR at Bruce nuclear site (at 680 m depth) were adopted in the modelling (AMEC Geomatrix 2011). There are three seismic scenarios with combinations of the earthquake magnitude and the distance from the repository that match the uniform hazard spectra at each probability level of 10^{-5} p.a. and 10^{-6} p.a. for the entire frequency range (AMEC Geomatrix 2011). Time histories for each seismic scenario include two horizontal components (H1 and H2) and one vertical component (V). The scenarios and the corresponding peak ground velocities (PGVs) and peak ground accelerations (PGAs) for each scenario and each motion component at the repository level are listed in Table 11. For example, the entire velocity time histories at the repository level for M7.4 event at 200 km distance are shown in Figures 17 through 19.

In summary, the maximum PGV of 22.1 cm/s at the repository level at 10^{-6} p.a. probability level occurs for M6.25 event at 25 km distance. The maximum PGA of 0.5g at the repository level at 10^{-6} probability level occurs for M5.25 event at 10 km distance. The maximum PGV of 11 cm/s at the repository level at 10^{-5} p.a. probability level occurs for M6.5 event at 100 km distance.

The maximum PGA of 0.16g at the repository level at 10^{-5} probability level occurs for M5.5 event at 20 km distance.

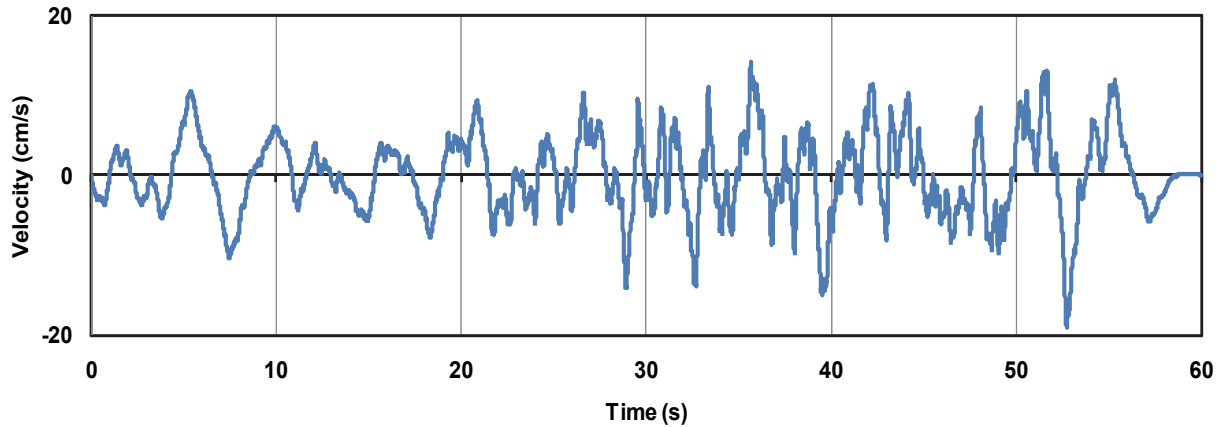
Table 11: Analyzed Seismic Scenarios with Corresponding PGVs and PGAs at the Repository Level (AMEC Geomatrix 2011)

Probability	Magnitude	Distance km	PGV (cm/s)			PGA (g)		
			H1	H2	V	H1	H2	V
10^{-5} p.a.	M5.5	20	3.3	4.1	2.5	0.15	0.16	0.11
	M6.5	100	6.8	11.0	6.0	0.09	0.10	0.08
	M7.4	300	9.5	8.8	5.7	0.05	0.05	0.04
10^{-6} p.a.	M5.25	10	8.1	9.8	6.3	0.45	0.50	0.36
	M6.25	25	14.4	22.1	11.8	0.37	0.36	0.28
	M7.4	200	19.8	19.1	12.0	0.12	0.12	0.09



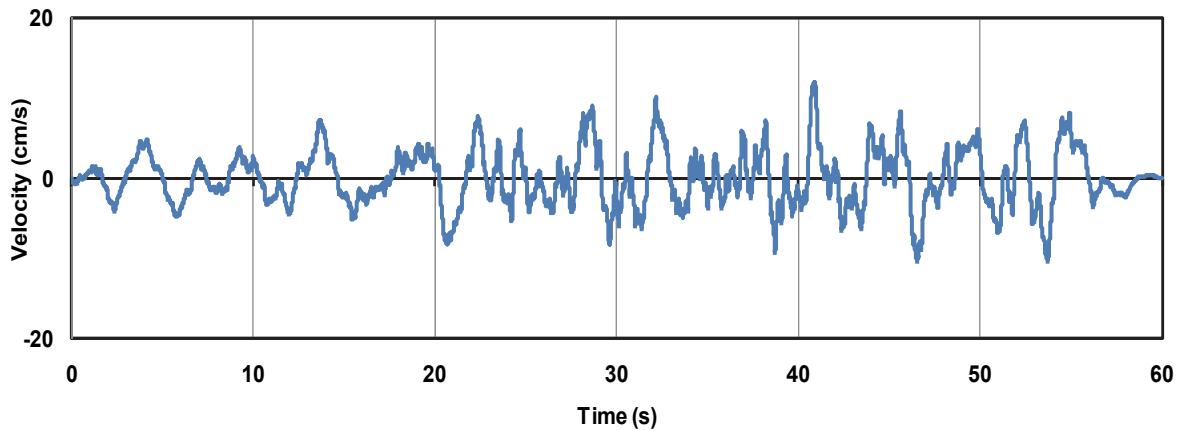
Note: Figure is from AMEC GEOMETRIX (2011).

Figure 17: Time History of Horizontal Velocity Component (H1) at the Repository Level for M7.4 at 200 km



Note: Figure is from AMEC Geomatrix (2011).

Figure 18: Time History of Horizontal Velocity Component (H2) at the Repository Level for M7.4 at 200 km



Note: Figure is from AMEC Geomatrix (2011).

Figure 19: Time History of Vertical Velocity Component (V) at the Repository Level for M7.4 at 200 km

For both probability levels, the duration of two closer events (within shorter distance) is 40 s. The duration of the third event is 60 s. In order to optimize the dynamic simulations, the seismic ground motions were not simulated for their entire durations. The seismic ground motions typically start and end with lower intensity. The strong motion and majority of the energy are within the middle portion of the time histories. Thus, the simulations were conducted for the interval between the time thresholds when 15% and 85% of the Arias intensity for the entire duration, T_d , of the ground motion are accumulated. The Arias intensity, I_A , defined as:

$$I_A = \frac{\pi}{2g} \int_0^{T_d} a^2 dt \quad (9)$$

where: a is acceleration and t is time, is a measure of the energy of seismic ground shaking. The simulation interval starts at the earliest 15%-threshold and ends at the latest 85%-threshold

among the three components, because there are three components of the ground motion. The calculated simulation times for the ground motions at the repository level are listed in Table 12.

Table 12: Simulation Times for Ground Motions at the Repository Level

Probability	Magnitude	Distance (km)	Start time (s)	Duration (s)
10 ⁻⁵ p.a.	M5.5	20	5.11	18.95
	M6.5	100	8.85	18.21
	M7.4	300	22.57	26.89
10 ⁻⁶ p.a.	M5.25	10	4.96	19.91
	M6.25	25	8.59	19.53
	M7.4	200	22.10	27.24

In the analyses of the placement rooms, only two components (one horizontal and one vertical) of the ground motion can be analyzed. The analyzed horizontal component acts perpendicular to the room axis. The other, neglected horizontal component, acts in the direction of the room axis and, consequently, should have insignificant effect on the room stability. Because the orientations of the two horizontal components of the ground motions are undetermined, it is always assumed that the horizontal component with greater PGV acts perpendicular to the room axis. (The maximum seismically induced damage and rockfall in the underground excavations are typically well correlated to the PGV.) Consequently, at both probability levels, the horizontal component H2 is used in two-dimensional analyses for two seismic scenarios within the shorter distance (see horizontal PGVs in Table 11). The horizontal component H1 is used for the third, the furthest seismic scenario at both probability levels.

3.2.6.2 Material Damping

All geological materials (e.g., soils and rocks) dissipate energy during cyclic deformation (e.g., caused by seismic loading) at all levels of shear strain. On the other hand, the constitutive models dissipate energy only when the strains exceed the yielding strain. Energy dissipation during cycling at relatively low strain amplitudes is accounted for through material damping, which in the case of geological materials, is hysteretic, or frequency independent, and typically in the range between 2% and 5% of the critical damping. The superposition of mass- and stiffness-proportional damping, called Rayleigh damping, provides hysteretic, frequency-independent damping over a certain frequency range. The problem with the Rayleigh damping is that it imposes severe restrictions on the calculation time step, making it more than 10 times shorter for typical damping ratios than in the case without Rayleigh damping. To avoid the excessively long simulation times and ensure that calculations are conservative, the placement room stability simulations were carried out using only local damping amounting to approximately 1.5% of the critical damping.

3.3 DESCRIPTION OF THE MODELS

3.3.1 Modelling and Coupling Approach

The modelling objective is to provide a bounding estimate of deformation and damage of the rock mass around the placement rooms and to assess the impact of predicted deformation and damage on performance of the repository in the sedimentary setting for period of 1 Ma. The analysis is conducted for expected in situ and repository-induced conditions and perturbations. Considering the nature of loading conditions and processes, coupled thermo-mechanical analyses are conducted.

Different simulations and their relation are illustrated in Figure 20. In order to optimize numerical simulations of coupled thermo-mechanical models, the thermal and mechanical models were simulated separately. Such approach was possible because the coupling is one-way. The thermal model affects the mechanical, but not the other way around (i.e., the effect of mechanical model on temperature changes is negligible). Thus, the thermal models were simulated first.

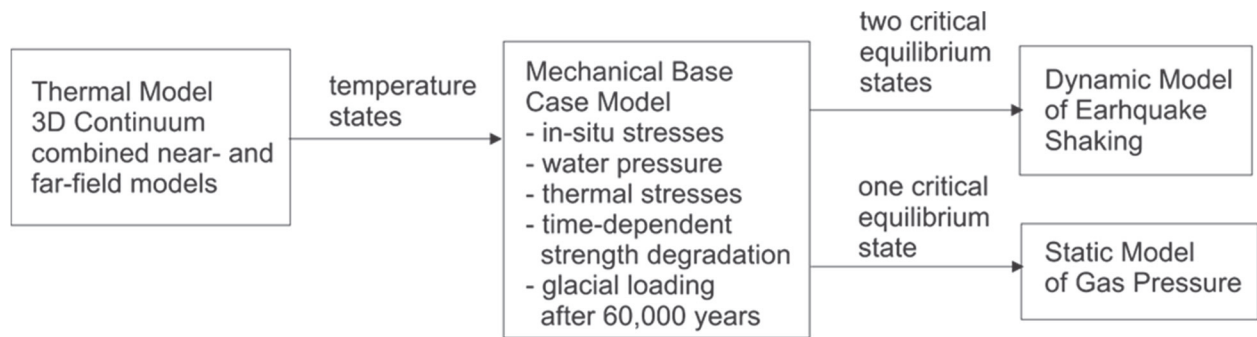


Figure 20: Numerical Model Simulation Chart

During the simulation of the thermal model, multiple model states were saved. The time increment between any two saved states was determined from the condition that the maximum temperature change in the model is equal to or less than 5°C. The temperature fields predicted in the thermal model were then sequentially imported in the mechanical model. The mean stress increment, $\Delta\sigma_m$, can be expressed in terms of temperature change, ΔT , bulk modulus of the solid material, K , and the linear coefficient of thermal expansion, α as:

$$\Delta\sigma_m = -3\alpha K\Delta T \quad (10)$$

The thermal analysis was actually conducted using two models: near- and far-field models. The near-field models represent the details of in-room and room geometries. They include only one placement room, but use a symmetry condition (adiabatic thermal boundary) at half-distance between the adjacent rooms to represent the repository with multiple rooms. Strictly, the used symmetry conditions is correct if the waste is emplaced in the entire repository in the same time. That assumption is reasonable given the relatively short duration of the waste placement compared to the time scales considered in the analysis and compared to the time scale before the drifts begin to thermally interact with each other. Thus, the near-field model at early times correctly approximates (with a small error) the temperature around the placement room. At longer times, the near-field model is a representation of temperatures assuming that there is an infinite number of the rooms on both sides of the analyzed room. This approximation results in

overestimation of temperatures for the long times. Therefore, the temperatures around the repository were also analyzed in the far-field models. In these models, the repository is represented as a planar heat source over the area of the repository panels, or the layer of zones on the repository level within the outline of the repository panels. Thus, the details of the in-room and the room geometries are not explicitly represented in the model.

Both near- and far-field models extend to the ground surface and 2,000 m below the ground surface. The far-field model extends laterally far enough that it can be assumed that the initial temperatures are insignificantly affected for simulated period of 1 Ma.

In the temperature fields used in the thermo-mechanical analyses, the transition from temperature fields predicted in the near-field model to those from the far-field model is made after 50,000 years. This is a conservative approximation because the near-field model overestimates the temperature around the repository after 2,000 years. The temperature fields from the near- and far-field models are imported into the mechanical model sequentially and used in calculation of the thermally induced stresses.

The placement rooms (the invert) and repository horizon are at 500 m depth. The models include the geological profile with all layers and their thermal properties as defined in Table 4. The temperatures at the base and the top of the models are fixed at the initial values based on thermal gradient measured in the deep boreholes during DGR Bruce nuclear site characterization (Intera 2011). The volumetric thermal source as defined in Table 11 (separately for the near- and far-field models) and by the decay curve (shown in Figure 11) is distributed over all elements (zones) that represent the UFC (e.g., “UFC” group in Figure 23), in the near-field models, and the repository panel, in the far-field models.

Different loading conditions, namely thermal loading, time-dependent strength degradation, glacial loading, and pore pressures, occur concurrently, and are modeled as such. Occurrence of earthquakes is a random process. The probability of an earthquake with 10^{-6} p.a. occurring at the same time as the maximum glacial loading is very small. Nevertheless, to assess an extreme loading scenario, earthquake loading of such probability was considered to occur coincidentally with the states of maximum stress caused by other loading combinations. For the purpose of presenting the results, and to reflect naturally occurring order of loading and loading combinations, the effects of certain loading conditions are separated.

3.4 MODELLING MARK II DESIGN IN SEDIMENTARY ROCK

3.4.1 Thermal Model

The details of the geometry of the near-field thermal model is are illustrated in Figure 21. (In the vertical direction, the model extends to the ground surface and to the depth of 2,000 m.) The model is created taking advantage of four planar symmetries of the analyzed problem. The vertical model boundaries are along those four symmetry planes. Two are perpendicular to the room axis: one through the center of the UFC in the lower row and the other through the center of the adjacent UFC in the upper row. Two other vertical model boundaries are parallel with the placement room axis. One of those boundaries is along the room axis; the other is at half-distance between two adjacent placement rooms. All four vertical model boundaries along the four planes of symmetries are considered as adiabatic in the thermal model.

The geometry of the far-field thermal model is shown in Figure 22. The plot illustrates all geological layers included and geometry of one panel. The repository layout includes four

panels. In this model, two planar symmetries are used. Only one panel is explicitly represented. Two vertical model boundaries are along the two mutually perpendicular symmetry planes between four panels. Those boundaries are considered adiabatic in the thermal model. Two other vertical boundaries are truncation boundaries at sufficient distance from the repository that temperature change during the simulated time of 1 Ma can be neglected. Those two boundaries are at 3,265 m and 3,511 m from the center of the repository. The thickness of the layer of the zones that represent the panel is 1.565 m, or the difference in the elevations of the top of the UFC in the upper row and the bottom of the UFC in the lower row.

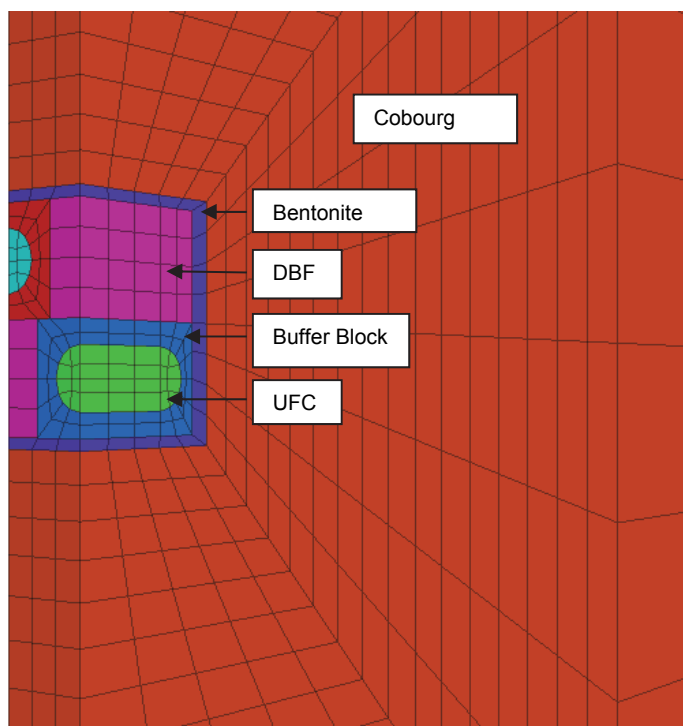


Figure 21: Detail of Geometry of the Near-Field Thermal Model in Sedimentary Rock

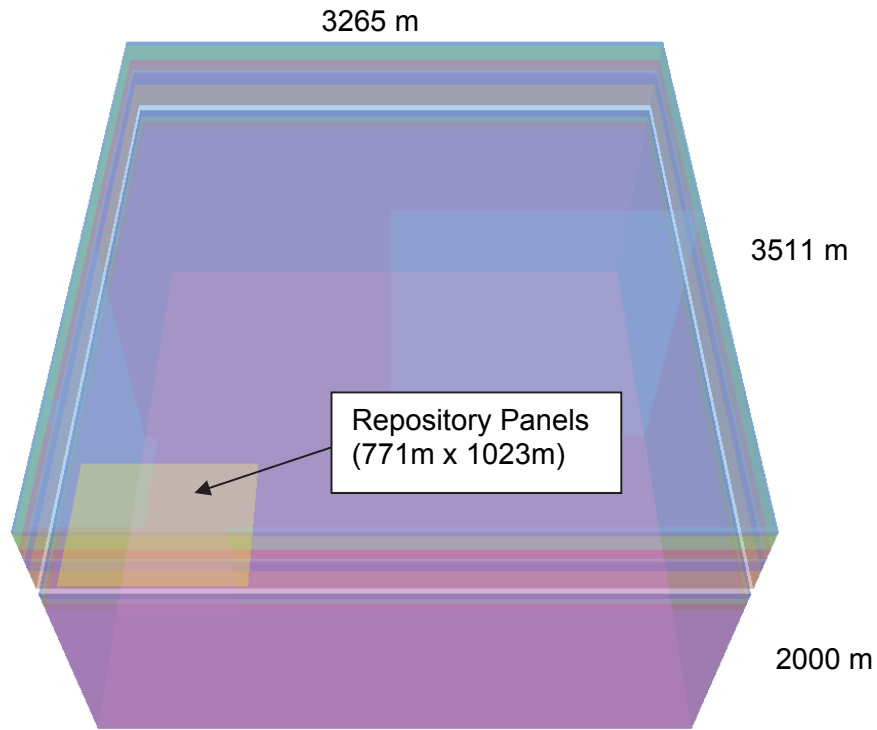


Figure 22: Geometry of the Far-Field Thermal Model in Sedimentary Rock

3.4.2 Mechanical Model

The deformation and damage around the placement rooms in the Mark II design was analyzed in a two-dimensional model. The geometry of the model, including different geological layers and the placement room, is shown in Figure 23. The model is in the plane perpendicular to the placement room axis. It includes a single room and extends laterally on both sides of the room to the vertical symmetry planes at the half-distance to the adjacent rooms. The model extends 34 m above and below the repository. The model truncation in the vertical direction was justified because the mechanical effects due to the emplacement room will not extend vertically beyond the distance of 34 m from the rooms. In this model, the bedding planes are explicitly represented as discontinuities at 0.75 m spacing. In the rectangular region, 9.5 m wide and 10 m high, around the center of the room, the rock mass is represented by as an assembly of Voronoi blocks (discussed in Section 3.1.3) as shown in Figure 24. The average size of the Voronoi blocks is 0.1 m.

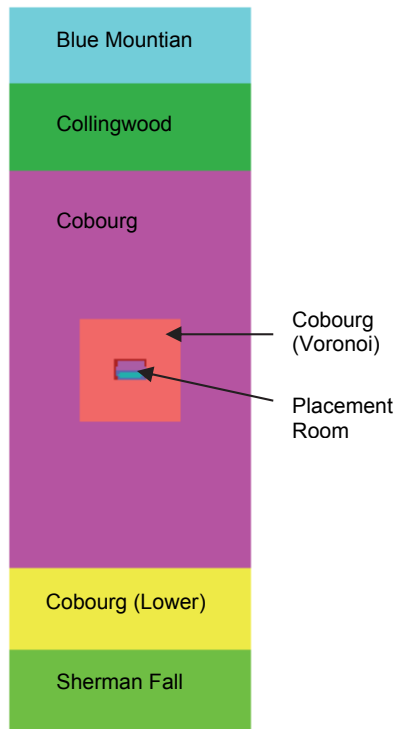


Figure 23: Geometry of the Mechanical Model in Sedimentary Rock

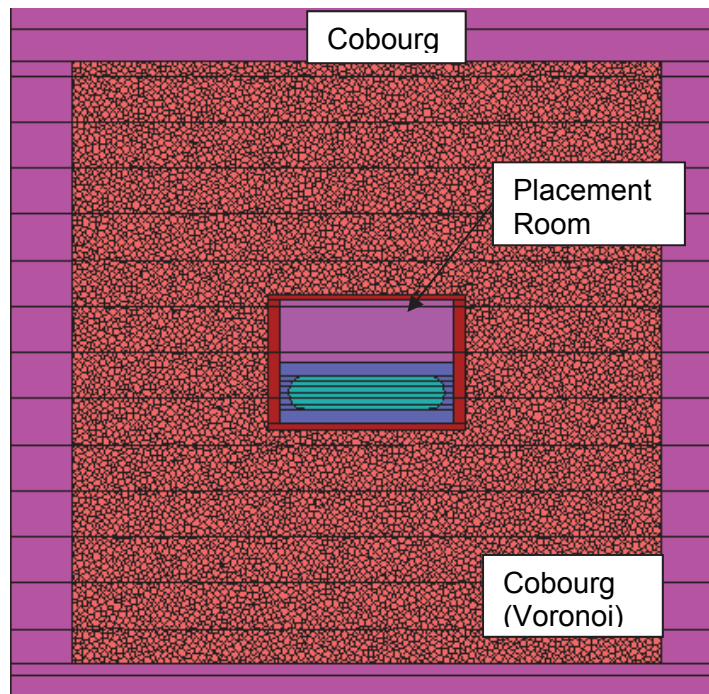


Figure 24: Details of Geometry of the Mechanical Model in Sedimentary Rock

3.4.2.1 Static Model

On the model vertical boundaries, corresponding to the symmetry planes, “roller” boundary conditions were applied. The roller boundary allows displacements in the plane of the boundary but restrains any displacement perpendicular to that plane. The bottom boundary was fixed in both directions. The stress boundary condition applied on the top model boundary considered: 1) the vertical stress equal to the weight of the overburden, and 2) shear stresses to be zero.

3.4.2.2 Dynamic Model

The geometry of the dynamic model is same as the geometry of the static model (shown in Figure 23). The dynamic analysis of seismic shaking was analyzed for two initial equilibrium states. The first was at the time of the maximum temperature at the room wall, 41.2 years after waste placement. The second state was at the time of the maximum vertical glacial load, 150,000 years after waste placement. These two equilibrium states were considered to be the initial conditions for the dynamic analysis that will yield bounding estimates of damage occurring as a result of extreme seismic ground motions. (The main influence of seismic ground shaking is due to stress changes created by propagating elastic waves.) The model used for analysis of stresses, deformation and damage around the repository due to static thermo-mechanical effects was also used for dynamic simulation involving seismic shaking but with modified boundary conditions adequate for dynamic analysis.

The boundary conditions for of the dynamic and static mechanical models are different. The seismic loading is applied at the model base as the vertically incoming stress wave. The velocity histories (shown in Figure 17 through Figure 19) are converted to the normal and shear stress history using the relation between the stresses and velocity for P and S body waves. For the two-dimensional model only one horizontal velocity (or, equivalently, shear stress) history perpendicular to the room axis was applied at the base of the model. It was always velocity history with greater peak ground velocity (PGV). The horizontal velocity history along the room is not expected to affect deformation and damage of the rock mass. Consequently, it was neglected in the analyses (i.e., only two ground motions perpendicular to the room were considered in the analysis). Viscous dashpots were applied on the top and bottom model boundaries. This boundary condition allows seismic waves to pass through the boundary without significant reflections. A free-field boundary condition was applied on two vertical boundaries. This boundary condition represents response of an infinite half-space to vertically propagating waves coupled with viscous dashpots. In this case, the viscous dashpots dissipate only the outgoing waves generated by seismic wave reflected from the placement room. These boundary conditions neglect interaction between the adjacent placement rooms during seismic shaking, a reasonable approximation given the spacing between the placement rooms relative to their cross-sectional dimension.

3.5 MODELLING RESULTS

3.5.1 Temperature Evolution

The locations of the three points within the near-field model for which the temperature histories are provided are shown in Figure 25. The temperature histories at these three points are shown in Figure 26. Figure 26 also shows the temperature history of the far-field model computed at the center of the repository panel (Figure 22). The temperature histories reveal that the near-field model consistently shows greater temperatures than the far-field model. This is attributed to that the repository in the far-field model has a finite size and the heat source in the model is distributed over the surface of the repository panels. Whereas, the near-field model represents a repository of an infinite size. The near-field model provides a good approximation of the temperatures near the repository during relatively short time of a thousand plus years after waste placement. After then, the near-field model overestimates the temperatures as a result of the artifact of numerical modelling. The far field model, however, could provide a good approximation of the repository temperatures for relatively long times after the initial few thousands of years. This phenomenon has been studied by Guo (2007). Reasonable temperature histories can be obtained by modifying the near-field modelling results by subtracting the temperature differences between a finite and an infinite far field models (Guo 2007).

In the thermo-mechanical analysis, temperature histories are created by combining the temperature prediction from the near- and far-field models. Conservatively, the temperatures from the near-field model were used until 50,000 years. The temperatures for the subsequent times used the far-field model predictions. The combined temperature history for Point 1 is shown in Figure 27. A more realistic temperature history of the proposed general configuration of the placement room and backfill were created based on Guo (2007) is also shown in the same plot. Comparison of these two curves confirms that the combined temperature history used in thermo-mechanical analysis is conservative (i.e., always overestimates the temperature). The figure also shows that the long-term temperatures calculated by the near-field analysis were affected by the aforementioned numerical modelling artifacts beyond the first temperature peak.

The temperature at the center of placement room (in close proximity to UFCs) peaks at a temperature of 97°C, ca. 42 years after placement disposition, while the temperature of the surface of the excavated rock peaks at a temperature of 71°C in 1,000 years. The insulating effect of the backfill can be seen slowing the radiation of the heat flux from the UFC.

The temperature contours at some characteristic times as obtained from near and far-field modelling are shown in Figure 28 and Figure 29.

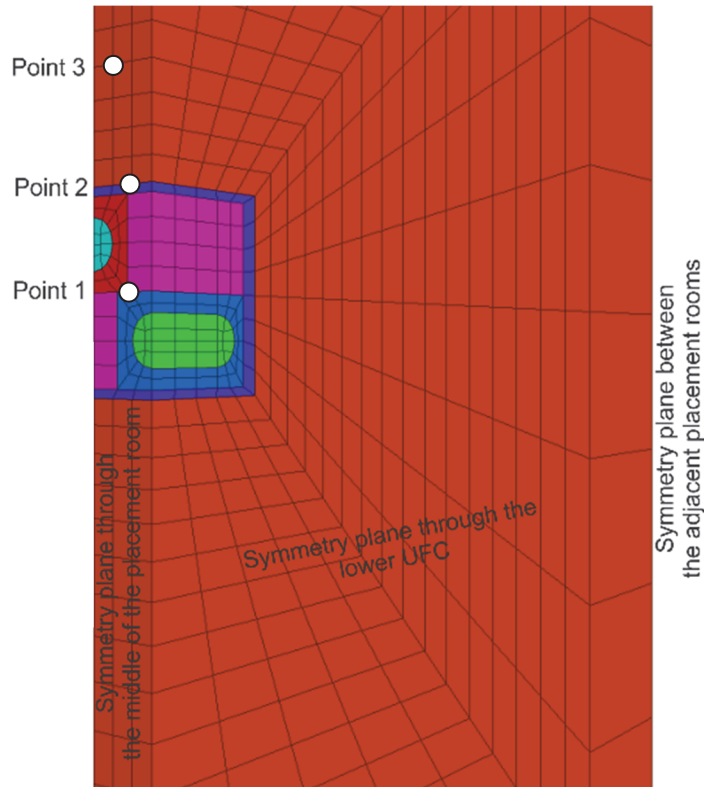


Figure 25: Locations of the Temperature History Points in the Near-field Thermal Model in Sedimentary Rock

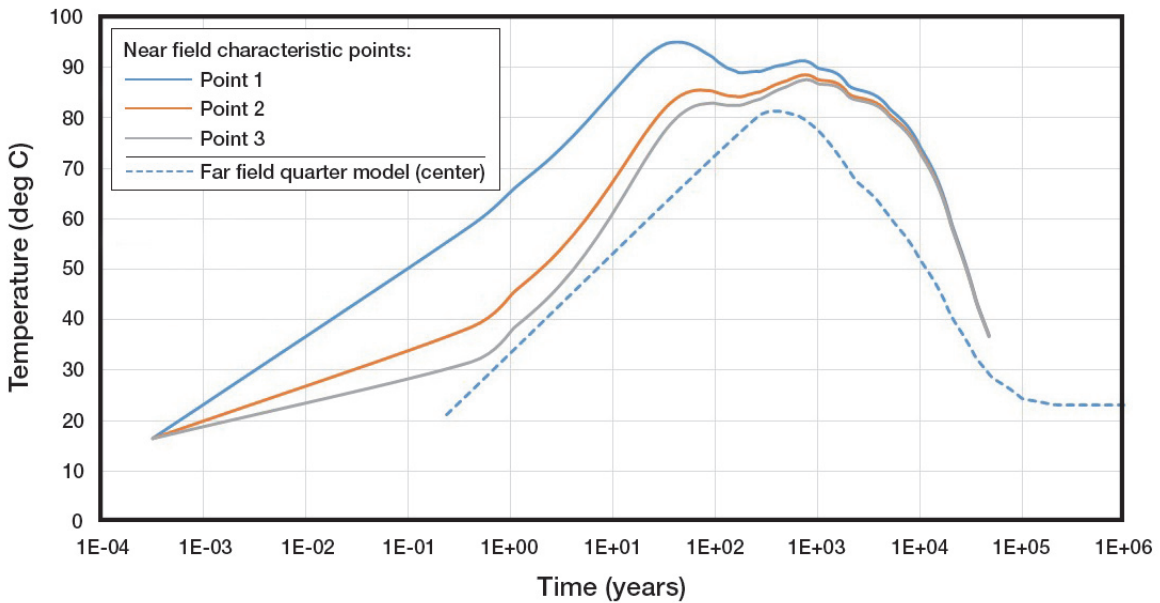


Figure 26: Temperature Histories at Characteristic Points (indicated in Figure 25) as Calculated From the Near- and Far-field Models in Sedimentary Rock

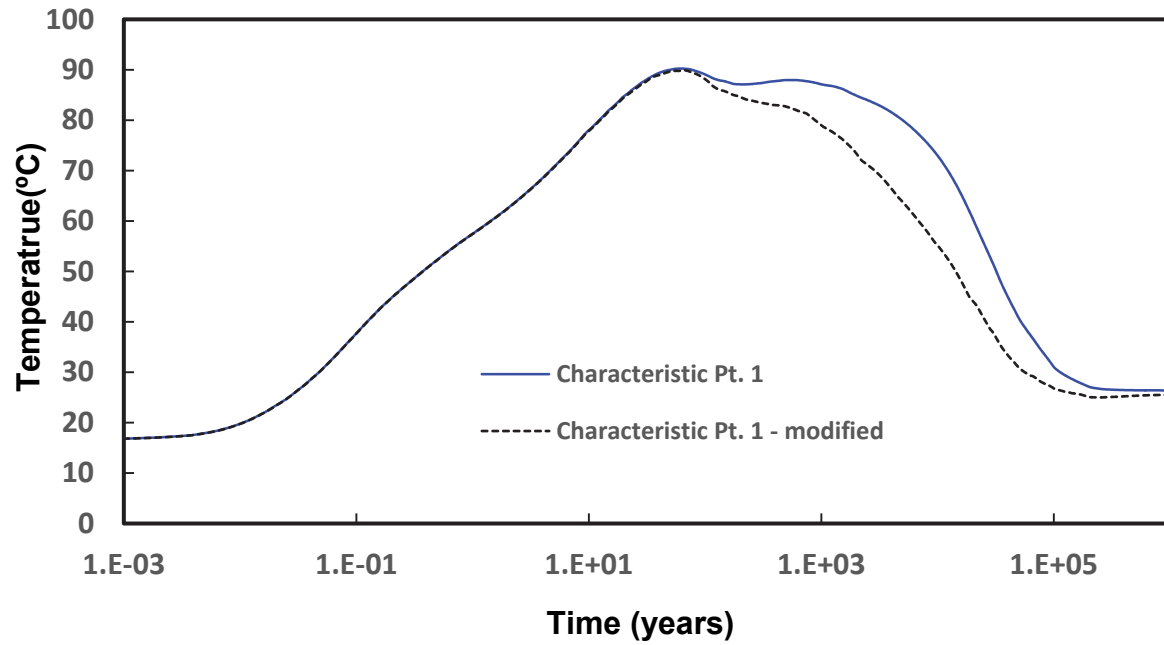


Figure 27: A Comparison Between Modified and Unmodified Combined Temperature Histories at Characteristic Point 1 in Sedimentary Rock

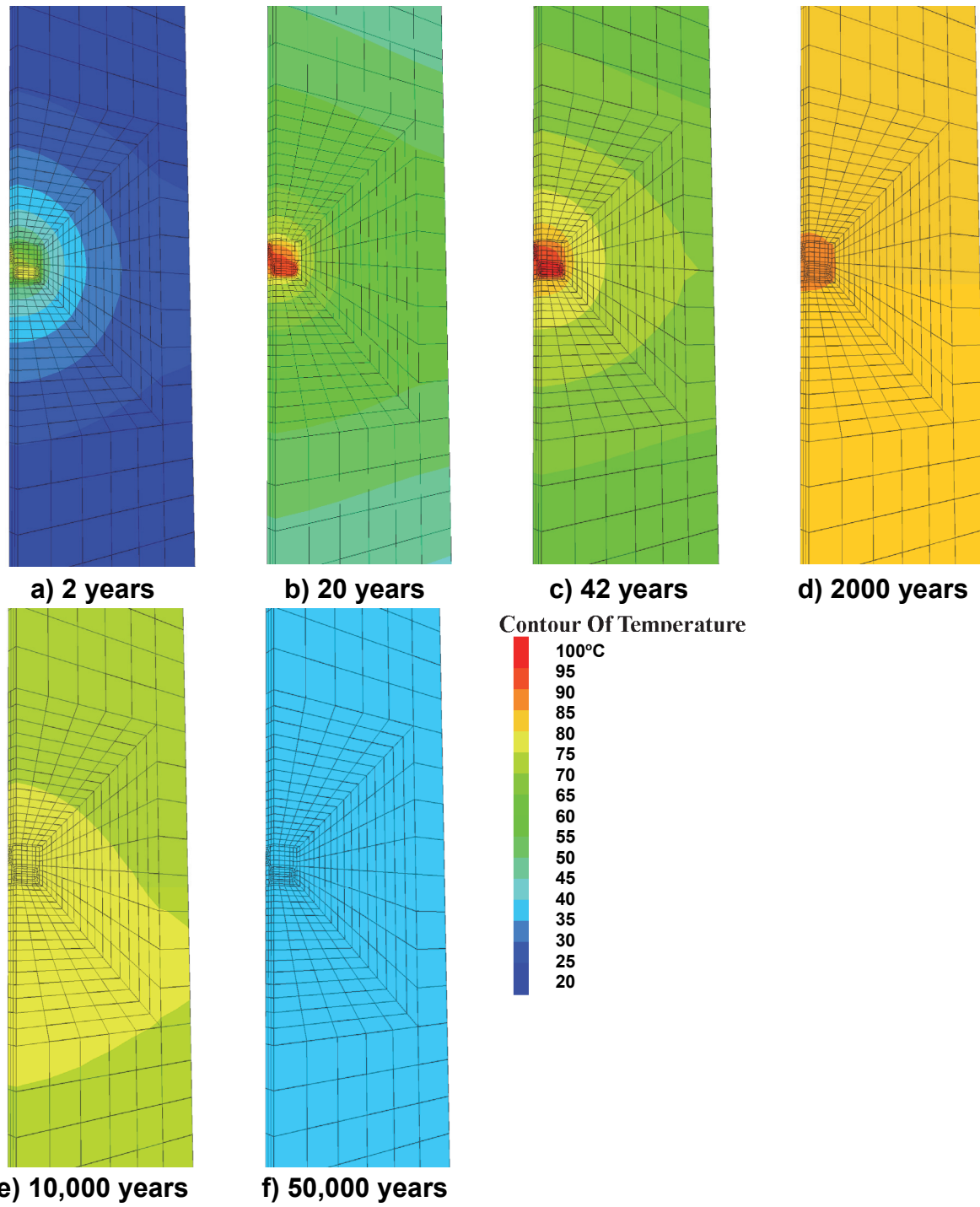


Figure 28: Evolution of Temperature Fields in the Near-field Model in Sedimentary Rock

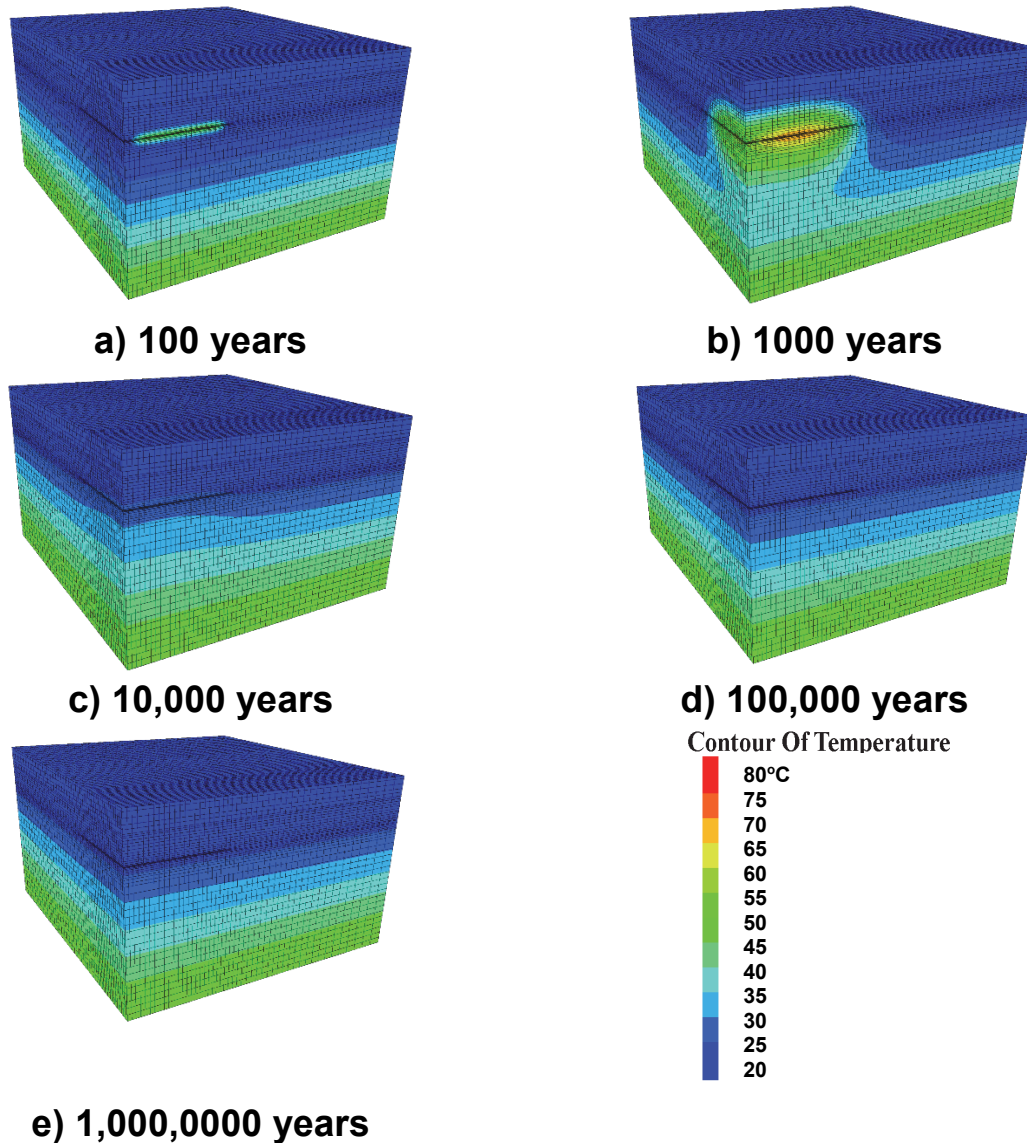


Figure 29: Evolution of Temperature Fields in the Far-field Model in Sedimentary Rock

3.5.2 Time-Dependent Strength Degradation and Thermo-Mechanical Loading

After placement room excavation and emplacement of the UFCs, a maximum rock mass temperature of 97°C is attained at 42 years. As shown in Figure 30b, the predicted rock mass damage (indicated by black and red lines) at the time of maximum temperature is minimal confining mainly to the hypothetical bedding planes adjacent to the room. As time progresses, fracturing of the rock around the room increases. Distributed sporadic micro fractures are present along bedding planes and throughout the vicinity of the room. The density of the micro fractures is greatest in the roof and floor of the room. Rock mass damage stabilizes around the placement room at 2,000 years extending approximately 1 m beyond the excavated surfaces.

Rock mass heating results in predominantly vertically upward expansion with maximum displacements on the level of the repository predicts in this model on the order of 3 cm. This vertical displacement is a consequence of a relatively uniform thermal expansion in the

horizontal plane within the repository footprint under condition of stress free boundary condition at the ground surface. The mechanical model probably underestimates the magnitude of the vertical displacement at the repository level because of relatively close bottom boundary of the model and neglected vertical displacement of the column of the rock below the boundary. The underestimate of the uniform vertical displacement on the repository level does not affect the model predictions of placement room stability or rock damage because the neglected uniform vertical displacement does not result in stress change (only vertical model translation). The vertical displacement of the ground surface above the repository will exceed the vertical displacement on the repository level. This mechanical model does not predict the displacement of the ground surface. This expansion is relatively uniform across the entire repository such that differential displacements do not result in the formation or reactivation of fractures in rock mass and, thus, do not influence the integrity of placement rooms.

Discontinuous micro cracking is evident along the horizontal bedding planes extending to 2 m from the placement room. Peak rock mass strength is not attained at these locations indicating that the damage does not represent open fractures. The EDZ (indicated by red cracks in the figure) is contained within 1 m distance from the room walls (mainly floor and roof).

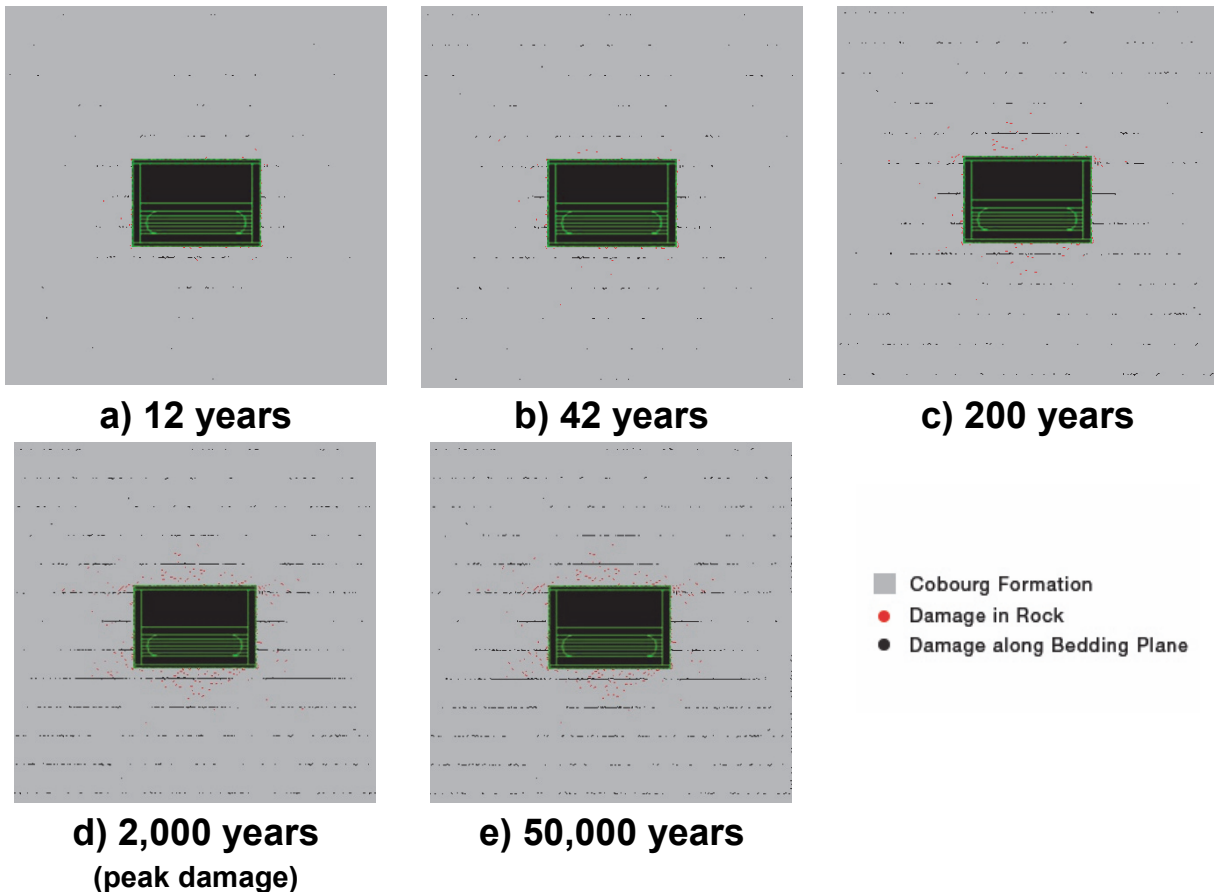


Figure 30: Repository Damage Evolution to 50 ka in Sedimentary Rock

3.5.3 Glacial Loading

The analysis considers in situ and rebound stresses, the effect of time-dependent strength degradation and a single cycle of glaciation. This glaciation occurs during the period between 60,000 to 174,000 years with a maximum ice thickness of 2.8 km at 150,000 year. Glacial loading does not significantly affect the damage around the placement room, as shown in Figure 31a and Figure 31b. This lack of damage development is attributed to confinement provided by the backfill in the placement room. The predicted EDZ, approximately extending 1 m into the roof and floor, is similar to that at initiation of the glacial cycle (50,000 years). The increase in vertical ice-sheet loading creates vertical downward movement that is nearly uniform across the repository. The maximum predicted relative displacements within the rock mass are less than 5 mm, which will not induce any fracture formation or reactivation within the rock mass around the placement room. Discontinuous micro cracking is evident along the horizontal bedding planes above and below the placement room. Peak rock mass strength is not reached at these locations indicating that induced damage does not represent open fractures.

At the state of the maximum glacial load, the average pillar stress is 18.7 MPa. Even for the maximum vertical loading during glacial cycle, there is 10-m wide elastic pillar between adjacent placement rooms.

Glacial loading does not significantly affect the damage around the room, as shown in Figure 31. This is attributed to the confinement provided by the backfill in the placement room. Thus, analysis with multiple glaciation episodes was not warranted.

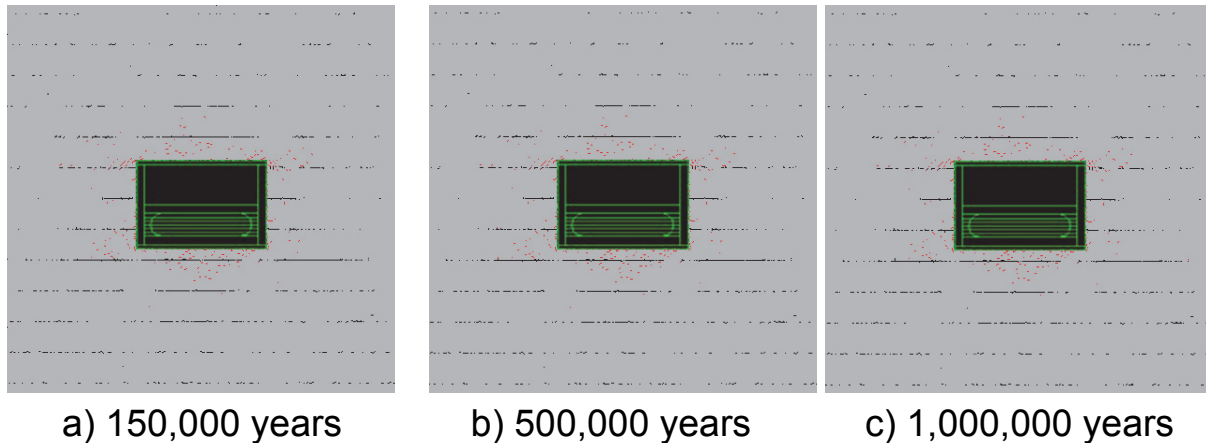


Figure 31: Microcracks in the Rock During Glaciation Period and Beyond, to 1Ma in Sedimentary Rock

3.5.4 Gas Pressure

The model at state corresponding to 29,000 years postclosure, is subjected to peak gas pressure of 8.3 MPa in the interior of the room. The resulting damage is shown in Figure 32. Figure on the left, shows damage before gas loading was applied, and figure on the right, shows damage developed after gas loading was applied. The effect of gas pressure on the room walls is minor. The increased gas pressure inside the room does not result in tension in the wall and initiation and propagation of a gas-driven fracture. Thus, there is no change in EDZ geometry, which extends approximately 1 m into the rock mass, primarily in the roof and floor.

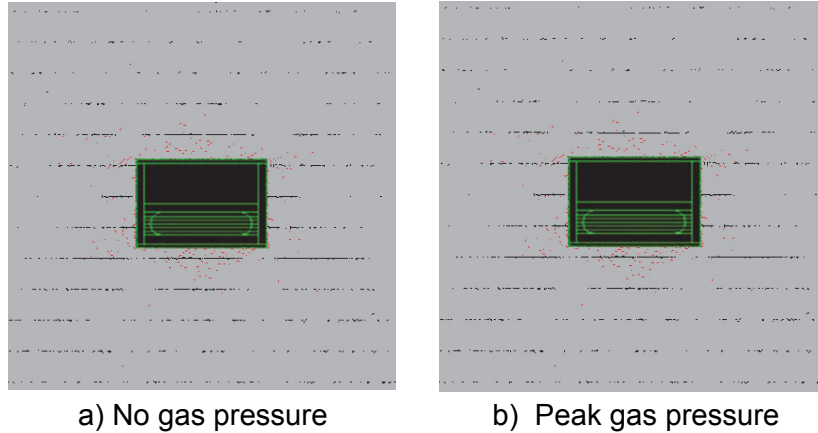


Figure 32: Effect of Gas loading on Damage in Sedimentary Rock

3.5.5 Seismic Loading

Three plots in Figure 33b through Figure 33d show the damage predicted by the model if the three ground motions at 10^{-6} p.a. probability level (PGA of 0.60g) are assumed to occur at the state when the peak temperature is reached. Some additional fracturing develops (compared to the initial state shown in Figure 33a). However, the general extent and intensity of the damage does not change significantly due to the confinement provided by the backfill. Thus, there is no change in EDZ which remains about 0.1 m thick.

Similarly, for the models of seismic loading occurring at the peak glacial loading, the damage due to dynamic shaking is shown in Figure 34. This is the state that initially has more damage than the peak temperature state. Even for this state the considered seismic loading (10^{-6} p.a. probability level, PGA of 0.60g) does not cause appreciable increase in damage. Thus, there is no change in EDZ which is about 1 m prior to and after the earthquake events.

Considering that the ground motions at 10^{-6} p.a. probability level did not result in significant increase in extent or intensity of the damage around the placement room, the effect of seismic ground motions at 10^{-5} p.a. probability level on deformation and damage of the rooms and other seismic related load combinations were not simulated. These ground motions under these scenarios would result in even less damage.

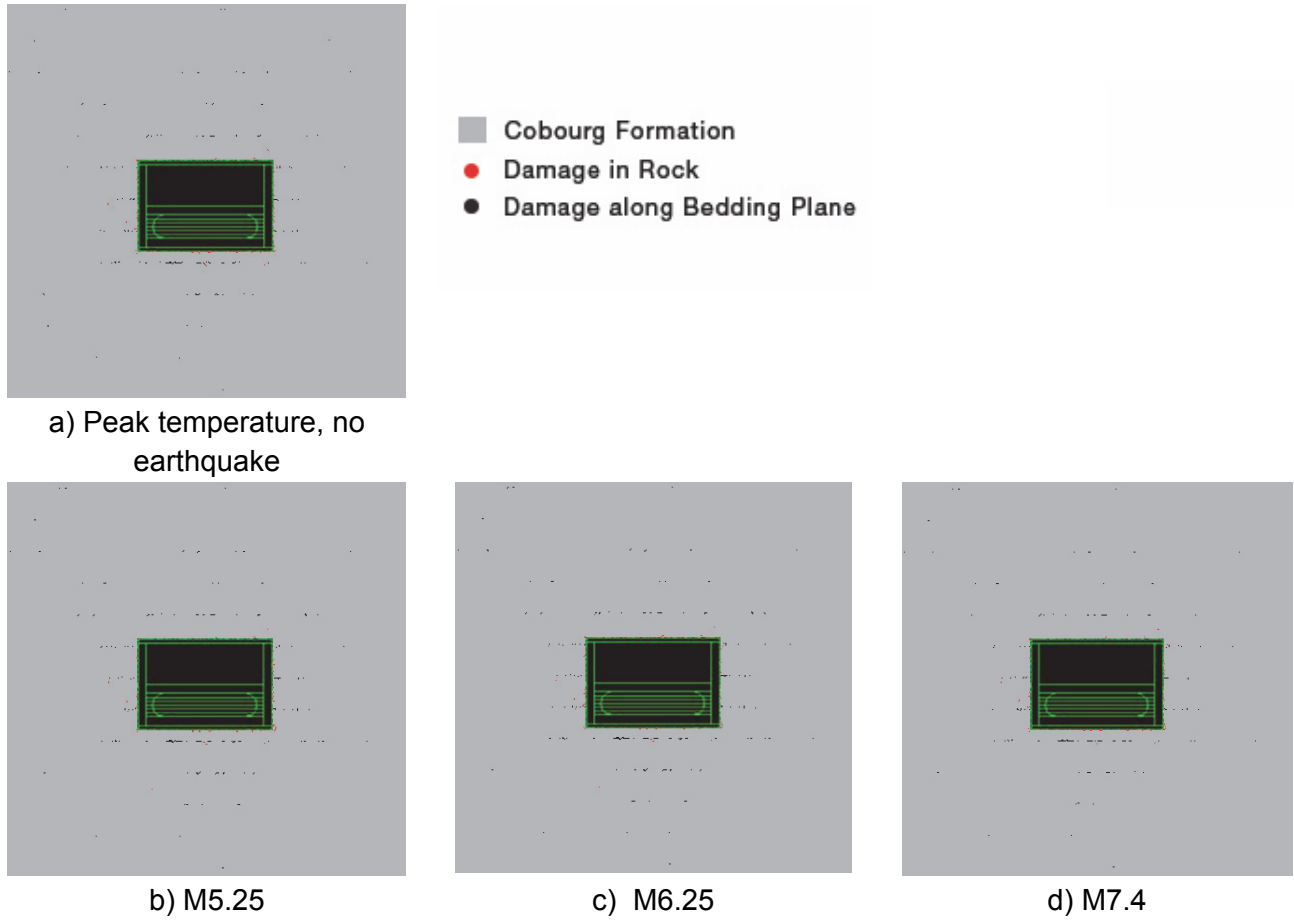


Figure 33: Microcracks in the Rock at Peak Temperature Subjected to Three Different Earthquakes at 10^{-6} Probability Level in Sedimentary Rock

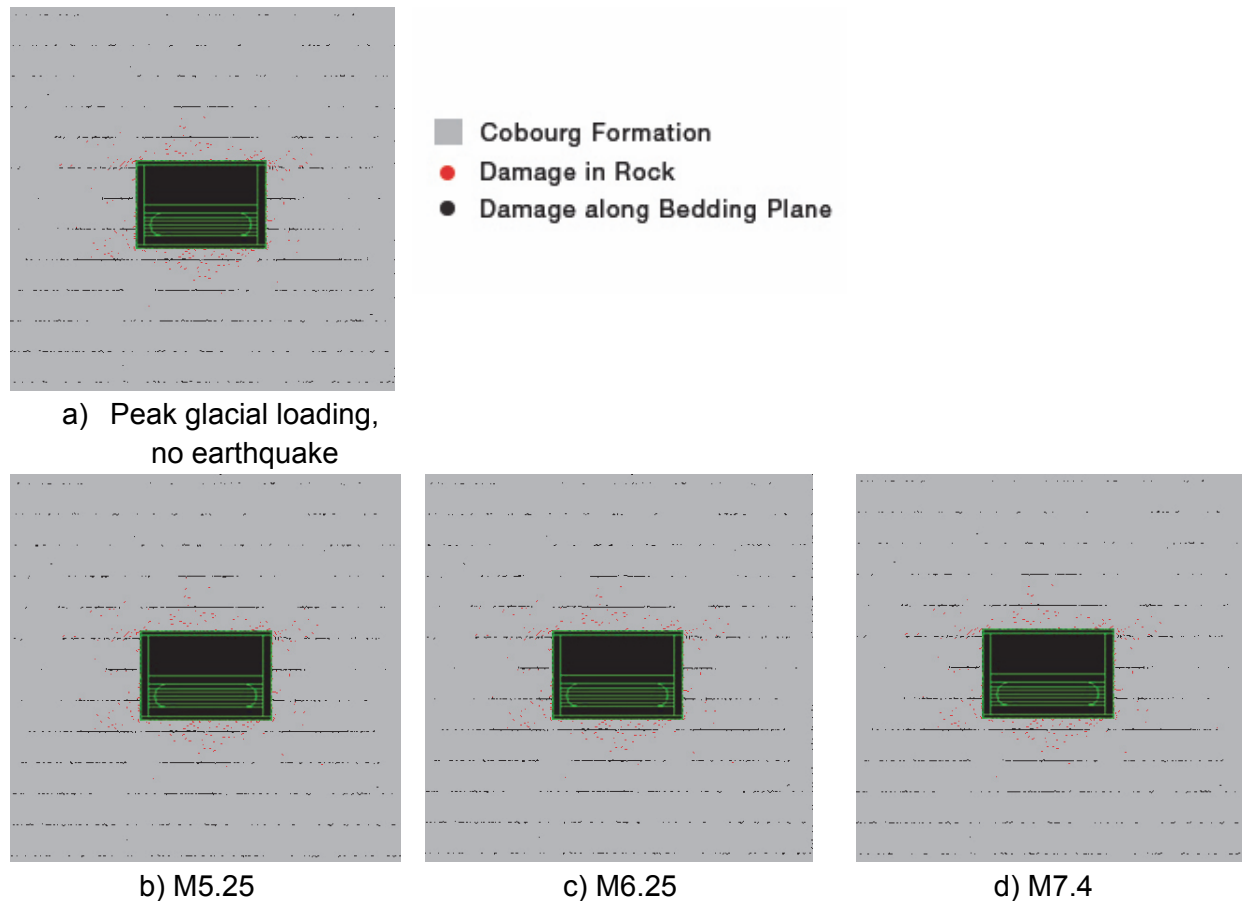


Figure 34: Microcracks in the Rock at Peak Glacial Load Subjected to Three Different Earthquakes at 10^{-6} Probability level in Sedimentary Rock

3.5.6 Loading on the UFC

As part of the case study, the transient loading on a UFC during external and internal repository perturbations was evaluated at key critical periods throughout the 140ka simulation timeframe. The loads estimated include those due to effective stress and porewater pressure. A time series plot that illustrates the predicted transient loads between 50,000 and 190,000 years, assuming two limiting conditions of porewater dissipation, is shown in Figure 35.

Post excavation rock stress around a placement room has a negligible effect on the UFC loading. The placement rooms are stable after excavation and no rock stress will be transferred to the UFC after placement other than the weight of the bentonite backfill itself. Over time and before the onset of glacial loading, the load on the UFC will gradual increase due to: 1) placement room resaturation; and 2) total stress increase due to thermally-induced stress changes. Upon resaturation, the maximum fluid pressure exerted equals to the hydrostatic pressure of 5 MPa in the fresh water case. Whereas the increase in the total stress due to thermally-induced stress are estimated by thermo-mechanical models as described in Section 3.4.1. Within the enclosing rock mass this thermally-induced stress increase combined with hydrostatic porewater pressure reaches a maximum of 6.7 MPa at about 1,000 years, much less than the vertical lithostatic stress of 13 MPa. Subsequently, UFC loading decreases to values below 6 MPa prior to glaciation and the occurrence of ice-sheet advance and retreat

above the repository. It is during this latter period of time that maximum loading of the UFC occurs.

The maximum UFC loading during glaciation is estimated to be approximately 16.0 MPa assuming undrained conditions (“without fluid migration” in Figure 35). This is due, in part, to “stress arching” created when the lower modulus backfill carries less load than the stiffer enclosing rock mass (e.g., pillars between the placement rooms). If this backfill total stress load is less than the pore water pressure in the rock mass there will be pore water migration toward the emplacement room leading to an increase in the backfill pore water pressure. The exerted UFC pressure is the sum of the initial hydrostatic groundwater pressure (5MPa), and the change in porewater pressure created by mechanical ice-sheet loading and resultant total stress change in the far-field. In the current case study, a conservative Skempton’s coefficient of 0.7 was used to estimate the excess pore pressure generated under maximum glacial loading. Under this condition, a conservative upper bound pressure on UFC could be as high as 20.8 MPa (“fluid migration” in Figure 35). This estimated value is considered cautious as it represents a very conservative assumption in that the porewater pressure in the enclosing rock mass could equilibrate with that inside the placement rooms. With this assumption in mind the maximum conservative loading on a UFC is estimated to be 22.7 MPa, including the contribution from bentonite swelling (assuming a swelling pressure of 1.9; Baumgartner 2005).

After glaciation, the pressures on the UFC could reduce to 6.0 MPa (excluding swelling pressure) and largely remain constant until the next glacial episodes (only one glacial episode is considered in the present study).

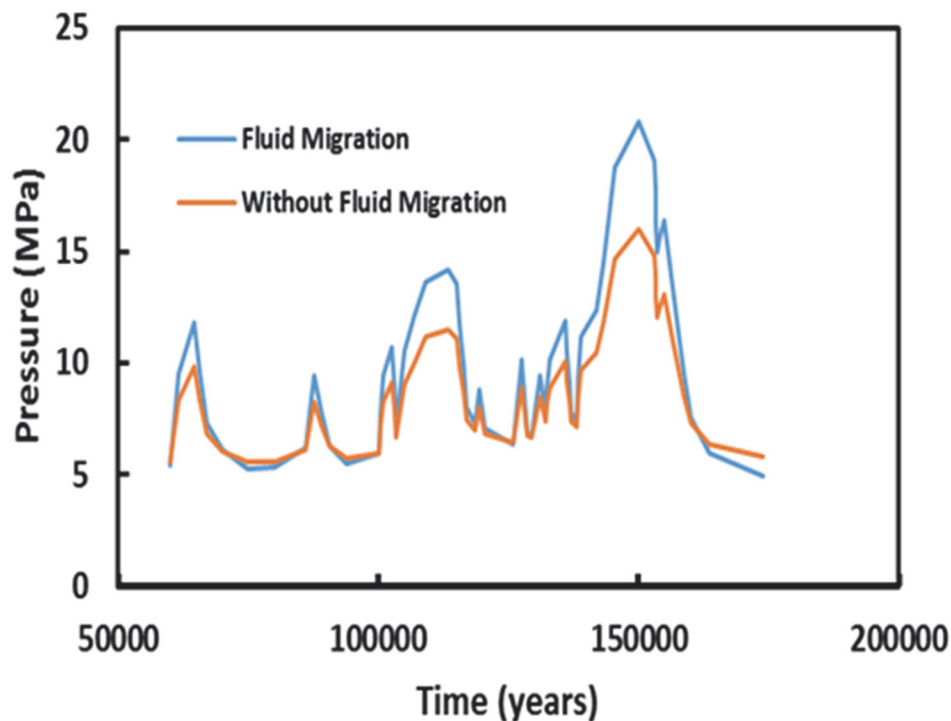


Figure 35: Evolution of Pressure on the UFC in Sedimentary Rock

3.6 SUMMARY AND DISCUSSION

The analyses considered a series of bounding simulations designed to gain insight into the response and degree of damage in the near- and far-field associated with the expected evolution of the repository to 1Ma. The simulations also provided a reasoned basis to estimate UFC loading. Each of the simulations considered a base-case scenario that included in-situ stresses, time-dependent strength degradation of rock mass, pore pressure in the rock mass, UFC thermal output and multiple glacial ice sheet advances and retreats (maximum thickness ca. 3km). Repository perturbations superimposed on the base cases were:

1. A low probability (rare) earthquake of 10^{-6} p.a. (0.5g);
2. Internal repository gas generation (8.3 MPa); and
3. Extreme combinations of the loads and perturbations above.

The simulations illustrate that induced rock mass damage is contained within meters of the placement rooms. The EDZ as defined in Fracture System (2011) is predicted to be approximately 1 m deep in the roof and floor of the placement rooms. If bedding planes exist, slipping and micro-cracking is predicted not to extend beyond 2 m from the rooms. The deformation of bedding planes does not include tensile damage or opening. Bedding plane failure in shear will not result in significant dilation or fracture opening. Predicted relative rock mass displacements are minor (i.e., 5 to 10 mm) and placement room instability did not occur under any loading scenario. The maximum placement room convergence is predicted to be less than 5 mm under maximum glacial ice-sheet loading. The creation of a HDZ appears to be prevented as a result of confinement provided by the engineered backfill materials.

The thermally-induced stresses occurring within the first thousand years are the main loading condition affecting the extent and intensity of rock mass damage. Other phenomena including long-term rock mass strength degradation, cyclic glacial loading and strong seismic ground motions have less influence on predicted damage and stability, again the apparent result of support provided by the engineered backfill.

For the glacial loading scenario, an effective stress formulation including undrained pore pressure changes was assumed. The pore pressure increase leads to the weakening of the rock mass strength and the effective stress calculation for low porosity rocks results in possible overestimation of the damage extent. If a fully coupled hydro-mechanical simulation is considered, more refined consideration of the magnitude of the pore pressure and its effect on the strength of low porosity rocks would lead to further reduction in rock damage. It is noteworthy that under the combined case of repeated seismic and glacial loads, the model predicts that a 10-m-wide core of the pillar between placement rooms remains elastic (undamaged) and load bearing.

The near-field model consistently yields higher temperatures than the far-field model. This is attributed principally to model geometry in which the thermal source in the far-field model is distributed over the entire repository surface area, as opposed to the near-field model that assumes symmetric boundaries. The near-field model yields good approximations of the repository temperature state to approximately 2,000 years. Subsequent to this the near field model, as a result of assumed boundary conditions, overestimates the temperatures. In this event temperature time histories for 1 Ma were constructed by combining predicted temperature histories from the near- and far-field models. The temperatures from the near-field model were conservatively used until 50,000 years, including an artificial second peak temperature. This

second peak is a model artifact. Beyond 50,000 years, temperature histories determined with the far-field model are applied.

Temperature increases occurring as a result of UFC heat fluxes cause the rock mass to expand vertically upward. The maximum displacement at the repository level is estimated to be approximately 30 mm. This movement is relatively uniform across the entire repository, with small differential displacements that would not induce placement room damage. Similarly, an increase in glacial ice-sheet load leads to vertical downward movement that is uniform across the entire repository. The maximum relative displacement or convergence of placement room is predicted to be less than 5 mm at the time of maximum glacial load.

Predictions of placement room stability, damage in the surrounding rock mass, and integrity of the enclosing rock mass involve uncertainty. Those uncertainties are caused by: i) material properties and behaviour (e.g., strength degradation and long-term strength); and ii) loading conditions imposed by natural and repository-induced perturbations. Uncertainty is also associated with the random nature of the processes considered; and ii) lack of knowledge and/or insufficient testing. In this study, the model uncertainties are addressed by conducting bounding analyses. Wherever uncertainty exists, the reasonable bounding properties or conditions were assumed. For example, the long-term strength of the Cobourg limestone was assumed to be equal to 40% UCS or the assumed crack initiation stress. It is not reasonable to expect that the long-term strength of rock would be less than the crack initiation stress. On the other hand, the extreme, low probability ground motions were assumed to occur coincidentally with most unfavourable stress conditions in the rock mass, for example, when the peak rock temperature is achieved. Consequently, this study yields reasoned bounding predictions of placement room performance at 1Ma.

4. LONG-TERM STABILITY ANALYSIS OF A MARK II REPOSITORY IN CRYSTALLINE ROCK

4.1 THERMAL AND MECHANICAL MATERIAL PARAMETERS

4.1.1 Geological Profile

The crystalline setting is assumed to be moderately to sparsely fractured granite, homogeneous and isotropic on large scale (NWMO 2014 and 2015). The homogeneous lithology is assumed for the entire geological profile from the ground surface to depth of 2,000 m, which was assumed to be the bottom of the thermo-mechanical models.

4.1.2 Material Models and Parameters

The assumed intact rock and rock mass properties are listed in Table 13. Using those data the Hoek-Brown failure envelope is generated as shown in Figure 36. In the same figure the fitted Mohr-Coulomb failure envelope is also shown. The fitting is conducted for the stresses for a tunnel at 500 m depth. Some key strength parameters, including UCS, cohesion and friction angle, and Young's modulus of rock mass are listed in Table 14. The Young's modulus of the rock mass, E_{rm} , was calculated using the following relation by Hoek and Diederichs (2006):

$$E_{rm} = E_i \left[0.02 + \frac{1-D/2}{1+e^{(60+15D-GSI)/11}} \right] \quad (11)$$

where the damage factor (D) was assumed to be zero; the Geological Strength Index (GSI) taken to be 79 (Golder Associates 2012); and Young's modulus of the intact rock, E_i , taken from Table 13.

Table 13: Intact Rock and Hoek-Brown Rock Mass Properties

Property	Value
Intact Unconfined Strength, UCS	210 MPa
Intact Rock Young's Modulus, E_i	45 GPa
Hoek-Brown Parameter, m	12.5
Hoek-Brown Parameter, s	0.1
Hoek-Brown Parameter, a	0.3

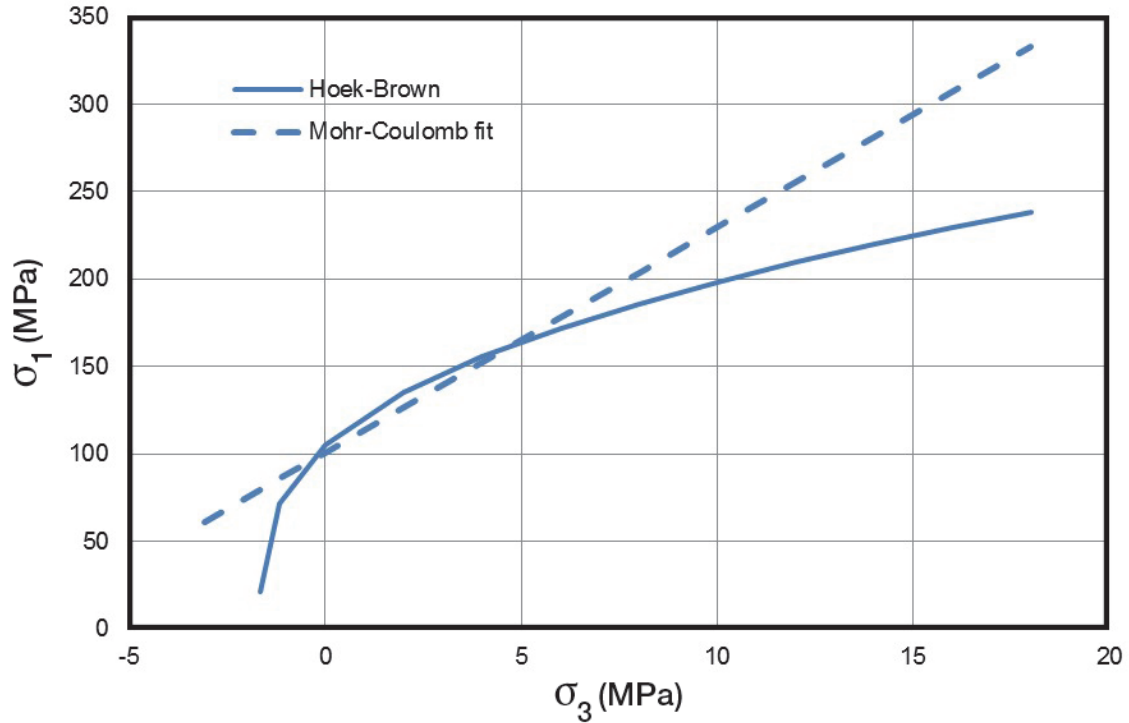


Figure 36: Crystalline Rock Failure Criteria: Non-Linear Hoek-Brown and Fitted Mohr-Coulomb

Table 14 Mechanical Model Parameters of Granite Rock Mass

Property	Value
Rock Mass Peak UCS	105 MPa
Cohesion	14 MPa
Friction Angle	59°
Tensile Strength	1.7 MPa
Young's Modulus, E_{rm}	39.1 GPa

The thermal properties of granite rock mass as used in the numerical simulations (Garisto et. al., 2004) are listed in Table 15. Homogeneous thermal properties were assumed in all models.

Table 15: Thermal Properties of Granite Rock Mass

Property	Value
Density	2700 kg/m ³
Thermal Conductivity	3.00 Wm/°C
Specific Heat	2.28 MJ/m ³ °C
Linear Coefficient of Thermal Expansion	10 ⁻⁵ 1/°C

4.1.3 Voronoi Block Approximation

Similar to the modelling in sedimentary rock setting, the Voronoi tessellation scheme (Figure 7) was used to represent deformation and damage of the crystalline rock around the placement room. A calibration process was carried out to adjust the micro-mechanical properties (Figure 7) until the macro-mechanical measured behaviour is matched to the test results. The Voronoi tessellation approach is described in detail in Section 3.1.2.

The model is discretized into Voronoi blocks in the region around the placement room where stress concentrations from the in situ stresses and external loading occur. The average Voronoi block size (width) is selected to be 0.1 m. The ratio of the block size to the minimum room dimension (height), which is $0.1/2.2 = 0.045 \ll 1$, is sufficiently small so that the block size does not affect the model results.

4.1.4 Voronoi Model Calibration

The Voronoi block model is calibrated to the mechanical properties of the granite. The calibration is conducted by simulating the laboratory experiments used to determine the laboratory properties of the rocks. The most important mechanical parameters that control stability of the underground excavation are UCS and Young's modulus (stiffness). The micro-mechanical parameters of the Voronoi block model are adjusted in order to match the stiffness and strength of the rock mass properties of the granite (Table 14).

The micro-mechanical parameters that need to be determined in the calibration process in described in Section 3.1.4.

The model parameters also include residual cohesion and tensile strength of the contacts. In all of the analyses discussed here, residual cohesion and tensile strength were considered to be zero in order to simulate the granite as a brittle material.

Matching of Young's modulus and Poisson's ratio and the macro-failure strength envelope defined by cohesion, friction angle and tensile strength, is an under-determined problem, because there are more micro-mechanical constants than constraints. The problem is resolved by assuming that the stiffness of the Voronoi blocks is much greater (~10 times) than the stiffness of the contacts, meaning that the contacts are the main contributors to the compliance of the model. The other extreme also is analyzed, when the contacts are much stiffer than the blocks. The results of the two approximations are found to be quite similar (BSC 2004). In the case of the calibration of micro-mechanical strength parameters, additional constraints used to bound the solution were mode of failure and its evolution as a function of confinement, and post-peak behaviour (e.g., post-peak softening strain and residual strength). It is expected that the

massive, good quality granite with relatively high strength and stiffness will also exhibit brittle behaviour and softening post-peak response. Therefore, the micro-mechanical strength parameters used in the Voronoi block model were adjusted to result in a brittle sample failure.

The calibration was carried out on 5 Voronoi block samples generated using different realizations of random block geometry. The results of the numerical simulation of unconfined compression and direct tension are shown in Figure 37. The tests were carried out on 2.5 m edge square samples. The samples fail by axial splitting in the unconfined compression test.

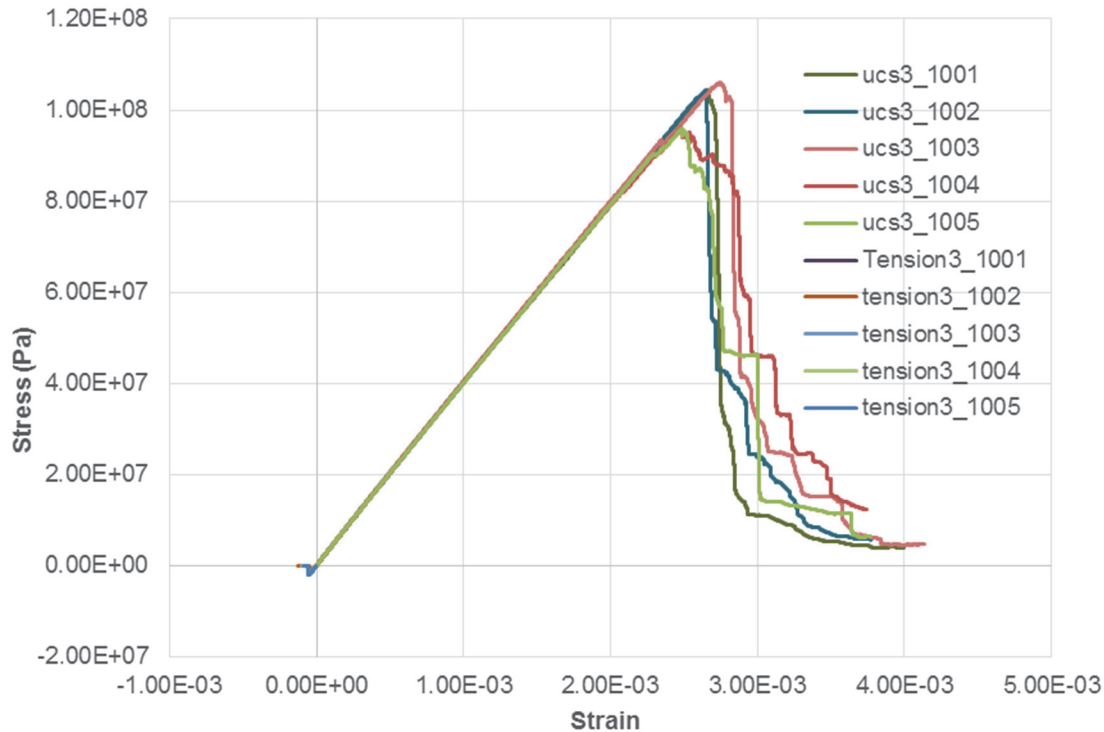


Figure 37: Axial Response Obtained from the Numerical Tests on Calibrated Voronoi Block Model of Granite (Compression Positive)

The stiffness and strength parameters that represent the properties of the Voronoi block samples under unconfined conditions are summarized in Table 16. The Young's modulus of 38.9 GPa and the UCS of 101 MPa, which are averages calculated from the results for 5 Voronoi block samples, are in good agreement with the target values of 39.1 GPa and 105 MPa respectively, for the granite rock mass listed in Table 14. The error in the tensile strength is somewhat larger, 2.1 MPa compared to estimated 1.7 MPa, an overestimation of 19%. However, these minor changes in the tensile strength do not have a significant effect on the compressive strength or stiffness.

Table 16: Summary of Voronoi Stiffness and Strength Parameters from Unconfined Tests

Seed	UCS (MPa)	Tensile Strength (MPa)	E (GPa)
1001	105.0	2.1	39.2
1002	104.0	1.95	39.3
1003	106.0	2.0	39.0
1004	95.0	2.1	40.0
1005	95.4	2.1	37.0
UDEC average	101.0	2.1	38.9
DATA	105.0	1.7	39.1
error	-4.0%	-19%	-0.5%

The Voronoi samples were tested also for compressive loading for two different values of confining stress (15 MPa and 30 MPa). Increase in confinement results in a strength increase. The post-peak behaviour observed in the numerical tests for three compression tests is also quite different. Unconfined response is brittle (Figure 37). The response of the synthetic material under confined conditions, for 15 MPa and 30 MPa confining pressures, is illustrated by the stress–strain curves shown in Figure 38. The material still exhibits softening behaviour but less brittle (i.e., increased residual strength and increased critical softening strain) than for unconfined conditions. Such a response is qualitatively typical for rocks.

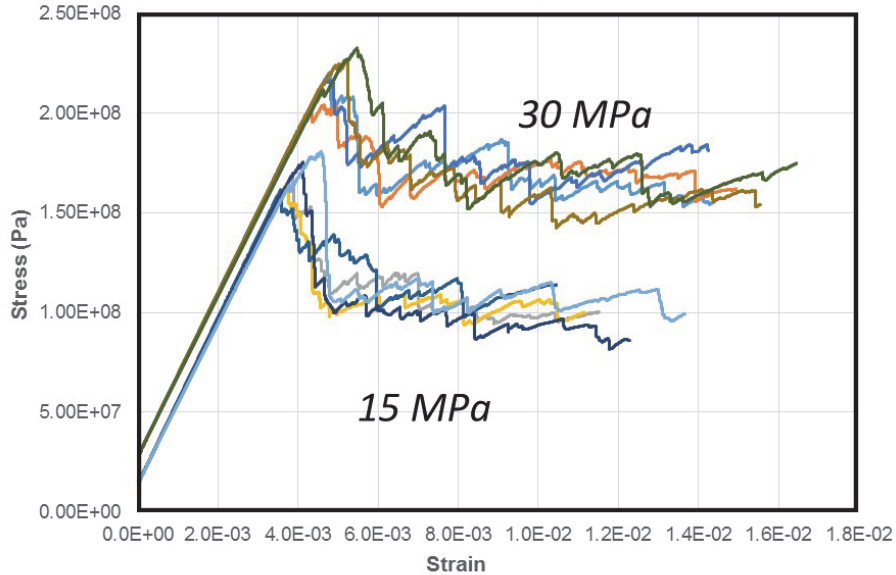


Figure 38: Confined Response (for 15 MPa and 30 MPa Confinement) Obtained from the Numerical Tests on Calibrated Voronoi Block Model of Granite (Compression Positive)

To ensure that the numerical model approximates the strength of the rock mass, it is necessary that the model has: 1) equal or lower yield strength, 2) equal or more brittle post-peak response and 3) equal or lower residual strength, compared to the estimated rock mass strength based on traditional rock engineering approaches. The post-peak response of the granite from numerical simulations during calibration for 5 realizations of Voronoi block geometry is almost perfectly brittle, with the residual strength less than or equal to 15% of the peak strength. The post-peak behaviour of synthetic Voronoi block model is a reasonably conservative approximation of the mechanical behaviour of the granite.

The model response (including the calibration tests) will not be identical between different realizations of the block geometry (as illustrated in Figure 37 and Table 16), because the geometry of the Voronoi blocks is random. Although there is variability between different block geometry realizations in the model response, it is important that variability is relatively small, within 10% of the mean. The variability for 5 samples used in the calibration is less than 5%, which is much less than the variability of the typical laboratory test results.

The calibrated micro-mechanical properties for the granite are listed in Table 17. Those properties were assumed to be uniform throughout the model (or the sample). The effect of spatially variable properties (i.e., normally distributed joint peak cohesion and tension with a standard deviation between 10% and 30% of the mean) on the mechanical behaviour of the Voronoi block model, which also was investigated, was not significant, therefore it was not considered necessary to introduce that as an additional complexity into this modelling.

Table 17: Calibrated Micro-mechanical Properties for the Voronoi Blocks and Contacts

Unit	Granite
Contact Normal Stiffness k_n	573 GPa/m
Contact Shear Stiffness k_s	287 GPa/m
Block Bulk Modulus K	326 GPa
Block Shear Modulus G	245 GPa
Block Young's Modulus E	588 GPa
Block Poisson's Ratio ν	0.2
Contact Peak Cohesion c	56.5 MPa
Contact Peak Friction ϕ_p	35°
Contact Peak Tensile Strength T	3.63 MPa
Contact Residual Friction ϕ_r	15°

Notes: Residual micro-tension and cohesion are assumed to be zero.

4.1.5 Long-Term Strength

Extensive static fatigue test results exist for Lac du Bonnet granite (Figure 12a). Those data were used as basis for time-dependent strength degradation of the granite for the repository in the crystalline setting. However, these data and curves do not include any information regarding the lower bound strength defined as the stress at which the damage initiates. Many experts in the field believe that the lower bound value of the long-term strength of the rock is equal to or greater than crack initiation (CI) stress in unconfined compressive tests (Damjanac and Fairhurst 2010). Nickiar and Martin (2013) examined 376 laboratory tests. The average ratio of crack initiation to peak stress in igneous, sedimentary and metamorphic rocks, regardless of the mineralogy and grain size, was found to range from 0.42 to 0.47 in unconfined compression. In triaxial compression, the crack initiation stress ratio ranges from 0.50 to 0.54. Hence assuming a CI equivalent to long-term strength of crystalline rock represents a lower bound value.

4.1.6 Discrete Fracture Network (DFN)

The DGR repository in the crystalline setting will be located in moderately to sparsely fractured granite. Most of the analysis assumes that the mechanical behaviour of such a rock mass can be approximated using the equivalent rock mass approach and scaled properties documented in Section 4.1.2. In order to investigate the effect of discrete fractures and to prove validity of the equivalent rock mass approach some simulations were conducted by explicitly represented pre-existing joints. Jointing of the rock mass is characterized statistically and different realizations of discrete fracture network (DFN) are generated as input for the three-dimensional model.

No jointing data have been developed specifically for the potential repository in the crystalline setting. Therefore, for this study it was decided to use statistical characterization of jointing at of developed based on mapping at and for Forsmark (Fox et al. 2007), the designated site of the

Swedish final repository for radioactive operational waste in a moderately to sparsely fractured crystalline rock mass. This site is managed by SKB, Swedish Nuclear Fuel and Waste Management Company.

4.1.6.1 DFN Geometrical Parameters

DFN parameters are derived from Fox et al. (2007). The reference model is called, in the SKB nomenclature, Tectonic Continuum Model (TCM). Only the fracture model named FFM01 is reproduced. In this DFN, we generate the four global fracture sets named NE, NS, NW and SH. The corresponding parameters are described in Tables 7-1 and 7-2 of the report by Fox et al. (2007), reproduced (partially) here in Tables 18 and 19.

Table 18: Fracture Orientation Model

Fracture domain	Fracture set	Set type	Probability distribution	Mean pole			Fisher Distribution κ		
				Trend	Plunge	κ_{mp}^*	Mean	Std. Dev.	Median
FFM01	NE	Global	Univariate Fisher	314.9	1.3	47.4	20.9	9.4	17.8
FFM01	NS	Global	Univariate Fisher	270.1	5.3	47.0	21.3	13.2	20.3
FFM01	NW	Global	Univariate Fisher	230.1	4.6	32.3	15.7	8.1	12.6
FFM01	SH	Global	Univariate Fisher	0.8	87.3	48.9	17.4	7.1	14.4

Table 19: Fracture Sizes Model at Forsmark

Fracture domain	Fracture set	Set type	Size distribution	Min. radius r_0 (m)	Exponent (k_r)	Match P_{32} $r_0 = \infty$ (1/m)
FFM01	NE	Global	Power Law	0.66	3.02	1.74
FFM01	NS	Global	Power Law	0.06	2.78	1.29
FFM01	NW	Global	Power Law	0.59	2.85	0.95
FFM01	SH	Global	Power Law	0.82	2.85	0.63

Note: FFM01 contains five additional fracture sets, defined as local sets, representing highly localized stress environments. They are not accounted here.

In summary, DFN obeys a power-law size distribution with exponent $k_r + 1$ and α term defined from the P_{32} provided by SKB. (P_{32} is a fracture density defined as the area of the fractures within the volume of rock mass.) Orientations are distributed according to Fisher distributions (given here as trend and plunge, and converted into dip and dip direction). Positions of the fractures centers are generated as a Poisson's process uniformly throughout the domain without considering physical constrains that could affect relative position of the fractures.

4.1.6.2 DFN Generation

Five DFNs are generated in a cubic domain with the size $L = 20$ m, centered at (0;0;0). Fracture sizes (diameters) are in the range [0.5 m;100 m]. Note that for fracture sets, where r_{min} is larger than the minimum generation size (here $r_{gen} = 0.25$ m), only fractures larger than r_{min} are generated.

During generation of DFNs, each set is generated in two steps:

- fractures between 0.5 m and 20 m in diameter are generated in a domain larger than twice the final domain; and
- fractures between 20 m and 100 m in diameter are generated in a 200-m-edge cube.

Finally, only fractures within or intersecting the final domain are kept. Each DFN contains approximately 13,000 fractures. A plot of a DFN realization and the corresponding stereonet of orientations are shown in Figure 39.

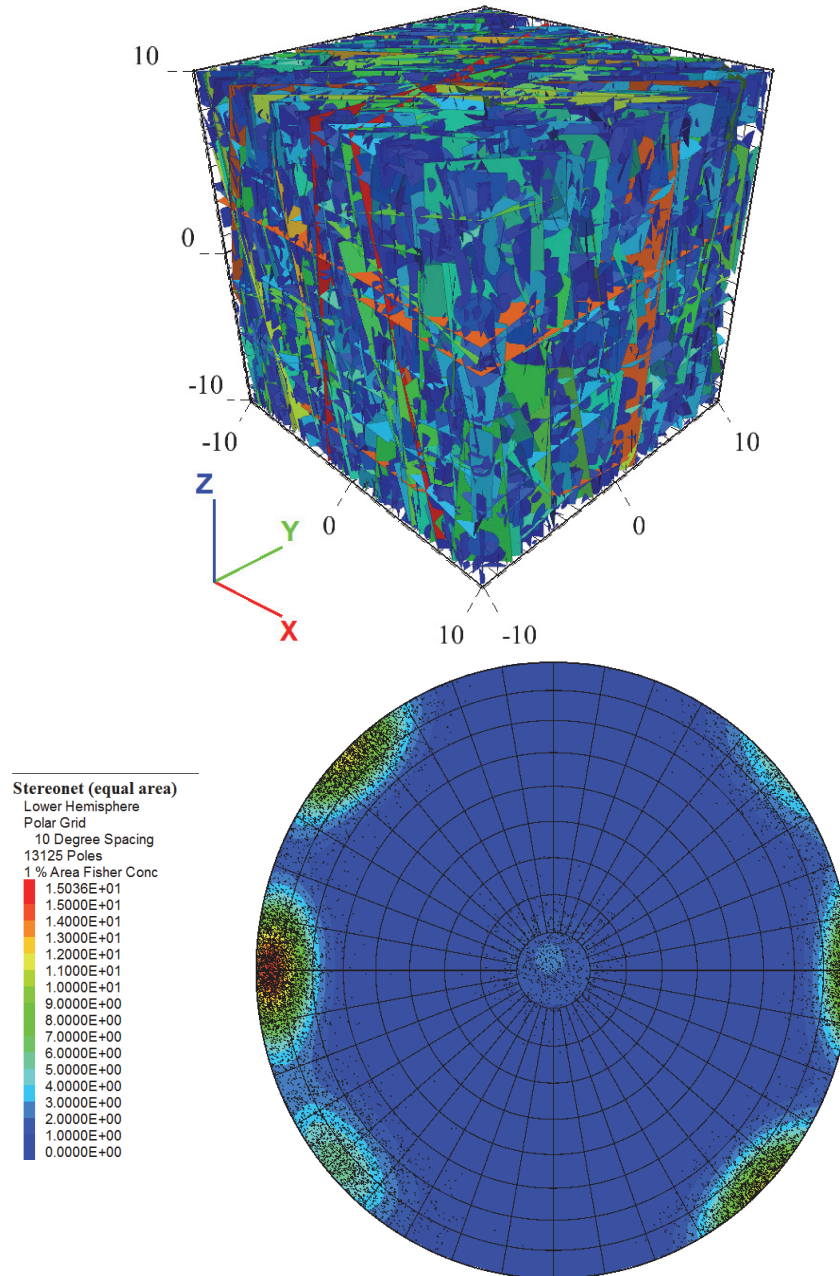


Figure 39: DFN Fractures, Colored by Area (top) and Stereonet of Orientation (bottom)

4.1.6.3 DFN Simplification

The generated DFNs have a large number of fractures. For computational purposes the DFNs needed further simplification by:

- disregarding fractures with minimum fracture radius less than 1 m (diameter of 2 m); and
- restricting the minimum angle of intersection of fractures to five degrees.

Plots of the simplified DFNs for three realizations as used in the numerical simulations are shown in Figure 40.

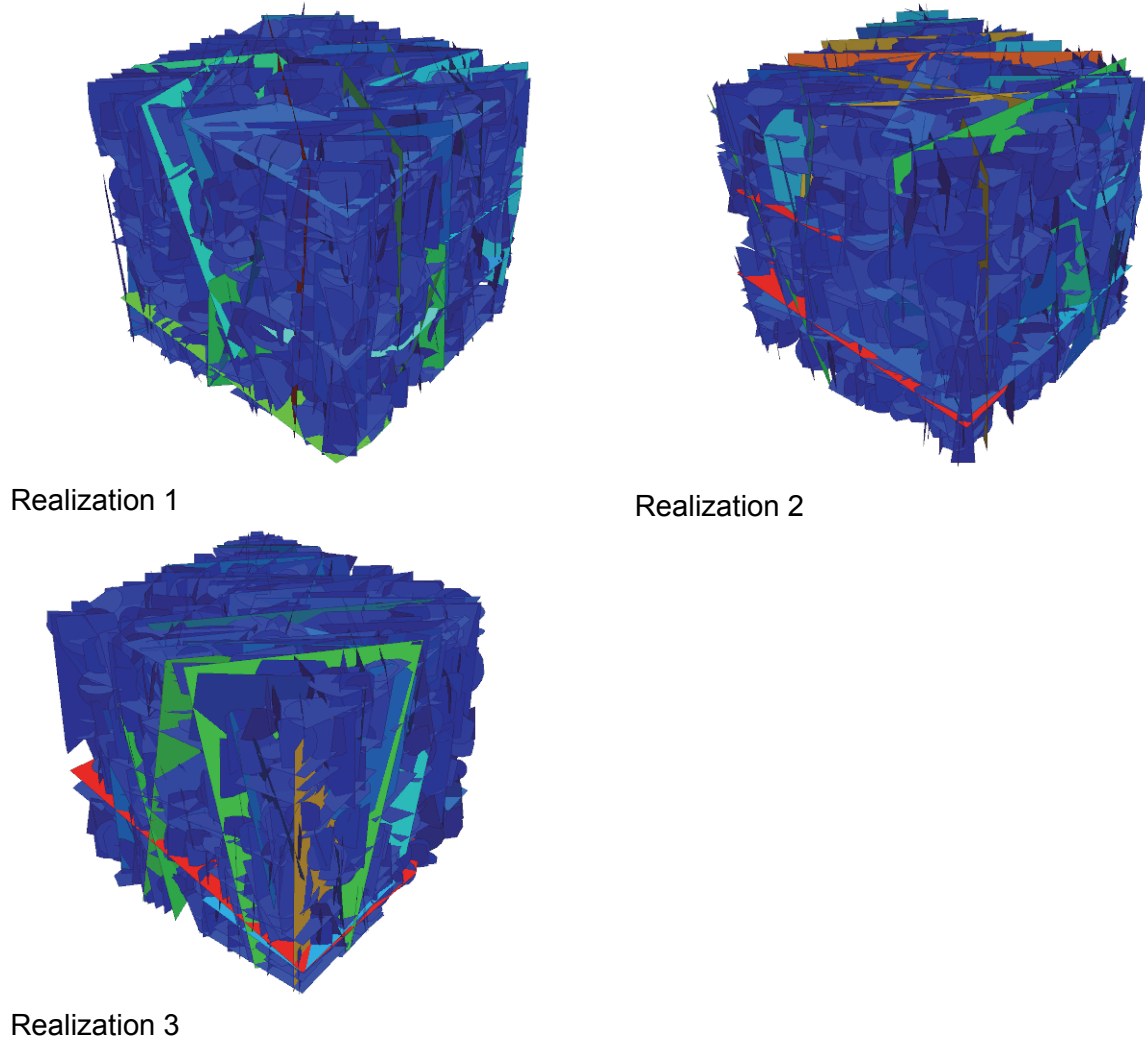


Figure 40: Three Different Realizations Used in 3DEC Analyses: DFNs are Simplified with a Minimum Fracture Radius of 1m.

4.1.6.4 DFN Mechanical Parameters

At this stage, the mechanical characterization of the DFN is not available. Therefore, typical but conservative strength parameters for pre-existing joints were selected for this analysis. The joints were assumed to have no tensile or cohesive strength. The friction angle was assumed to be 30° . The normal and shear stiffnesses of the joints should have less effect on the predicted slip on the joints. Therefore, those parameters were selected such that the joints behave as relatively stiff compared to the surrounding blocks. The joint normal stiffness was selected to be 700 GPa/m; the shear stiffness is ten times less, 70 GPa/m.

4.1.7 Backfill Materials

The mechanical and thermal properties of the backfill materials, components of the engineered barrier system, are listed in Table 7 and Table 8, respectively. In all analyses, the backfill materials are considered to be linearly elastic (SNC-Lavalin 2014).

4.2 GEOLOGICAL AND REPOSITORY INDUCED PERTURBATIONS

The long-term stability of the placement rooms is analyzed considering different processes and loads that can affect their stability over a period of 1 Ma, including in situ stresses, time-dependent strength degradation, pore pressures (inside the rock mass) and multiple glacial and seismic events. The analysis has been carried out for in situ stresses, thermal loading, time-dependent strength degradation, pore pressures in rock mass and multiple glacial ice sheet advances and retreat occurring concurrently as the base case.

The glacial events occur periodically, with variable time intervals between the events (of the order of tens of thousands of years), variable duration of the events (of the order of thousands of years) and variable maximum thickness of the ice sheet. The time histories of the glacial loads are results of a glaciation and earth crust deformation models used are those of Peltier (2011) and Wu (2013) for the location of the hypothetical repository site in crystalline rock.

Stability of the rooms, subject to seismic events with 10^{-5} and 10^{-6} probabilities of annual exceedance like the ones for the sedimentary site (Section 3.27), also was considered assuming that seismic events occur at different stages during degradation of the rooms (as result of thermally-induced stresses, time-dependent strength degradation and multiple glacial cycles). The seismic analyses were conducted for two critical states: 1) when the peak temperature was reached in the rock mass, and 2) when the maximum vertical glacial loading was reached. As the main effect of seismic loading on underground excavations is due to stress change, the critical states were selected as the states when maximum stresses are achieved in the rock mass. The seismic analyses were conducted for the lower probability seismic events only, because the analyses have shown that even those stronger events do not have significant effect on room stability or on the extent of the damage around the rooms.

Different loading conditions and their representation in the models are discussed in this chapter.

Both hypothetical sedimentary and crystalline rock sites are set in low seismicity North American interior continental region and thus have a similar tectonic setting. According to 2010 National Building Code hazard maps (NBCC 2010), the expected ground motions at the crystalline site are slightly lower than those at the sedimentary site. Therefore the use of ground motions for the sedimentary rock site (Section 3.2.6.1), should be slightly conservative if applied to the crystalline rock site.

4.2.1 In-Situ Stresses

In situ stress state in the crystalline geological setting was defined in three domains (NWMO 2014). The domains and the stresses are specified in Table 20. These stresses are implemented in the mechanical models as the initial in-situ stresses.

Table 20: In-situ Stress State (NWMO 2014)

Domain	Depth range (m)	Stresses
1	0 – 300	$\sigma_H = 0.071 \text{ MPa/m} + 5.768 \text{ MPa}$ $\sigma_h = 0.043 \text{ MPa/m} + 3.287 \text{ MPa}$ $\sigma_v = 0.034 \text{ MPa/m}$
2	300 – 600	stresses assumed to increase linearly from values at base of Domain 1 to values corresponding to top of Domain 3.
3	600 - 1500	$\sigma_H = 0.026 \text{ MPa/m} + 23.636 \text{ MPa}$ $\sigma_h = 0.016 \text{ MPa/m} + 17.104 \text{ MPa}$ $\sigma_v = 0.020 \text{ MPa/m} + 1.066 \text{ MPa}$

4.2.2 Thermal Loading

The initial temperature field in the crystalline setting is assumed to have a constant gradient of 0.012 °C/m, with the initial temperature of the ground surface of +5°C (NWMO 2014). The average temperature at 500 m depth is +11°C.

The characteristics of the UFC for Mark II repository design are listed in Table 9 (NWMO 2014). The heat release rates per an UFC and per unit volume of the UFC for a post-reactor discharge time of 30 years (i.e., the waste placement time) are listed in Table 10 (NWMO 2014). The heat release rates listed in Table 10 were considered as the initial heat release rates in the analysis. In the near-field models, which is 3D and explicitly represents the UFC, the thermal heat source is represented as the heat release rate per unit volume assigned to the model zones within the UFC. In the far-field model, the heat source is distributed over the layer of the zones that covers the panel layout in the plan view. That height is equal to the difference between the top coordinate of the upper layer of the UFC and the bottom coordinate of the lower layer of the UFC. The volumetric heat source for the far-field models is calculated by averaging the power of the single UFC over the tributary area in the plan view (i.e., center-to-center spacing between the adjacent UFC times the center-to-center spacing of the placements rooms).

The heat release rate (or power) decays with time as a result of radioactive decay of the waste. The decrease of the power, relative to the power at time of placement, is illustrated in Figure 11. The multiplier given by this chart is used to scale the heat release rates as a function of time in all of the thermal models.

4.2.3 Long-Term Strength Degradation

One objective of the analysis presented here is to predict degradation and development of the EDZ around the placement rooms due to long-term (1 Ma) rock-strength degradation of the host rock units around the repository excavations subjected to in situ and glacially-induced stresses.

4.2.3.1 Static-Fatigue Curves and Evolution of Damage Due to Strength Degradation

The static-fatigue (long-term) behaviour of a rock forms the basis of the model for simulating time-dependent processes. The static-fatigue curves, which are obtained from laboratory tests on small, intact rock, samples, provide the time-to-failure (t_f) of the material at a particular driving-stress ratio, σ / σ_c (see Section 3.2.3).

Schmidtke and Lajtai (1985) established the static-fatigue relation for unconfined Lac du Bonnet granite and Lau et al. (2000) evaluated the static-fatigue relation for confined (5 MPa and 10 MPa) samples (Figure 12a). Data sets for each confinement were fit with a straight line, and the line was extrapolated to encompass driving-stress ratios measured. The approximation of static-fatigue line as used in the long-term stability analyses is shown in Figure 12b.

The long-term strength threshold for intact rock is approximated by the crack initiation stress as proposed by Damjanac and Fairhurst (2010). No data are available for time-dependent strength degradation and long-term strength threshold of granite rock mass. The rock mass (short-term) UCS is already degraded 50% compared to the intact rock UCS. To ensure that the model predictions are conservative regarding the effect of the time-dependent strength degradation, the long-term strength threshold for the granite rock mass was taken to be 40% of the rock mass UCS. In this case such approximation was acceptable because the long-term stability of the placement rooms will not be very sensitive function of the long-term strength threshold of the granite rock mass, due to confinement provided by the backfilling material.

Once the lower-bound long-term strength was established, the next step was to develop a numerical process that degrades the short-term strength to the long-term strength. The evolution of damage, expressed in terms of the damage coefficient, D , which is the ratio of the degraded to the initial strength, for the Lac du Bonnet granite was developed using the discrete element software PFC (Itasca 1999, BSC 2004) and is shown in Figure 13.

Like the sedimentary rock in Section 3, the two parameters control the predictions of time-dependent strength degradation are: 1) time-to-failure, and 2) damage evolution (rate) before time-to-failure. It was confirmed in Section 3.2.3 that the considered variation of damage rates has no practical effect on predicted rockfall despite that time-to-failure is the main factor controlling evolution of the rockfall due to time-dependent strength reduction.

4.2.3.2 Time-dependent Strength Degradation in UDEC

Implementation of the time-dependent strength degradation scheme in the room stability model, which uses UDEC Voronoi block model (Section 4.1.3) for Mark II design analysis, is discussed in detail in Section 3.2.3.

4.2.4 Glacial Loading

Details of consideration of the effect of potential glacial events on stability of the DGR are discussed in Section 3.2.4. The glaciation case that resulted in the greatest vertical stress (histories of all independent stress components shown in Figure 41) for potential location of the repository in the crystalline setting was used in the long-term stability analysis of the repository and the placement rooms.

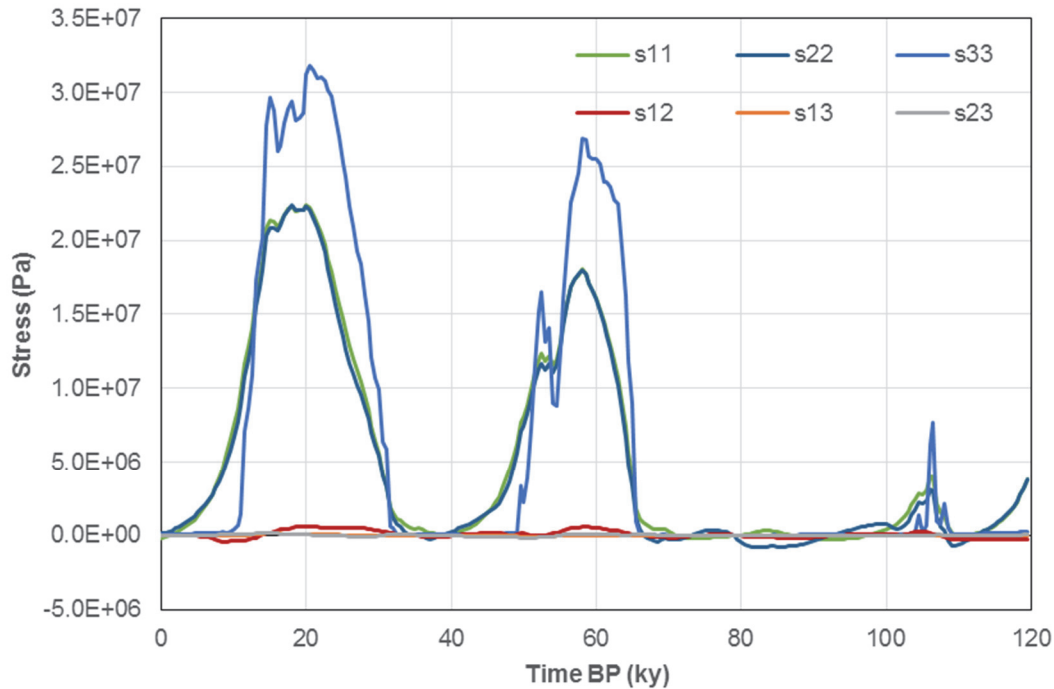


Figure 41: Calculated Glacially-induced Rebound Stress Histories (BP = before present); s11, s22, and s33 are the Normal Stress Components, s12, s13, and s23 are the Shear Stress Components

The conditions for the next advance of continental scale glaciation will not be favourable for approximately another 60,000 years (Peltier 2011). However, predictions of possible variations of the ice thickness during future glaciations are not available. The analysis is conducted assuming that the sequence of the glacial events and corresponding histories of the rebound stresses predicted for the L9930-Lith075-UM6E20LM3E21 (Wu 2013) case will occur in future starting at 60,000 years after the present. The rebound shear stresses (s12, s13 and s23 in Figure 41) are much smaller than the normal stresses (s11, s22 and s33 in Figure 41). Consequently, they were neglected in the analysis. The rebound stress histories, as considered in the analysis, are shown in Figure 42. The x-axis shows the time relative to the onset of the glaciation, 60,000 years after the present. Each glacial rebound stress increment (including all three normal stress components) was read into the model to increment stress state throughout the domain that represents the rock mass. Subsequently, the model was run to equilibrium. The stress increments due to the rebound stresses were initialized (i.e., not applied as the boundary conditions). Consequently, the model does not predict the elastic deformation of the entire geological setting caused by the change in the glacial loading. Instead, predicted are only elastic rock mass deformation at placement room horizon and inelastic deformation due to yielding and damage of the rock mass.

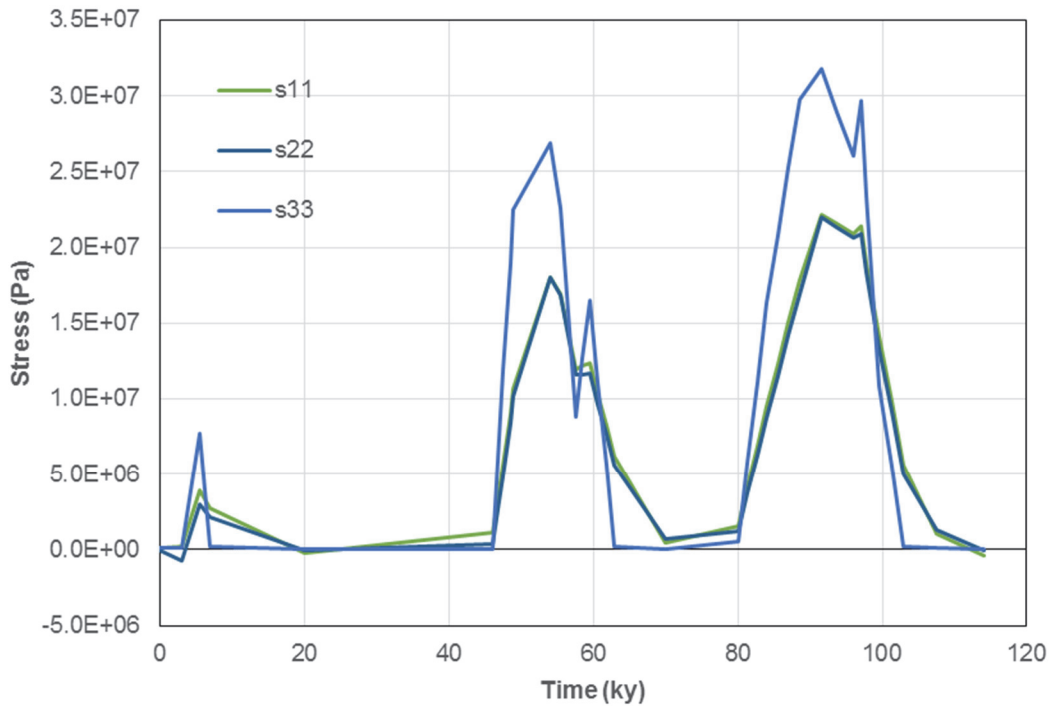


Figure 42: Approximation of Glacially-induced Rebound Stress Histories Used in Repository Stability Analysis

4.2.5 Seismic Loading

4.2.5.1 Ground Motions and Damping

Stability of the placement rooms was analyzed for seismic ground motions, which could be generated by earthquakes with an annual probability of exceedance of 10^{-5} p.a. for the reference case and 10^{-6} per annum (p.a.) for the extreme case. The ground motion time histories were developed for the ground surface, but also at depths of interest to be used as inputs as the ground motions at the base of the models for stability analysis. Thus, different time histories were used for the placement room analyses. The ground motions used as the inputs to the analyses include the surface reflections, because the numerical models do not extend to the ground surface (i.e., they are truncated at some height above the structure of interest) and use the non-reflecting boundaries at the model top.

Ground motions were not available for the hypothetical site in the crystalline setting. Conservative three dimensional ground motions generated for the hypothetical sedimentary site were adopted in the modelling. Similar to the repository in sedimentary rock, three seismic scenarios with combinations of the earthquake magnitude and the distance from the repository match the uniform hazard spectra at each probability level of 10^{-5} and 10^{-6} p.a. for the entire frequency range (AMEC Geometrix 2011). Time histories for each seismic scenario include two horizontal components (H1 and H2) and one vertical component (V) and are shown on Figure 17 to Figure 19. The scenarios and the corresponding peak ground velocities (PGVs) and peak ground accelerations (PGAs) for each scenario and each motion component at the repository level are listed in Table 11 (AMEC Geometric 2011). The placement room stability simulations

were carried out using only local damping amounting to approximately 1.5% of the critical damping.

4.3 DESCRIPTION OF THE MODELS

4.3.1 Modelling and Coupling Approach

Different simulations conducted for the repository in the crystalline setting and their relation are illustrated in Figure 43. In order to optimize numerical simulations of coupled thermo-mechanical models, the thermal and mechanical models were simulated separately. Such approach was possible because the coupling is one-way. The thermal model affects the mechanical, but not the other way around (i.e., the effect of mechanical model on temperature changes is negligible). Thus, the thermal models were simulated first.

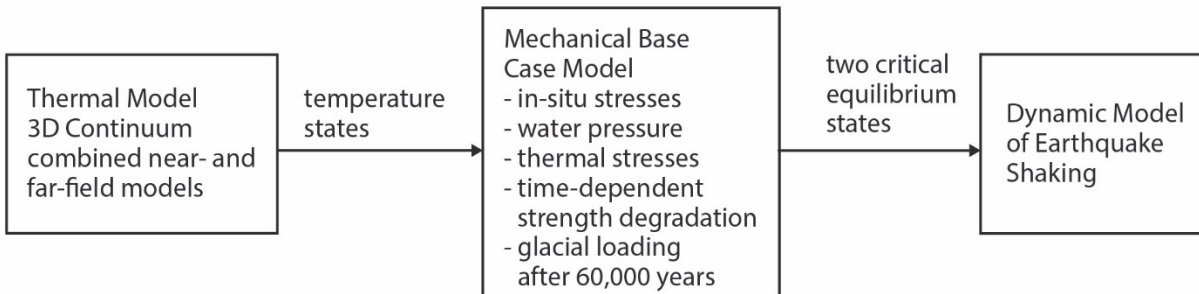


Figure 43: Simulation Chart

During the simulation of the thermal model, multiple model states were saved. The time increment between any two saved states was determined from the condition that the maximum temperature change in the model is equal to or less than 5°C. The temperature fields predicted in the thermal model were then sequentially imported in the mechanical model. The mean stress increment, $\Delta\sigma_m$, can be expressed in terms of temperature change, ΔT , bulk modulus of the solid material, K , and the linear coefficient of thermal expansion, α as:

$$\Delta\sigma_m = -3\alpha K\Delta T \quad (12)$$

The thermal analysis was actually conducted using two models: near- and far-field models. The near-field models represent the details of backfill and room geometries. They include only one placement room, but use a symmetry condition (adiabatic thermal boundary) at half-distance between the adjacent rooms to represent the repository with multiple rooms. Thus, the near-field model at early times correctly approximates (with a small error) the temperature around the placement room. At longer times, the near-field model is a representation of temperatures assuming that there is an infinite number of the rooms on both sides of the analyzed room. That is an approximation that results in overestimation of temperatures for the long times. In addition, simulation of the near-field model for a period of 1 Ma can be very time consuming. Therefore, the temperatures around the repository were also analyzed in the far-field models. In these models, the repository is represented as a planar heat source over the area of the repository panels, or the layer of zones on the repository level within the outline of the repository panels.

Both near- and far-field models extend to the ground surface and 2,000 m below the ground surface. The far-field model extends laterally far enough that it can be assumed that the initial temperatures are insignificantly affected for simulated period of 1 Ma.

In the temperature fields used in the thermo-mechanical analyses, the transition from temperature fields predicted in the near-field model to those from the far-field model was made at approximately 50,000 years. This is a conservative approximation because the near-field model over-estimates the temperature around the repository after 2,000 years. The temperature fields from the near- and far-field models are imported into the mechanical model sequentially and used in calculation of the thermally induced stresses.

The placement rooms (the invert) and repository horizon are at 500 m depth. The models use the thermal properties as defined in Table 15. The temperatures at the base and the top of the models are fixed at the initial values. The volumetric thermal source as defined in Table 10 (separately for the near- and far-field models) and by the decay curve (shown in Figure 11) is distributed over all elements (zones) that represent UFC (e.g., "UFC" group in Figure 44), in the near-field models, and the repository panel, in the far-field models.

4.4 MODELLING MARK II DESIGN IN CRYSTALLINE ROCK

4.4.1 Thermal Model

The details of the geometry of the near-field thermal model in crystalline rock are illustrated in Figure 44. The model is created taking advantage of four planar symmetries (indicated in the figure) of the analyzed problem. The vertical model boundaries are along those four symmetry planes. Two are perpendicular to the room axis: one through the center of the UFC in the lower row and the other through the center of the adjacent UFC in the upper row. Two other vertical model boundaries are parallel with the room axis. One of those boundaries is along the room axis; the other is at half-distance between two adjacent rooms. All four vertical model boundaries along the four planes of symmetries are considered as adiabatic in the thermal model.

The geometry of the far-field model in crystalline rock is shown in Figure 45. The plot illustrates geometry of one panel. The repository layout includes four panels. In this model, two planar symmetries are used. Only one panel is explicitly represented. Two vertical model boundaries are along the two mutually perpendicular symmetry planes between four panels. Those boundaries are considered adiabatic in the thermal model. Two other vertical boundaries are truncation boundaries at sufficient distance from the repository that temperature change during the simulated time of 1 Ma can be neglected. Those two boundaries are at 3,265 m and 3,511 m from the center of the repository. The thickness of the layer of the zones that represent the panel is 1.6 m, or the difference in the elevations of the top of the UFC in the upper row and the bottom of the UFC in the lower row.

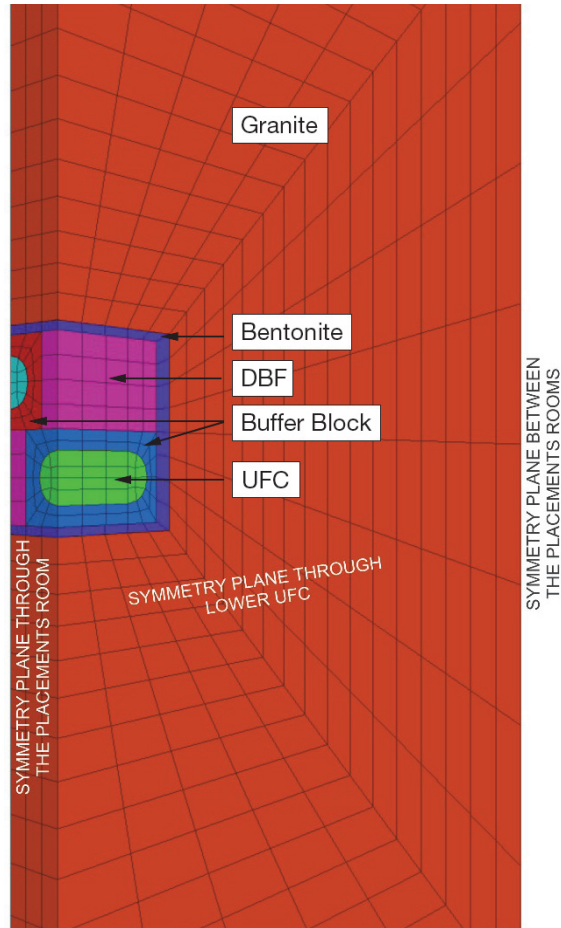


Figure 44: Detail of Geometry of the Near-Field Thermal Model in Crystalline Rock

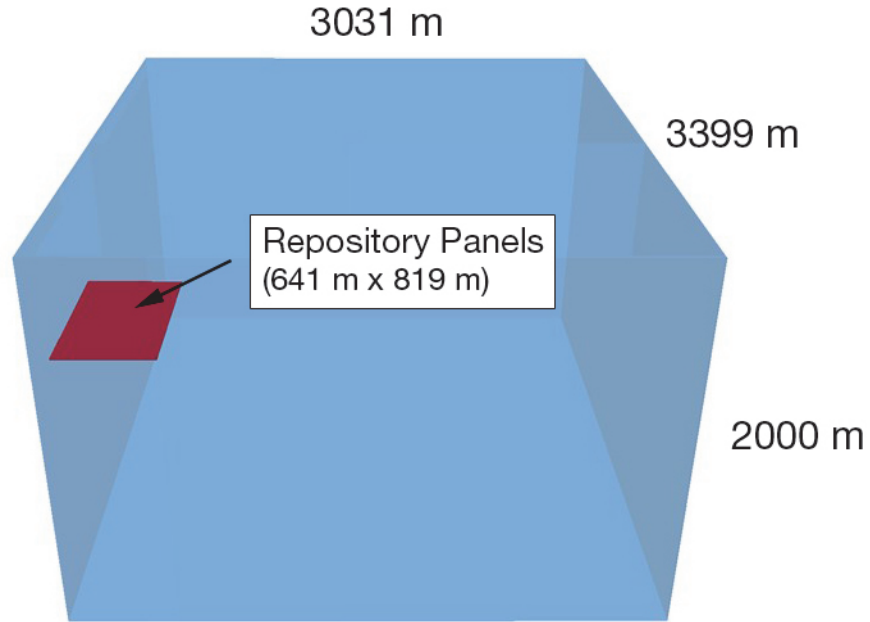


Figure 45: Geometry of the Far-Field Thermal Model in Crystalline Rock

4.4.2 Mechanical Model

The deformation and damage around the placement rooms in the sedimentary settings was analyzed in a two-dimensional model. The geometry of the model, including a single geological domain and the placement room, is shown in Figure 46. The model is in the plane perpendicular to the room axis. It includes a single room and extends laterally on both sides of the room to the vertical symmetry planes at the half-distance to the adjacent rooms. It extends 34 m above and below the repository. The model truncation in the vertical direction was justified because the mechanical effects due to the placement room will not extend vertically beyond the distance of 34 m. In the rectangular region, 9.5 m wide and 10 m high, around the center of the room, the rock mass is represented as an assembly of Voronoi blocks (discussed in Section 4.1.3) as shown in Figure 47. The average size of the Voronoi blocks is 0.1 m.

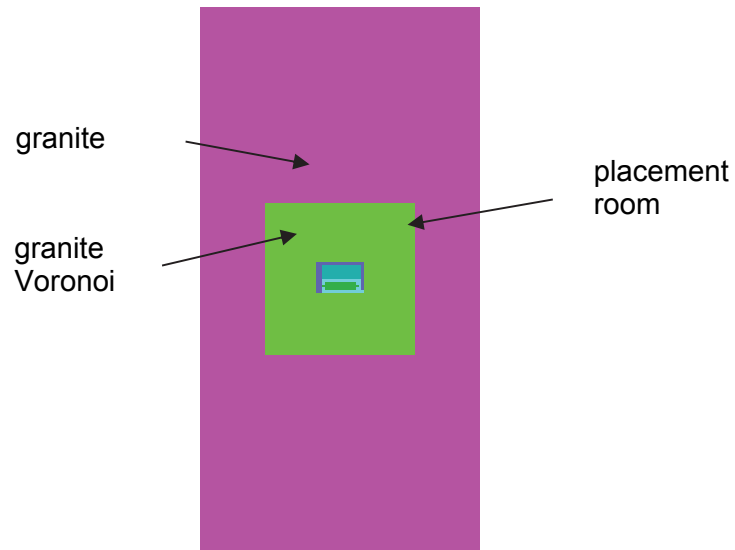


Figure 46: Geometry of the Near-Field Mechanical Model in Crystalline Rock

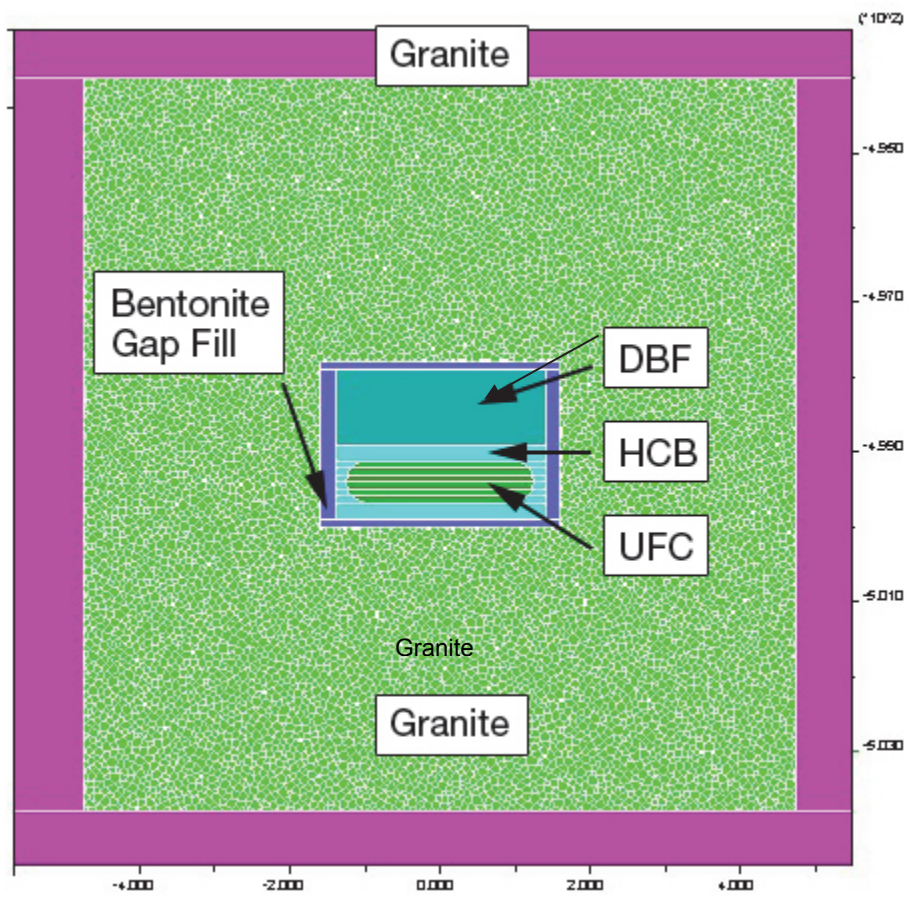


Figure 47: Detail of Geometry of the Near-Field Mechanical Model in Crystalline Rock

4.4.3 Static Model

On the model vertical boundaries, corresponding to the symmetry planes, “roller” boundary conditions were applied in the static analysis. (Rollers allow displacements in the plane of the boundary but restrain any displacement perpendicular to the plane of the boundary.) The bottom boundary was fixed in all three directions. The stress boundary condition was applied on the top model boundary: 1) the vertical stress is equal to the weight of the overburden, and 2) shear stresses are zero.

4.4.4 Dynamic Model

The geometry of the dynamic model is same as the geometry of the static model (shown in Figure 47). The dynamic analysis of the model response to seismic shaking was analyzed for two initial equilibrium states. The first was at the time of the maximum temperature at the room wall, 27 years after waste emplacement. The second state was at the time of the maximum vertical glacial load, 150,000 years after waste emplacements. Those two equilibrium states were considered to result in conservative load combinations. The same model used for analysis of stresses, deformation and damage around the repository due to static thermo-mechanical effects, was used for dynamic simulation of the model response to seismic shaking. The boundary conditions of the dynamic and static mechanical models are different. The seismic loading is applied at the model base as the vertically incoming stress wave. The velocity histories (shown in Figure 17 through Figure 19) are converted to the normal and shear stress history using the relation between the stresses and velocity for P and S body waves. For the two-dimensional model only one horizontal velocity (or, equivalently, shear stress) history perpendicular to the room axis was applied at the base of the model. It was always velocity history with greater PGV. The horizontal velocity history along the room is not expected to affect deformation and damage of the rock mass. Consequently, it was neglected in the analyses. Viscous dashpots were applied on the top and bottom model boundaries. This boundary condition allows seismic wave to pass through the boundary without significant reflections. Free-field boundary condition was applied on two vertical boundaries. This boundary condition represent response of infinite half-space to vertically propagating waves coupled viscous dashpots. In this case, the viscous dashpots dissipate only the outgoing waves resulted from the reflection of the seismic wave with the placement rooms. These boundary conditions neglect interaction between the adjacent rooms during seismic shaking. However, considering the spacing between the rooms relative to their size, the approximation is reasonable.

4.4.4.1 3D Model with Explicit Representation of DFN

The effect of discrete fractures on deformation and stability of the placement rooms was analyzed in the three-dimensional model. In this model, the fractures were explicitly represented. Three-dimensional distinct element code, 3DEC was used for the analysis. Five DFN realizations were developed as described in Section 4.1.6 and imported into the 3DEC model. Multiple fracture realizations were considered in order to address the effect of spatial variability and uncertainty in fracturing along the placement rooms. This study was conducted for Mark II design only.

In these models the rock mass properties (Table 14) were assigned to the blocks between the joints that were explicitly represented. The typical dimension of the blocks created by the simplified DFN is of the order of couple of meters. Thus, the mechanical properties of the blocks needed to be scaled compared to the intact rock properties. The empirically determined rock mass properties are reasonable (and conservative) approximation of the properties of the rock mass on the scale of the blocks in these models.

The geometry of the 3DEC model is shown in Figure 48. The model dimensions are 20 m × 20 m in the plan view. In the vertical direction, the model extends 34 m below and above the repository (same as in the two-dimensional UDEC model). Two vertical model boundaries are in the symmetry planes parallel to the room axis, half-distance between the rooms. Two other vertical boundaries were perpendicular to the room axis, 20 m apart from each other. These boundaries are truncation boundaries required for a model of finite size. The roller boundary condition was used on all vertical model boundaries. The base of the model was fixed; the stress boundary condition was applied on the top of the model: 1) the vertical stress is equal to the weight of the overburden, and 2) shear stresses are zero. The DFN was explicitly represented in the 20-m-edge cubic region centered on the placement room (Figure 48).

The effect of pre-existing fractures on deformation and stability of the placement rooms is investigated for induced stresses due to coupled thermo-hydro-mechanical processes and loading conditions. Specifically, two critical states were considered: 1) 27 years after placement of the waste, when the peak temperature is reached in the rock mass, and 2) 151,500 years after placement of the waste, when the maximum vertical glacial load is reached. The stress states at those two critical states, obtained in the UDEC model by following the entire loading histories, were imported into the 3DEC model. After the 3DEC model was equilibrated for imported stresses under elastic conditions in the rock and joints, the realistic joint properties were assigned. After equilibrating the model again, it was possible to estimate if the explicit joints will experience any significant deformation for considered critical loading conditions.

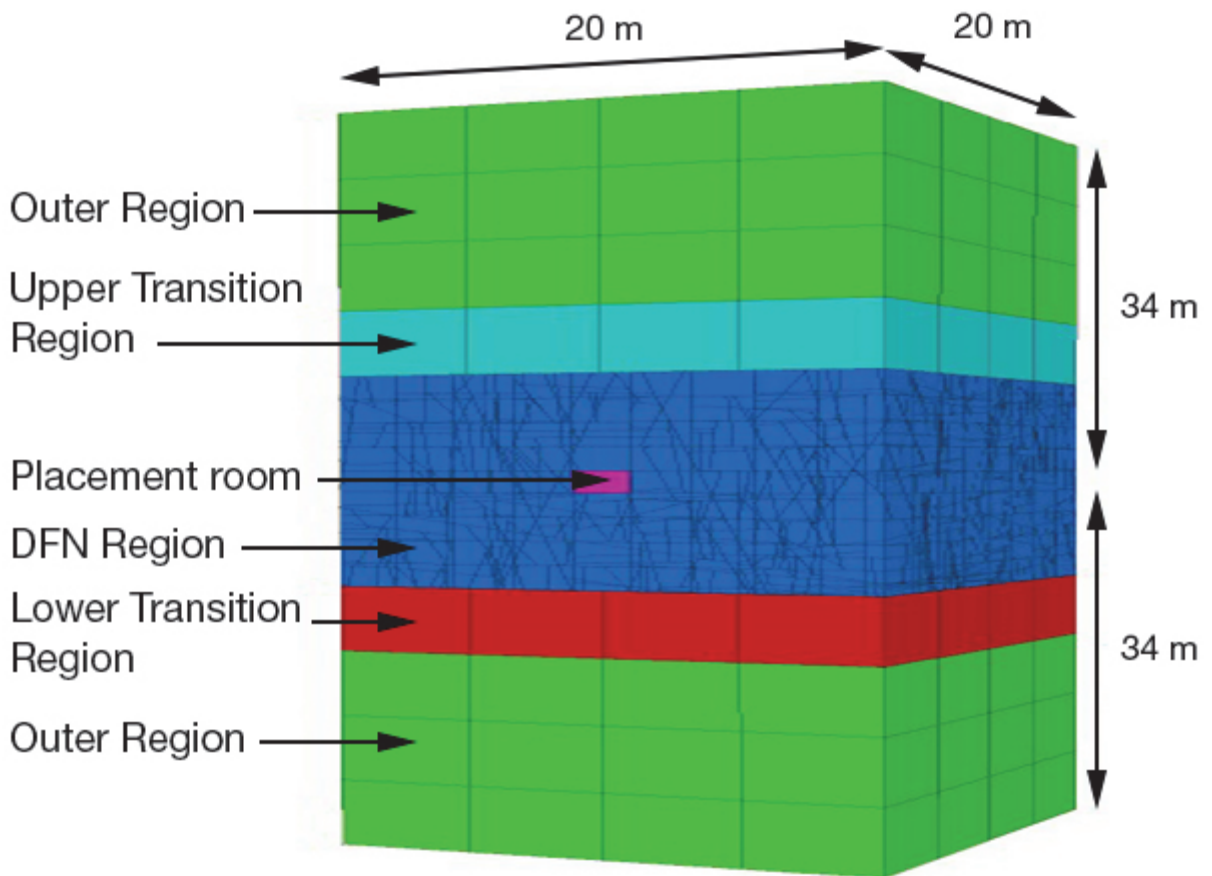


Figure 48: DFN Region in the 3DEC Model

4.5 MODELLING RESULTS

4.5.1 Evolution of Temperatures

The locations of the points within the near-field model for which the temperature histories are provided are shown in Figure 49. The temperature histories from the near-field models at those three points and from the far-field model at the center of the modelled quarter of the repository are shown in Figure 50. The trends of the near- and far-field model temperatures are similar as in the Mark II model for sedimentary rock setting. The temperature histories reveal that the near-field model consistently shows greater temperatures than the far-field model. This is attributed to the fact that the far-field model has a finite size and the heat source in the model is distributed over the surface of the repository panels. Whereas, the near-field model represents a repository of an infinite size. The near-field model provides a good approximation of the temperatures near the repository during relatively short time of a thousand plus year after waste placement. After then, the near-field model overestimates the temperatures resulted from the artifact of numerical modelling. The far field model, however, could provide a good approximation of the repository temperatures for relatively long times after the initial thousand years. This phenomenon has been studied by Guo (2007). Reasonable temperature histories can be obtained by modifying the near-field modelling results by subtracting the temperature differences between a finite and an infinite far field models (Guo 2007).

In the thermo-mechanical analysis, the temperature is assumed to be a combination between the temperatures predicted by the near- and far-field models. The combination is conducted in such a way to ensure bounding thermally induced stresses. Consequently, the temperatures from the near-field model were used for such time to result in overestimation of the temperature toward the end of the period for which the near-field model temperatures were used. In the current analysis, the temperatures from the near-field model were used until 60,000 years after UFC placement. The temperatures for the subsequent times were approximated using the results of the far-field model. The combined temperature history for Point 1 is shown in Figure 51. For comparison, the temperature history of the proposed general configuration of the placement room and backfill were created based on Guo (2007), shown in the same plot. Comparison of these two curves offers confidence that the combined temperature history used in thermo-mechanical analysis is conservative (i.e., always overestimates the temperature). The figure also shows that the long-term temperatures calculated by the near-field analysis were affected by the aforementioned numerical modelling artifacts beyond the first temperature peak.

The temperature at Point 1 peaks at 84.6°C in 1570 years after waste placement (the maximum temperature of the surface of the UFC is 0.1°C hotter), while the surface of the rock excavation (point 2) at temperatures of 84.5°C and 83.2°C in 1570 years and 1600 years, respectively. The insulating effect of the backfill can be seen slowing the radiation of the heat flux from the UFC. For rock mass 9 m above the placement room, Point 3, the peak temperature is lower at 81.2°C and occurs in 1600 years after UFC placement. The temperature contours at some characteristic times as obtained from the near-field model are shown in Figure 52. The temperature contours at some characteristic times, as obtained from the far-field, model are shown in Figure 53.

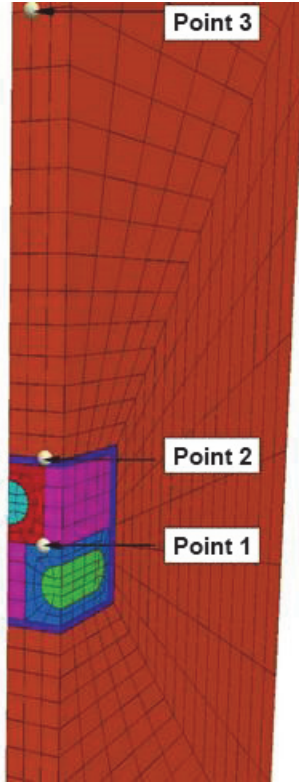


Figure 49: Locations of the Temperature History Points in the Near-Field Thermal Model in Crystalline Rock

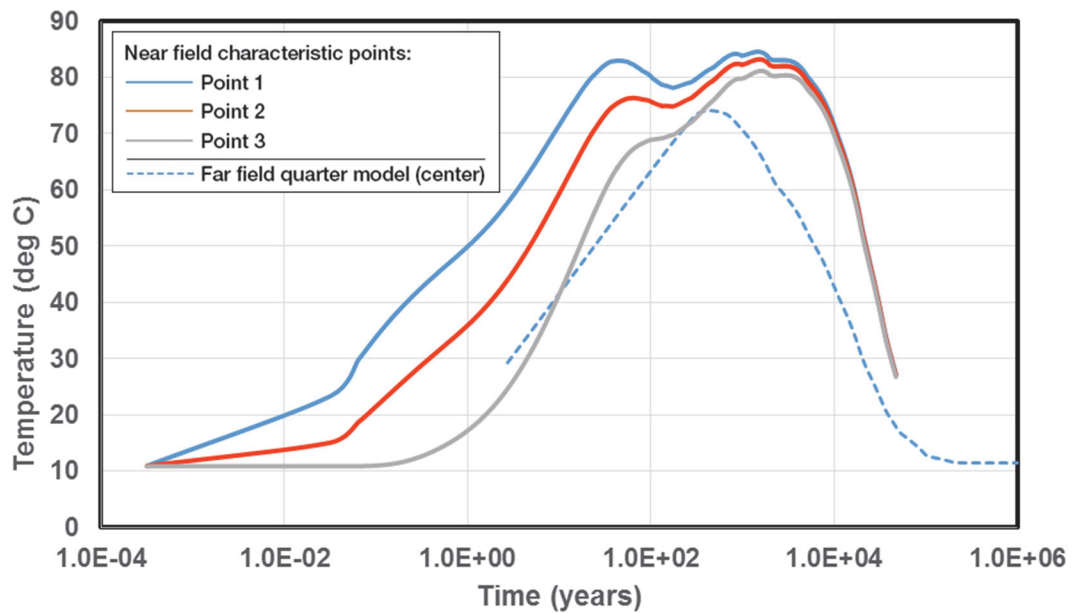


Figure 50: Temperature Histories at Characteristic Points (indicated in Figure 49) as Calculated from the Near- and Far-Field Models in Crystalline Rock

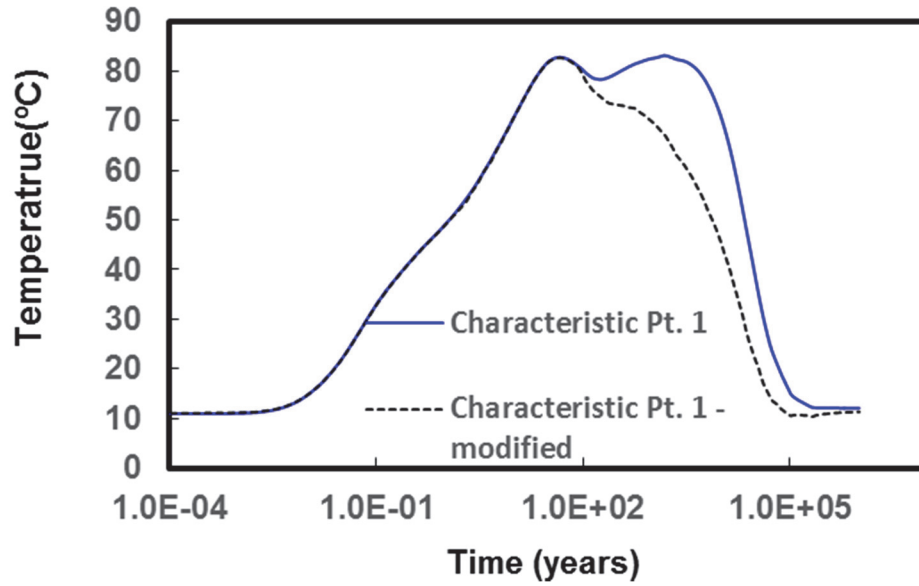


Figure 51: A Comparison Between Modified and Unmodified Combined Temperature Histories at Characteristic Point 1 in Crystalline Rock

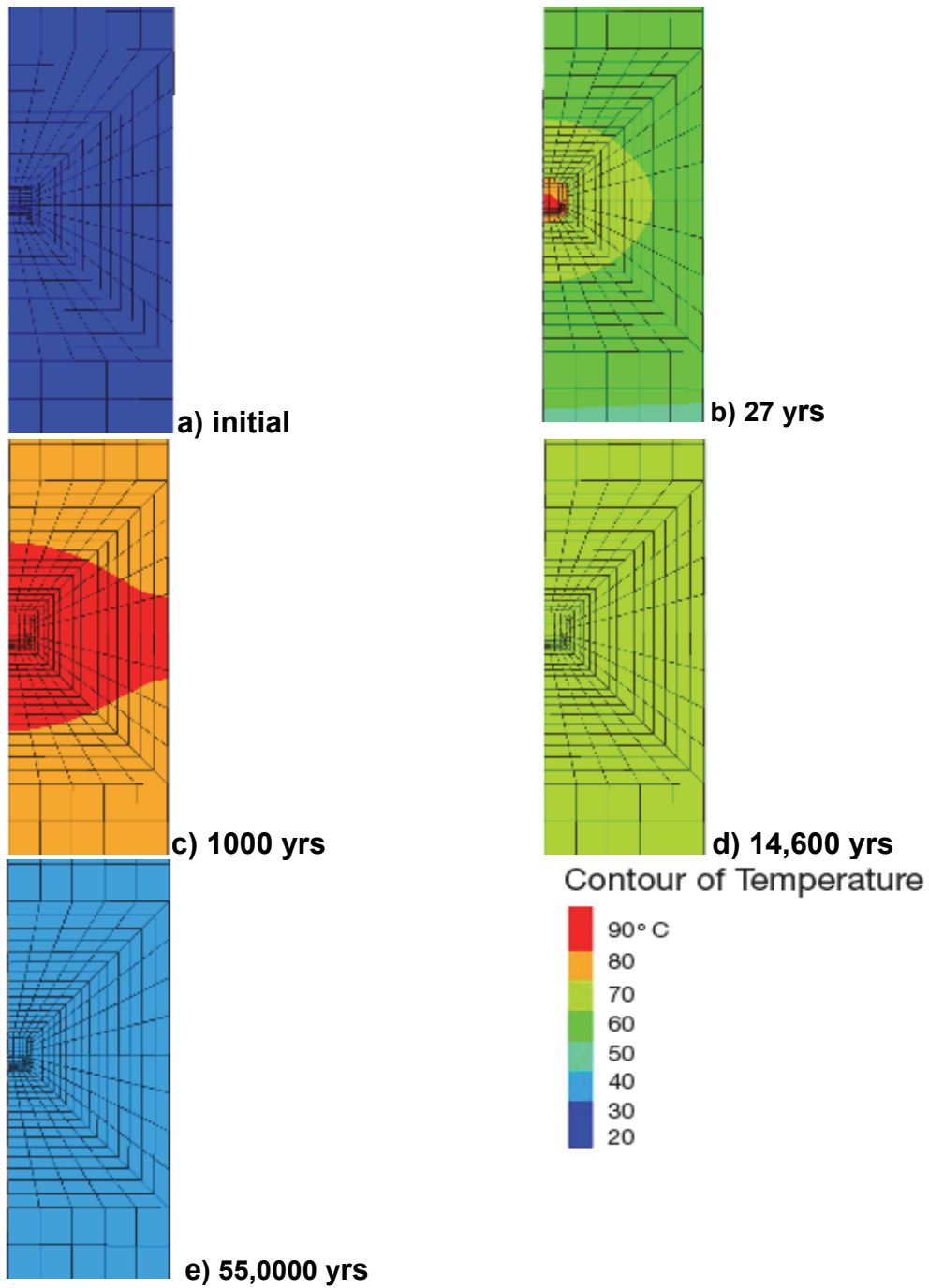


Figure 52: Evolution of Temperature Fields in the Near-field Model in Crystalline Rock

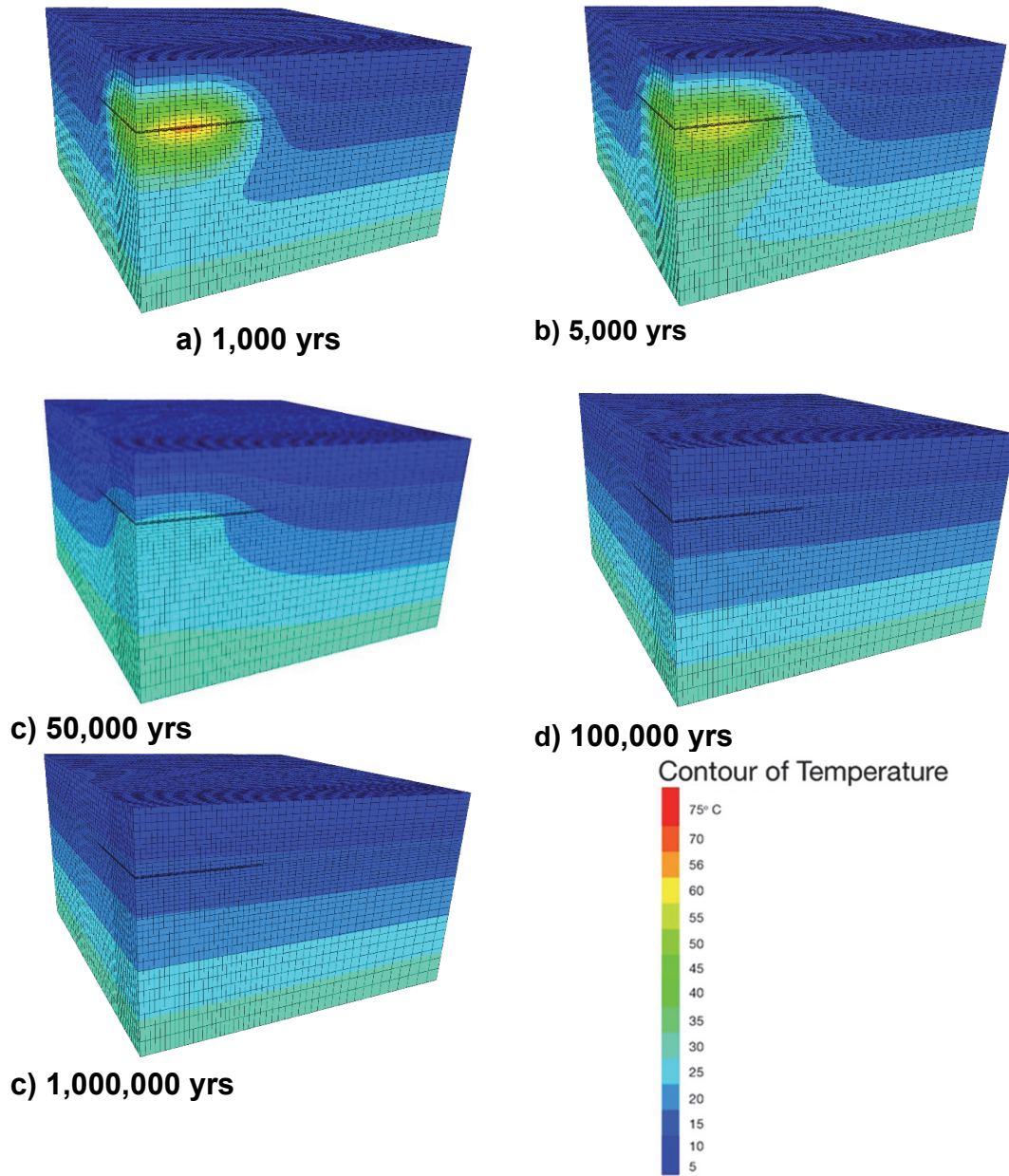


Figure 53: Evolution of Temperature Fields in the Far-field Model in Crystalline Rock

4.5.2 Thermo-Mechanical Loading and Time-Dependent Strength Degradation

After excavation of the room and subsequent filling with UFCs and backfilling materials, damage around the room is minimal, as can be seen in Figure 54a. Up to peak temperature, which occurs at 27 years, the extent of damage is confined to the near vicinity of the opening (Figure 54c). The extent of EDZ is 0.2 m behind the surface of the room walls. As heating progresses, sporadic fracturing of the rock mass around the room increases. The extent of the damage zone reaches the boundary of the Voronoi region, placed at a distance of 3.1 m away from the room wall (Figure 54d). Around the opening, fracture density is higher, and fractures coalesce and form longer more pronounced fractures; fracturing away from the opening, while

present, is still only sporadic with low density. Although microcracks develop at distances greater than 1 m from the room boundary, the peak rock strength has never been reached at those points.

Rock mass heating results in predominantly vertically upward expansion with maximum displacements on the level of the repository predicts in this model on the order of 3.8 cm. This vertical displacement is a consequence of a relatively uniform thermal expansion in the horizontal plane within the repository footprint under condition of stress free boundary condition at the ground surface. The mechanical model probably underestimates the magnitude of the vertical displacement at the repository level because of relatively close bottom boundary of the model and neglected vertical displacement of the column of the rock below the boundary. The underestimate of the uniform vertical displacement on the repository level does not affect the model predictions of placement room stability or rock damage because the neglected uniform vertical displacement does not result in stress change (only vertical model translation). The vertical displacement of the ground surface above the repository will exceed the vertical displacement on the repository level. This mechanical model does not predict the displacement of the ground surface. This expansion is relatively uniform across the entire repository such that differential displacements do not result in the formation or reactivation of fractures in rock mass and, thus, do not influence the integrity of placement rooms.

None of the induced damage represent open fractures or HDZ. EDZ that involves mainly cracking of the intact rock is contained within 1 m distance from the room walls (mainly floor and roof). This maximum damage occurred at approximate 1,000 years after waste deposition.

During the first 50,000 years, a nominal loading pressure imposed on the UFC is about 6.6 MPa. This loading does not include the swelling effect of bentonite backfill. A detailed description on how this load was derived is presented in Section 4.5.5.

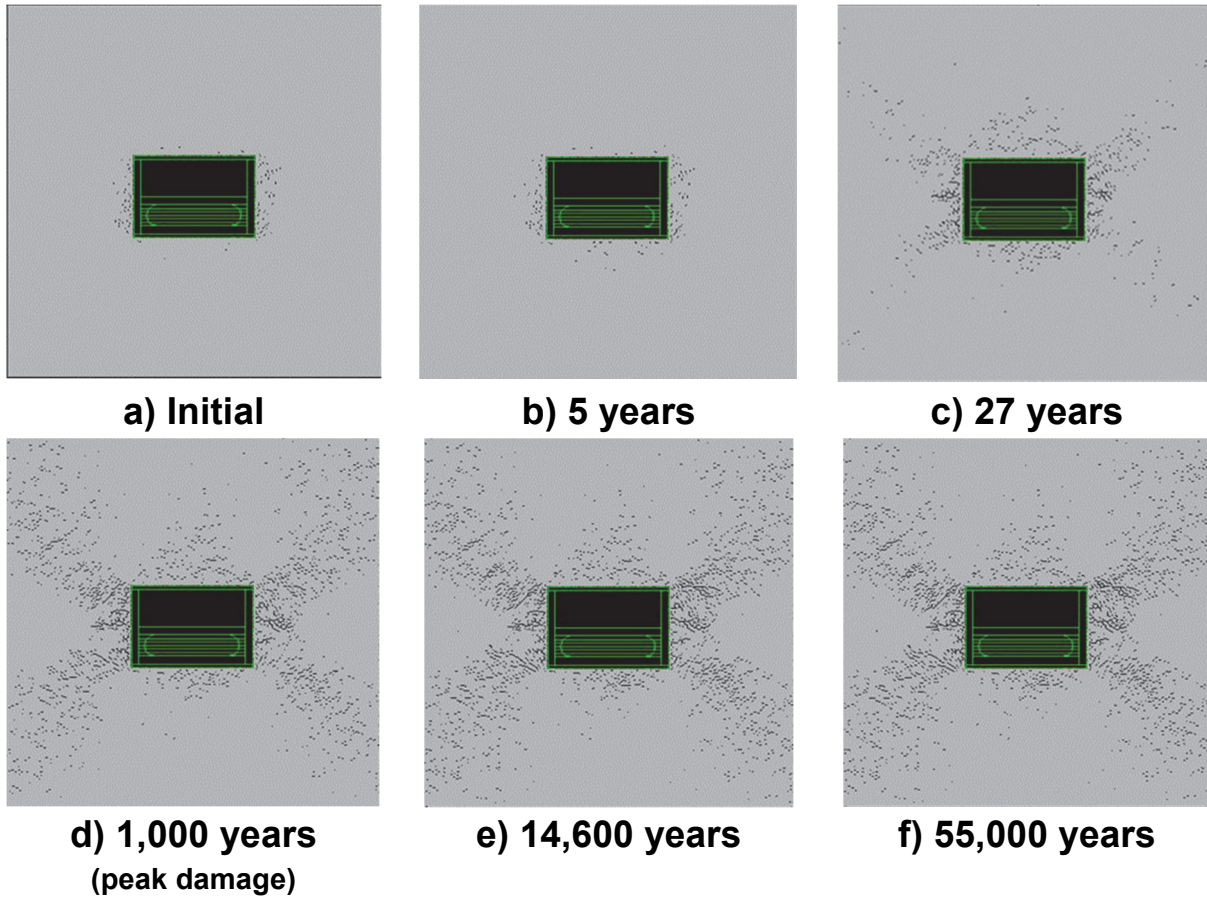


Figure 54: Evolution of Damage in Crystalline Rock

4.5.3 Glacial Loading

The analysis considers in situ and rebound stresses, the effect of time-dependent strength degradation and a single cycle of glaciation. This glaciation occurs during the period between 60,000 years to 174,000 years with a maximum ice thickness of 3.2 km at the site at 150,000 year. Similar to the sedimentary case, glacial loading does not significantly affect the damage around the room before, during and after glaciation, as shown in Figure 55a, Figure 55b and Figure 55c, respectively. Insignificant increase in damage around the rooms during this period can be attributed to the confinement provided by the dense backfill in the placement room. The predicted EDZ extent is similar to that at 50,000 years: about 1 m deep in the room walls. The increase in the vertical glacial loading causes predominantly vertical downward movement, which is uniform across the entire repository (similar to displacements due to heating). The maximum displacements of the room walls during glacial episodes relative to the surrounding rock mass is relatively small, 1.2 cm.

The average pillar stress is 16.8 MPa. Even for the maximum vertical loading during glacial cycle, there is 10-m wide elastic pillar between adjacent placement rooms.

During the glacial episode with maximum ice thickness, the loading on the canister will be at its peak and is estimated to be 16 MPa. A detailed description on how this load was derived is presented in Section 4.5.5.

In essence, the glacial event considered does not induce any additional damage and fracture of rock mass as a result of the confinement provided by backfilling. Thus, analysis with multiple glaciation episodes was not warranted.

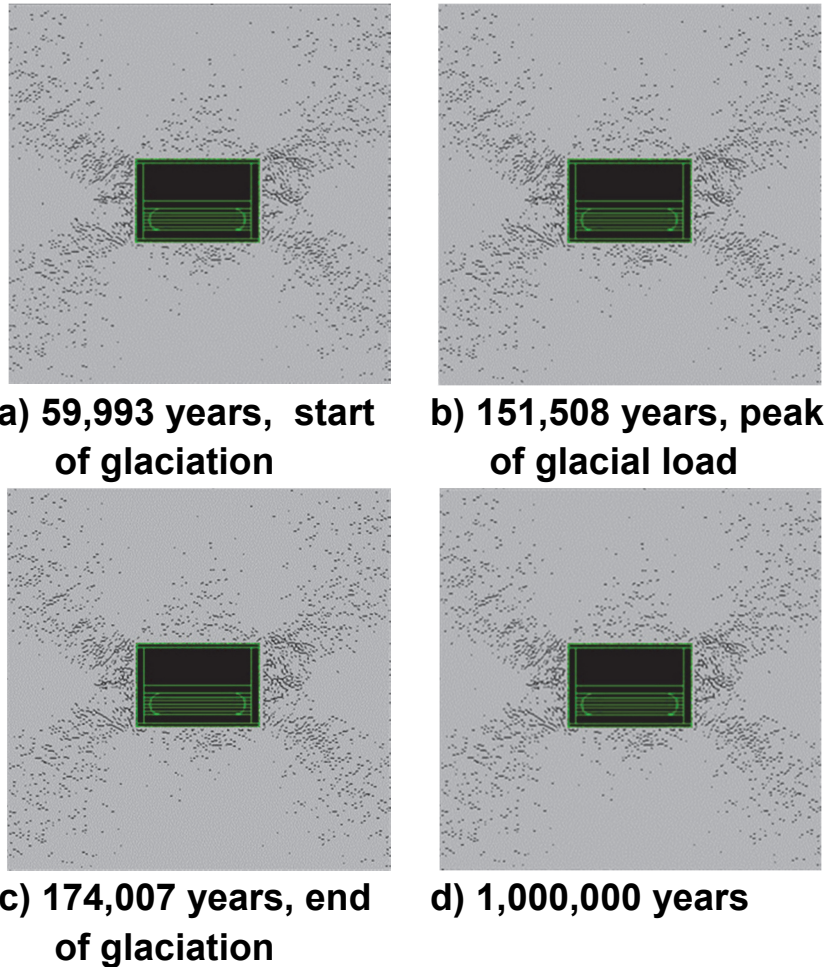


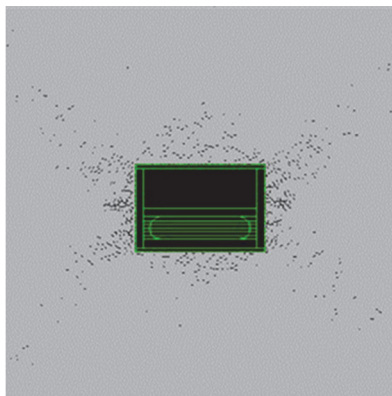
Figure 55: Evolution of Damage during Glaciation Period and Beyond, to 1Ma in Crystalline Rock

Three plots in b through d show the damage predicted by the model if the three ground motions at 10^{-6} p.a. probability level are assumed to occur at the state when the peak temperature is reached. Some additional fracturing develops (compared to the initial state shown in a). However, the general extent and intensity of the damage does not change significantly. Thus, there is no change in EDZ, which remains about 0.5 m wide.

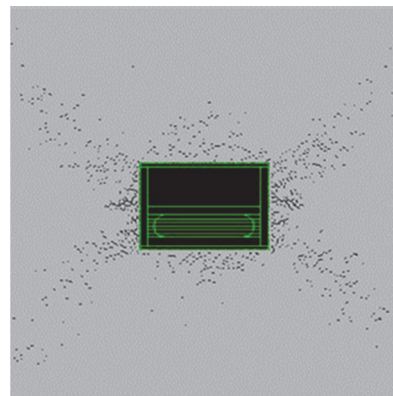
4.5.4 Seismic Loading

Similarly, for the models of seismic loading occurring at the peak glacial loading, the damage due to dynamic shaking is shown in Figure 57. This is the state that initially has more damage than the peak temperature state. Even for this state the considered seismic loading (10^{-6} p.a. probability level) does not cause appreciable increase in damage. Thus, there is no change in EDZ, which was about 1 m wide prior to and after the earthquake events.

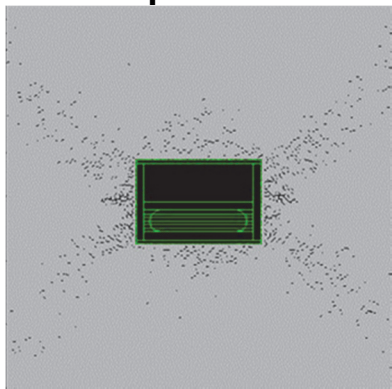
Considering that the ground motions at 10^{-6} p.a. probability level did not result in significant increase in extent or intensity of the damage around the placement room, the effect of seismic ground motions at 10^{-5} p.a. probability level on deformation and damage of the rooms was not simulated. These ground motions would result in even less damage.



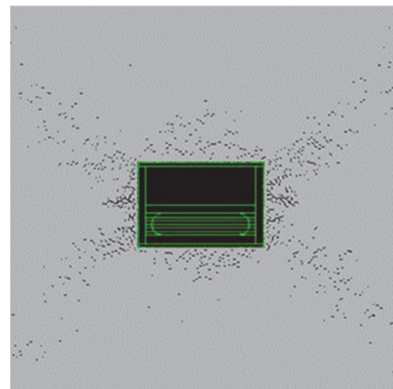
a) Peak temperature, no earthquake



b) M5.25



c) M6.25



d) M7.4

Figure 56: Microcracks in the Rock at Peak Temperature Subjected to Three Different Earthquakes at 10^{-6} Probability Level in Crystalline Rock

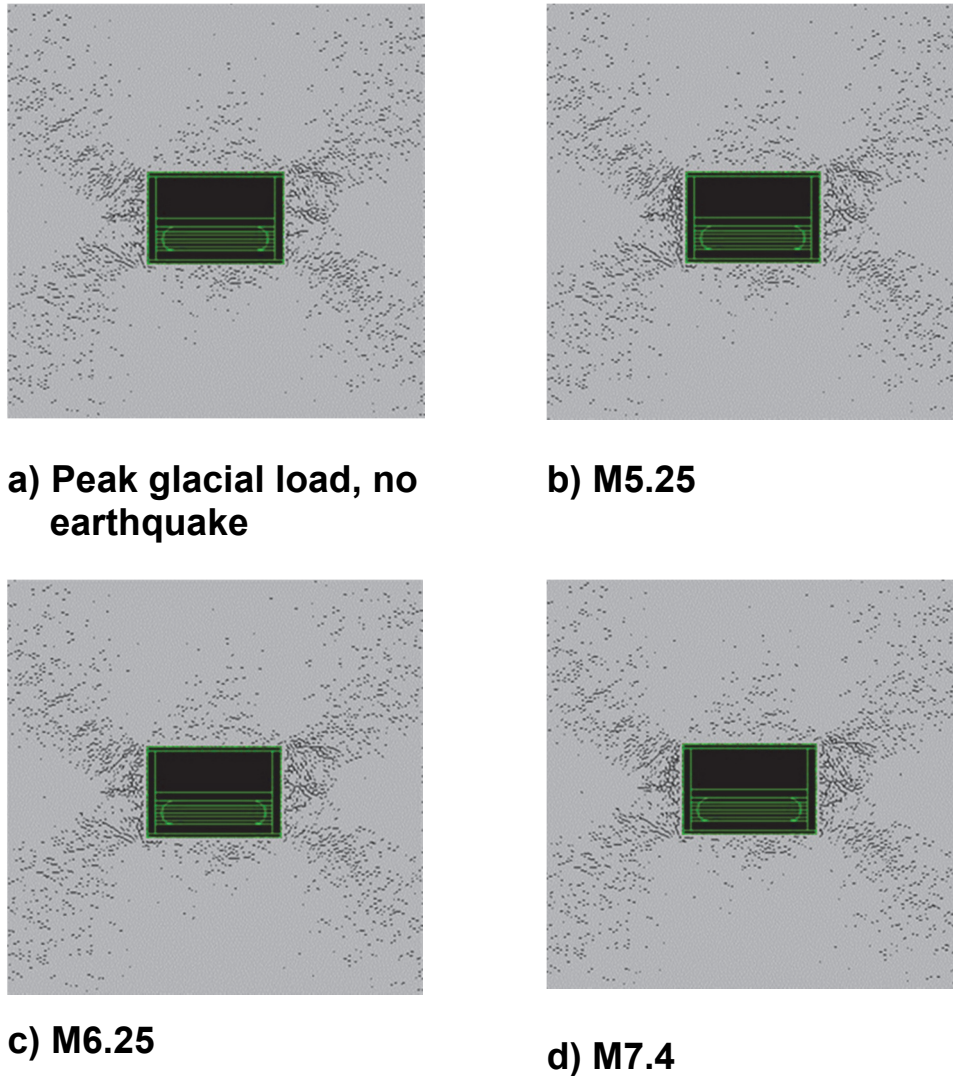


Figure 57: Microcracks in the Rock at Peak Glacial Load Subjected to Three Different Earthquakes at 10^{-6} Probability Level in Crystalline Rock

4.5.5 Loading on the UFC

Similar to the case in sedimentary rock setting (Section 3.5.6), the transient loading on a UFC during external and internal repository perturbations was evaluated at key critical periods throughout the 140ka simulation timeframe. The loads estimated include those due to effective stress and porewater pressure. A time series plot that illustrates the predicted transient loads between 50,000 and 190,000 years, assuming two limiting conditions of pore water dissipation, is shown in Figure 58.

After construction, the placement rooms are stable and no rock stress will be transferred to the UFC after placement other than the weight of the UFC and bentonite backfill. Over time and

before the onset of glacial loading, the load on the UFC will gradual increase due to: 1) placement room resaturation; and, 2) total stress increase due to thermally-induced stress changes. Upon resaturation, the maximum fluid pressure exerted equals to a 500 m deep hydrostatic pressure of 5 MPa in the fresh water case. Whereas the increase in the total stress due to thermally-induced stress are estimated by thermo-mechanical models as described in Section 4.4.1. Within the enclosing rock mass this thermally-induced stress increase combined with hydrostatic porewater pressure reaches a maximum of 6.6 MPa at about 1,000 years, which is less than the lithostatic stress. The UFC loading decreases to values below 6 MPa prior to glaciation and the occurrence of ice-sheet advance and retreat above the repository. It is during this latter period of time that maximum loading of the UFC occurs.

Under undrained conditions, the maximum UFC loading during glaciation is estimated to be approximately 17.6 MPa (“without fluid migration” in Figure 58) due to, in part, “stress arching” created when the lower modulus backfill carries less load than the stiffer enclosing rock mass. If this backfill total stress load is less than the pore water pressure in the rock mass there will be pore water migration toward the emplacement room leading to an increase in the backfill pore water pressure. The exerted UFC pressure is the sum of the initial hydrostatic groundwater pressure (5 MPa), and the change in pore water pressure created by ice-sheet loading and resultant total stress change in the far-field. Using a conservative Skempton coefficient of 0.7 to estimate of the excess pore pressure, a conservative upper bound pressure on UFC could be as high as 22.7 MPa (“fluid migration” in Figure 58). This estimated value is considered cautious as it represents a very conservative assumption that considers only maximum porewater pressure increases without allowing for anticipated fluid migration and pore water pressure dissipation.

After glaciation, the pressures on the UFC reduce to 6.0 MPa and largely remain constant until the next glacial episodes (only one glacial episode is considered in the present study).

The above UFC load estimates do not include the swelling effect of bentonite backfill. Otherwise, assuming a swelling pressure of 7.1 MPa (Baumgartner 2005), the maximum total pressure on the UFC during the peak of glacial loading would become 29.8 MPa.

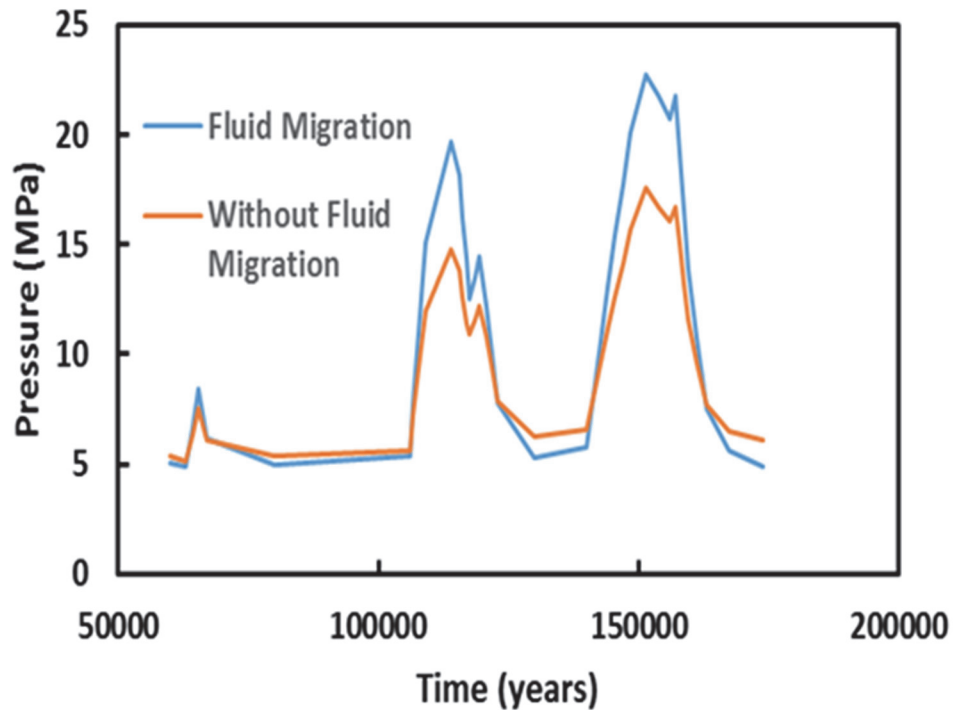


Figure 58: Evolution of Pressure on the UFC in Crystalline Rock

4.5.6 Effect of DFN

The effect of discrete fractures on deformation and stability of the placement rooms was analyzed using the numerical code 3DEC and with explicit representation of the DFN fractures. In order to capture the effect of uncertainty in fracture realization, the analysis was conducted for five different DFN realizations. Two states during evolution of thermally-induced stresses and glacial loading were considered: (1) the state when the peak rock temperature is reached; and (2) the state when the maximum glacial load occurs. These modelling results are considered conservative as the fractures were assumed to be frictional (i.e., zero cohesion) with a relatively small friction angle of 30° and no dilation.

The modelling results indicate that the induced shear displacements on the pre-existing fractures are less than 2 mm for all analyzed cases (both initial states and five DFN realizations). The contour plots of the shear displacements on the joints for the DFN realization II are shown in Figure 59 and Figure 60. The figures show the critical cross-section through the model where the maximum shear displacements occur close to the room boundaries. The magnitude of slip increases for the state at the maximum glacial load. However, even in that case, the maximum slip is less than 2 mm. The maximum shear displacement is not at the room wall but inside the rock mass. Clearly, the DFN does not have significant effect on the deformation of the rock mass around the placement rooms nor on stability of the rooms. The models that use other DFN realizations result in similar predictions, with generally smaller slip magnitudes occurring even further from the room walls compared to the results for the DFN realization 2 shown in Figure 59 and Figure 60.

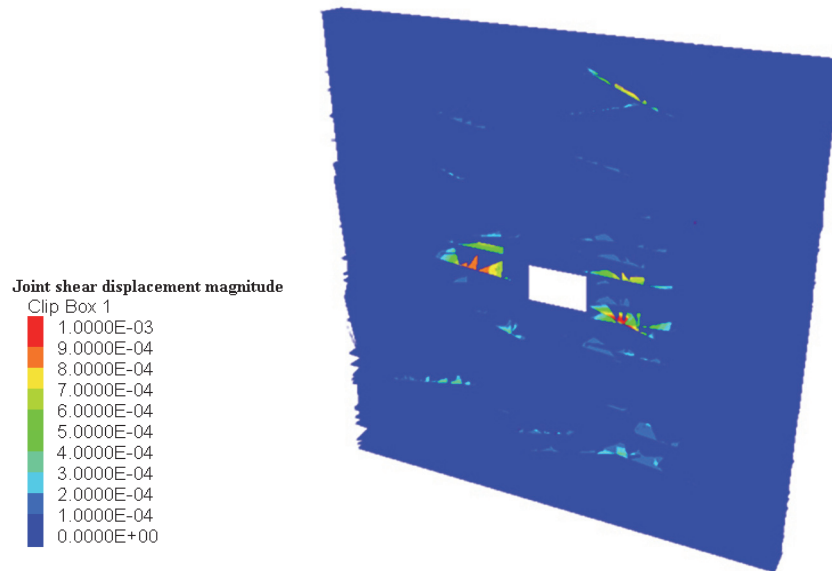


Figure 59: DFN realization II: Contours of Shear Displacements (m) on Joints at Peak Rock Temperature

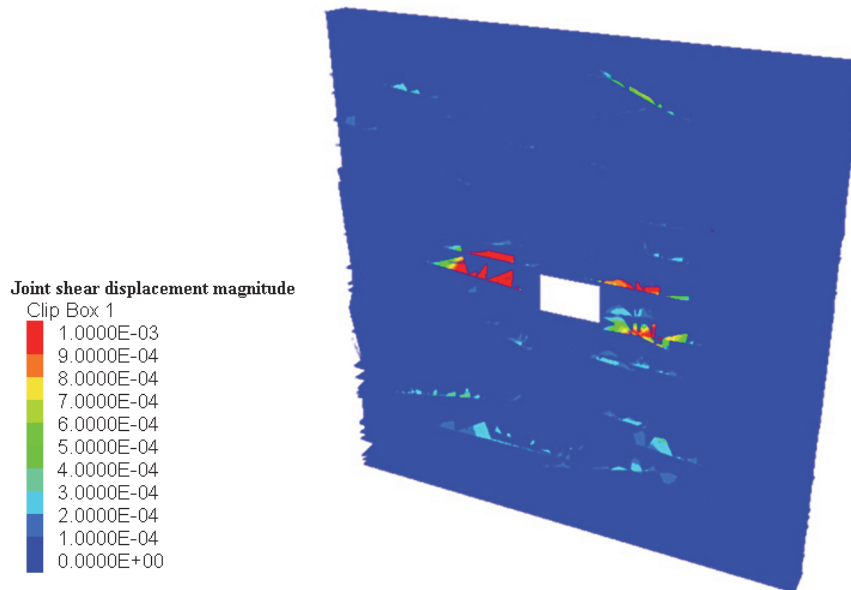


Figure 60: DFN Realization II: Contours of Shear Displacements (m) on Joints at Peak Glacial Load

4.6 SUMMARY AND DISCUSSION

The analyses considered a series of bounding simulations designed to gain insight into the response and degree of damage in the near- and far-field associated with the expected evolution of a repository to 1Ma. The simulations also provided a reasoned basis to estimate Used Fuel Canister (UFC) loading. Each of the simulations considered a base-case scenario that included in-situ stresses, time-dependent strength degradation of rock mass, pore pressure in rock mass, UFC thermal output, and multiple glacial ice sheet advances and retreats (max. thickness ca. 3 km). Repository perturbations superimposed on the base cases were:

1. A low probability (rare) earthquake of 10^{-6} p.a. (0.5g);
2. Internal repository gas generation (8.3 MPa); and
3. Extreme combinations of the loads and perturbations above.

The simulations illustrate that at the end of construction, induced damage is contained within meters of the placement rooms and a HDZ as defined in Fracture Systems (2011) is not expected to form.

EDZ (Fracture Systems 2011) develops around the placement rooms after excavation. The damage peak near the end of the thermal loading cycle at approximately 1,000 years and is predicted to be approximately 1 m deep in the walls. However, the models also predict EdZ (excavation disturbed zone) extending up to 3 m from the rooms forming a characteristic butterfly shape. The EdZ is characterized by sparse cracking, which does not result in localization in the form of macro fractures or shear zones. Within the EdZ the rock mass is in the pre-peak stress state, between the crack initiation (~40% UCS) and crack damage (~85% UCS) stress states.

The thermally-induced stresses are the main loading condition affecting the extent and intensity of rock mass damage. The analyses demonstrated that other loading conditions, including glacial loading, seismic loading and time-dependent strength degradation, have relatively small effect on damage and stability of the rooms. The confinement provided by the engineered backfill is the main reason for such observations.

Relatively large coefficient of linear thermal expansion (10^{-5} $1/^\circ\text{C}$) in stiff rock results in large thermally-induced stress changes. Also, conservative assumptions of effective stress calculation with pore pressure corresponding to hydrostatic distribution with the water table at the ground surface, resulted in weakening of the rock mass and greater extent of the damage. Better estimation of the coefficient of linear thermal expansion and more refined consideration of the magnitude of the pore pressure and its effect on the strength of low-porosity rocks would certainly result in prediction of lesser extent and intensity of the damage. Even for assumed conservative conditions, the models predict 10-m wide elastic pillars between adjacent placement rooms in all scenarios simulated.

Heating causes relatively large displacements of the rock mass. Expansion of the rock mass results in predominantly vertical movement upwards. The maximum displacements on the repository level are of the order of 3.8 cm. However, this movement is relatively uniform across the entire repository, with relatively small differential displacements that could not affect the performance of the rooms. Similarly, the increase in the vertical glacial loading causes predominantly vertical downward movement, which is uniform across the entire repository. The predicted maximum relative displacement of the rock mass around the placement rooms is less than 1.2 cm (at the state of the maximum glacial load).

The maximum placement room convergence is predicted to be less than 5 mm throughout the entire 1 Ma period.

Explicit representation of the DFN does not result in an unfavourable response of the rock mass compared to the predictions of the continuum and Voronoi block models. Some slip on subhorizontal structures in the vicinity of the rooms is observed. However both magnitude of slip (less than 2 mm) and extent are not such to affect performance of the repository.

5. CONCLUSIONS

The purpose of this study is to illustrate the geomechanical responses of Mark II conceptual designs to perturbations occurring in the time frame of 1 Ma. The analyses considered a broad range of scenarios, described below, that are intended to provide a bounding estimate of rock mass damage evolution in the repository near- and far-field. This included the prediction of the excavation damage zone and a zone of micro-cracking induced by the redistribution of ground stresses around placement rooms. The simulations performed considered construction and backfilling sequences, representative rock mass properties and in situ ground stresses, repository thermal history, thermally induced stresses, time-dependent strength degradation, repository gas generation, groundwater pore pressures, glacial ice sheet loading (repeated), strong seismic ground motions and effects of combinations of loads and perturbations.

In order to conduct the analyses a number of assumptions were applied to provide a reasoned assessment of repository stability and resilience to future loading. These included:

- 1) **Hydraulic Formation Pressures:** A hydrostatic formation (fresh) pore water pressure of 5 MPa was assumed for the repository at 500 m depth;
- 2) **Long-term Rock Mass Strength:** Time dependent rock mass strength degradation was simulated with the long-term rock mass strength set at the mean crack initiation stress of intact rock. This lower bound strength is assumed to be approximate 40% of Unconfined Compressive Strength in both Cobourg limestone and granite host rocks. To account for the pre-existing joint system within the granitic host rock, the intact rock strength was further degraded with a Geological Strength Index of 79;
- 3) **Temperature Evolution:** The emplacement room geometry and layout is designed to maintain a maximum used fuel canister surface temperature less than 100°C;
- 4) **Glaciation:** Site specific transient glacial ice-sheet histories and loading were explicitly considered with maximum ice-sheet thicknesses approaching 3 km;
- 5) **Earthquakes:** Rare, strong and broad spectrum ground motions (i.e., 10^{-6} p.a.; 0.5g) associated with long return period (1 Ma) earthquake events were simulated at times of repository vulnerability;
- 6) **Repository Gas Pressures:** Gas generation rates within the repository in sedimentary rock setting as a result of corrosion processes is estimated to yield a maximum pressure of 8.3 MPa at 29,000 years;
- 7) **Effective Stress Formulation:** Effective stress calculations were estimated without considering pore pressure relief in low porosity rocks (i.e. <0.01). A conservative Skempton's of 0.7 was assumed in the pore pressure estimation;
- 8) **Bedding and Joint Strength:** Artificial bedding planes of 0.75 m spacing were constructed explicitly in modelling of Cobourg limestone. To be consistent with very high RQD and absence of planes of weakness observed during regional borehole investigation, these bedding planes were assumed not to be continuous but with 50% of the rock bridges within the planes with the strength equal to that of the intact rock. Whereas, for the granitic rock mass, a discrete fracture network based on mapping data from Forsmark, Sweden was used in three-dimensional numerical models. All discontinuities were assumed to be cohesionless with a relatively low friction angle of 30°;

- 9) **Thermal Expansion:** Relatively high coefficients of thermal expansion were applied to yield bounding estimates of rock mass damage; and
- 10) **Blasting-Induced Damage:** It is assumed that excavation of the rooms will be conducted in such a way that blast-induced damage will be minimal.

Voronoi block models were used to simulate time-dependent mechanical behaviour of the rocks and potential degradation of rock (including micro cracking) around the placement rooms. The conclusions drawn from the analyses are summarized below.

- 1) Thermal analyses revealed that the Mark II conceptual design yield UFC surface temperatures below 100°C satisfying DGR design requirements;
- 2) Assuming that excavation-induced damage will be minimum, rock mass damage in close proximity to the excavated repository openings occurs as a result of in-situ stress magnitude and orientation, thermally-induced stress changes and time-dependent rock mass strength degradation. The damage evolves with time but is primarily driven by thermally-induced stress changes. Maximum thermally-induced stress changes and rock mass damage occur before 2,000 years;
- 3) Rock mass failure occurs as shear with insignificant dilation. The maximum extent of the Excavation Damage Zone (EDZ) in the two rock types are:
 - i. Cobourg limestone: approximately 1 m into the room ceiling and floor. Slippage along assumed bedding planes may extend to 2 m from the room walls.
 - ii. Granite: approximately 1 m into the walls of placement rooms.
- 4) A Highly Damaged Zone (HDZ) is not predicted to occur along excavated placement room surfaces because of the backfill inside the rooms prevents its formation. Spalling or tensile failure are not evident for any considered loading condition;
- 5) Simulations performed considered an effective stress formulation that would promote rock mass strength weakening and greater damage. More refined consideration of the magnitude of the pore pressure and its effect on the strength of low-porosity rocks in fully coupled analysis would result in less damage extent and intensity. Even for such bounding conditions, a 10-m wide elastic (load bearing) pillar exists between placement rooms under all loading conditions considered;
- 6) Cyclic glacial repository loading generated minor rock mass damage;
- 7) The effect of rare and extreme seismic ground motions is small with results revealing virtually no increase in rock mass damage;
- 8) Bounding simulations that consider extreme combinations of loading (e.g., rare seismic ground motions at maximum far-field temperature and glacial ice-sheet loading) indicate virtually no increase in rock mass damage;
- 9) For the sedimentary rock case, despite internally-generated repository gas pressures (8.3 MPa) approaching lithostatic (approximate 13 MPa), the effect on the placement room wall damage is minor. Estimated gas generation rates and pressures do not generate tension in the placement room wall or lead to the initiation or propagation of gas-driven fracture(s);
- 10) The long-term strength of both Cobourg limestone and granite does not have significant effect on room stability. The bounding long-term strength (i.e., 40% of the

rock mass unconfined compressive strength) results in relatively small damage. It is evident that the engineered backfill provides the necessary confinement to prevent spalling and/or fracture dilation, and likely contributes to slowing the rate of time-dependent strength degradation;

- 11) The thermally-induced rock mass stresses are the main loading condition affecting the extent and intensity of rock mass damage;
- 12) Heating creates vertical displacement of the rock mass. The maximum displacements at the repository level are on the order of 30 mm and 38 mm due to thermally-induced stress changes in sedimentary and crystalline rock setting, respectively. The displacements are relatively uniform such that only small (i.e., order of millimeter) differential displacements occur. Maximum predicted placement room convergence is less than 5 mm in both cases;
- 13) The maximum mechanical and hydrostatic loads on the Mark II UFCs considering with and without bentonite swelling are:

Host Rock	UFC Surface Load without Bentonite Swelling (MPa)	UFC Surface Load with Bentonite Swelling (MPa)
Cobourg Limestone	20.8	22.7
Granite	22.7	29.8

and

- 14) For the crystalline rock case, explicitly represented discrete fracture network as considered in 3 dimensional modelling does not result in significant additional deformation. The predicted maximum shear deformation of less than 2 mm will not have any effect on stability and performance of the placement rooms.

In summary, natural and repository-induced perturbations that could influence the evolution and performance of a deep geologic repository were explored through a series of bounding numerical simulations. The results indicate that the repository placement rooms at 500 m depth will remain stable. The integrity of the natural barrier provided by the enclosing rock mass is not influenced. The assessment provides evidence of relative small rock mass displacements and evolution of an EDZ principally at early times less than 1 m from the excavated surfaces for the Mark II conceptual repository designs.

REFERENCES

- Adams, J., and J. S. Bell. 1991. Crustal stresses in Canada. In: Neotectonics of North America. Slemmons, D.B., E. R. Engdahl, M. D. Zoback and D. D. Blackwell (eds.). Geological Society of America, Decade Map Volume 1, 367-386.
- AMEC GEOMATRIX. 2011. Seismic Hazard Assessment. AMEC Geomatrix, Inc. report for the Nuclear Waste Management Organization NWMO DGR-TR-2011-20 R000. Toronto, Canada.
- Arjang, B. 2001. Database on Canadian in situ ground stresses, Technical Note, Canada Centre for Mineral and Energy Technology – Mining and Mineral Sciences Laboratories March 2001.
- Barton, N. 2007. Rock Quality, Seismic Velocity, Attenuation and Anisotropy. Taylor and Francis. London, United Kingdom.
- Bauer, S.J., D.E. Munson, M.P. Hardy, J. Barrix and B. McGunegle. 2005. In situ measurements and their implications in a deep Ohio mine. In: Chen, G. et al. (eds.). Alaska Rocks 2005 — Rock Mechanics for Energy, Mineral and Infrastructure Development in the Northern Regions. Paper ARMA/USRMS 05-804. ARMA, University of Alaska-Fairbanks.
- Baumgartner, P. 2005. Scoping Analyses for the Design of a Deep Geologic Repository in Sedimentary Rock. Atomic Energy of Canada Limited. Report number: 06819-REP-01300-10093-R00.
- BSC. 2004a. Drift degradation analysis. Yucca Mountain Project Report ANL-EBS-MD-000027 REV 03. Las Vegas, USA.
- Cartwright, P.B. 1997. A review of recent in situ stress measurements in United Kingdom coal measures strata. In Sugawara K, Y. Obara (eds.). Proceedings International Symposium on Rock Stress, Kumamoto. A. A. Balkema, Rotterdam.
- Damjanac, B., M. Board, M. Lin, D. Kicker and J. Leem. 2007. Mechanical Degradation of Emplacement Drifts at Yucca Mountain – A Modelling Case Study. Part II: Lithophysal Rock. International Journal of Rock Mechanics and Mineral Science 44, 368-399.
- Damjanac, B., and C. Fairhurst. 2010. Evidence for a long-term strength threshold in crystalline rock. Rock Mechanics and Rock Engineering 43(5), 1–19.
- Detournay, E. and A.H.-D. Cheng. 1993. Fundamentals of poroelasticity. In: Hudson, J., E.T. Brown, C. Fairhurst and E. Hoek (Eds.). Comprehensive Rock Engineering 2.
- Fox, A., P. La Pointe, J. Hermanson and J. Öhman, 2007. Statistical geological discrete fracture network model, Forsmark modelling stage 2.2., R-07-46, Svensk Kärnbränslehantering AB.
- Fracture Systems. 2011. Excavation Damaged Zones Assessment. Fracture Systems Ltd. report for the Nuclear Waste Management Organization NWMO DGR-TR-2011-21 R000. Toronto, Canada.
- Garisto, F., A. D'Andrea, P. Gierszewski and T. Melnyk. 2004. Third Case Study – Reference Data and Codes. Ontario Power Generation Report Number 06819-REP-01200-10107-R00, Toronto, Ontario.

- Geofirma and Quintessa. 2011. Postclosure Safety Assessment: Gas Modelling. Geofirma Engineering Ltd. and Quintessa Ltd. report for the Nuclear Waste Management Organization NWMO DGR-TR-2011-31 R000. Toronto, Canada.
- Golder Associates. 2012. Thermo-Mechanical Analysis of a Single Level Repository for Used Nuclear Fuel, APM-REP-00440-0010, Golder Associates Report No. 11-1117-0045-00.
- Golder Associates. 2013. OPG's Deep Geological Repository for Low and Intermediate Level Waste, Factual Report – Boreholes DGR-7 and DGR-8, Geotechnical Logging. DGR-REP-01130-28028.
- Gorski, B., T. Anderson and B. Conlon. 2009a. Laboratory Geomechanical Strength Testing of DGR-1 & DGR-2 Core. Intera Engineering Ltd. Report TR-07-03 Rev.3. CANMET Mining and Mineral Sciences Laboratories. Ottawa, Canada.
- Gorski, B., T. Anderson and B. Conlon. 2009b. DGR-2 Long-term strength degradation tests TR-08-11, Revision 0. Canada Centre for Mineral and Energy Technology – Mining and Mineral Sciences Laboratories. Ottawa.
- Gorski, B., T. Anderson and B. Conlon. 2010a. Laboratory Geomechanical Strength Testing of DGR-3 & DGR-4 Core. Intera Engineering Ltd. Report TR-08-24 Rev.1. CANMET Mining and Mineral Sciences Laboratories. Ottawa, Canada.
- Gorski, B., T. Anderson and B. Conlon. 2010b. Long-term strength testing of DGR-3 and DGR-4 Core TR-08-36, Revision 1. Canada Centre for Mineral and Energy Technology – Mining and Mineral Sciences Laboratories. Ottawa.
- Guo, R. 2007. Numerical modelling of a deep geological repository using the in-floor borehole placement method. Nuclear Waste Management Organization NWMO TR-2007-14. H
- Hoek, E. and M.S. Diederichs. 2006. Empirical estimation of rock mass modulus. International Journal of Rock Mechanics and Mining Sciences, 43, 203–215.
- Intera. 2011. Descriptive Geosphere Site Model. Intera Engineering Ltd. report for the Nuclear Waste Management Organization NWMO DGR-TR-2011-24 R000. Toronto, Canada
- Itasca. 1999. PFC2D (Particle Flow Code in 2 Dimensions) Version 2.0. Itasca Consulting Group Inc. Minneapolis, USA. Itasca. 2012. FLAC3D (Fast Lagrangian Analysis of Continua in 3 Dimensions) Version 5.2. Itasca Consulting Group Inc. Minneapolis, USA.
- Itasca. 2011. Long-Term Geomechanical Stability Analysis. Itasca report to the Nuclear Waste Management Organization NWMO DGR-TR-2011-17, Toronto, Canada.
- Itasca. 2012. FLAC3D (Fast Lagrangian Analysis of Continua in 3 Dimensions) Version 5.2. Itasca Consulting Group Inc. Minneapolis, USA.
- Itasca. 2013. 3DEC (3-Dimensional Distinct Element Code) Version 5.2. Itasca Consulting Group Inc. Minneapolis, USA.
- Itasca. 2014. Universal Distinct Element Code (UDEC) Version 6.00. Itasca Consulting Group Inc. Minneapolis, USA.
- Jaeger, J.C. and N.G.W. Cook. 1979. Fundamentals of Rock Mechanics. 3rd Edition. Chapman and Hall, New York, USA.
- Kaiser, P. K., and S. Maloney. 2005. Review of Ground Stress Database for the Canadian Shield Report No. 06819-REP-01300-10107-R00. December 2005.

- Lau, J.S.O., B. Gorski, B. Conlon and T. Anderson. 2000. Long-term Loading Tests on Saturated Granite and Granodiorite. Ontario Power Generation Report 06819-REP-01300-10016 R00. Toronto, Canada.
- Lo, K.Y. and R.S.C. Wai. 1982. Thermal expansion, diffusivity, and cracking of rock cores from Darlington, Ontario. Canadian Geotechnical Journal. Vol. 19, p154-166.
- National Building Code of Canada (NBCC). 2010.
- Nicksiar, M. and C.D. Martin. 2013. "Crack Initiation Stress in Low Porosity Crystalline and Sedimentary Rocks." Engineering Geology 154: 64–76.
- NWMO. 2012. Used Fuel Repository Conceptual Design and Post-closure Safety Assessment in Crystalline Rock. NWMO TR-2012-16, Toronto, Ontario
- NWMO. 2014. 2014 APM Conceptual Design and Cost Estimate Update. Underground Repository Design Criteria. Technical Memorandum. Doc No: APM-DCRI-22100-0001 revision R00e.
- NWMO. 2015. Technical Program for Long-Term Management of Canada's Used Nuclear Fuel – Annual Report 2014. NWMO TR-2015-01, Toronto, Ontario.
- Peltier, W.R. 2011. Long-Term Climate Change. Nuclear Waste Management Organization Report NWMO DGR-TR-2011-14 R000. Toronto, Canada.
- Schmidtke, R.H. and E.Z. Lajtai. 1985. The long-term strength of Lac du Bonnet Granite. International Journal of Rock Mechanics and Mining Science 22, 461-465.
- SKB. 2009. Underground Design Forsmark Layout D2, Swedish Nuclear Fuel and Waste Management Company Report No R-08-116, July 2009
- SNC-Lavalin. 2014. 2014 APM Conceptual Design and Cost Estimate Update, Conceptual Design for Mark II Underground Repository in Crystalline Rock and Sedimentary Rock, SNC-Lavalin Nuclear Inc., APM-TDM-22100-0003, October 2014.
- Valley, B., and S. Maloney. 2010. Analyses of DGR-1 and DGR-2 Borehole Images for Stress Characterization TR-08-35. MIRARCO.
- Wu, P. 2013. Estimation of maximum horizontal rebound stresses at 850 m depth below Bruce nuclear site. NWMO Technical Memorandum.

APPENDIX A: ABBREVIATIONS, ACRONYMS AND UNITS

APM	Adaptive Phased Management
CI	Crack Initiation
CD	Crack Damage
D	Damage Coefficient
DFN	Discrete Fracture Network
DISL	Damage Initiation and Spalling Limit
DGR	Deep Geologic Repository
E	Elastic Modulus
EDZ	Excavation Damage Zone
EdZ	Excavation Disturbed Zone
GGM	Gas-Generation Model
GSI	Geological Strength Index
GPa	Giga Pascal
HDZ	Highly Damaged Zone
kPa	kilo Pascal
LdB	Lac du Bonnet
L&ILW	Low and Intermediate Level Waste
mBGS	metres Below Ground Surface
M	Earthquake Magnitude
MS	Mechanostratigraphic Unit
MPa	megapascal
Ma	million years
NWMO	Nuclear Waste Management Organization
OPG	Ontario Power Generation Inc.
P_c	Confining Pressure
PGAs	Peak Ground Accelerations
PGVs	Peak Ground Velocities
ν	Poisson's Ratio
σ_1	Applied Stress in Axial Direction of Samples
σ_H	Maximum Horizontal In Situ Stress
σ_h	Minimum Horizontal In Situ Stress
σ_n	Confining Stress
σ_v	Vertical In Situ Stress
(σ / σ_c)	Driving-stress-ratio
T_f	Time-to-failure
TBM	Tunnel Boring Machine
3D	three-dimensional
UCS	Unconfined Compressive Strength
UCS ₀	Initial UCS
UCS ₁₀₀	UCS at 100 days
UFC	Used Fuel Container
UofT GSM	University of Toronto Glacial Systems Model